

# The Shubnikov de Haas effect in narrow-gap semimagnetic semiconductors

**Citation for published version (APA):**

Schleijpen, H. M. A. (1987). *The Shubnikov de Haas effect in narrow-gap semimagnetic semiconductors*. [Phd Thesis 1 (Research TU/e / Graduation TU/e), Applied Physics and Science Education]. Technische Universiteit Eindhoven. <https://doi.org/10.6100/IR272283>

**DOI:**

[10.6100/IR272283](https://doi.org/10.6100/IR272283)

**Document status and date:**

Published: 01/01/1987

**Document Version:**

Publisher's PDF, also known as Version of Record (includes final page, issue and volume numbers)

**Please check the document version of this publication:**

- A submitted manuscript is the version of the article upon submission and before peer-review. There can be important differences between the submitted version and the official published version of record. People interested in the research are advised to contact the author for the final version of the publication, or visit the DOI to the publisher's website.
- The final author version and the galley proof are versions of the publication after peer review.
- The final published version features the final layout of the paper including the volume, issue and page numbers.

[Link to publication](#)

**General rights**

Copyright and moral rights for the publications made accessible in the public portal are retained by the authors and/or other copyright owners and it is a condition of accessing publications that users recognise and abide by the legal requirements associated with these rights.

- Users may download and print one copy of any publication from the public portal for the purpose of private study or research.
- You may not further distribute the material or use it for any profit-making activity or commercial gain
- You may freely distribute the URL identifying the publication in the public portal.

If the publication is distributed under the terms of Article 25fa of the Dutch Copyright Act, indicated by the "Taverne" license above, please follow below link for the End User Agreement:

[www.tue.nl/taverne](http://www.tue.nl/taverne)

**Take down policy**

If you believe that this document breaches copyright please contact us at:

[openaccess@tue.nl](mailto:openaccess@tue.nl)

providing details and we will investigate your claim.

**THE SHUBNIKOV DE HAAS EFFECT  
IN NARROW-GAP  
SEMIMAGNETIC SEMICONDUCTORS**

**H. M. A. SCHLEIJPEN**

**THE SHUBNIKOV DE HAAS EFFECT  
IN NARROW-GAP  
SEMIMAGNETIC SEMICONDUCTORS**

**PROEFSCHRIFT**

**TER VERKRIJGING VAN DE GRAAD VAN DOCTOR AAN  
DE TECHNISCHE UNIVERSITEIT EINDHOVEN, OP GEZAG  
VAN DE RECTOR MAGNIFICUS, PROF. DR. F.N. HOOGE  
VOOR EEN COMMISSIE AANGEWEZEN DOOR HET COLLEGE  
VAN DEKANEN IN HET OPENBAAR TE VERDEDIGEN OP  
DINSDAG 27 OKTOBER 1987 TE 14.00 UUR**

**DOOR**

**HENRICUS MARIA ANTONIUS SCHLEIJPEN**

**GEBOREN TE HEERLEN**

Dit proefschrift is goedgekeurd door de promotoren:

Prof. dr. J.H. Wolter

en

Prof. dr. ir. W.J.M. de Jonge

Co-promotor: Dr. ir. F.A.P. Blom

*aan mijn ouders*

## TABLE OF CONTENTS

I	INTRODUCTION	1
	1.1 History of SMSC	3
	1.2 Bandstructure and exchange interaction	4
	1.3 Trends in research and applications of SMSC	8
	References	15
II	THE SHUBNIKOV DE HAAS EFFECT	20
	2.1 The free electron model for the Shubnikov de Haas oscillations	21
	2.2 Quantitative expression for the Shubnikov de Haas oscillations	22
	2.3 Spin effects on the Shubnikov de Haas amplitude	25
	2.4 Splitting of the electron spin levels	28
	References	29
III	BANDMODELS FOR SEMIMAGNETIC SEMICONDUCTORS	30
	3.1.1 Bandstructure of a narrow-gap semiconductor	30
	3.1.2 Bandstructure of a semiconductor with zinc blende symmetry	32
	3.1.3 Extension of the bandstructure model to SMSC	36
	3.1.4 Bandstructure in a quantising magnetic field	38
	3.1.5 Modified Pidgeon Brown model	46
	3.2 Bandstructure of a semiconductor with tetragonal symmetry	50
	References	51
IV	NUMERICAL CALCULATION OF THE ELECTRON ENERGY LEVELS IN $\text{Hg}_{1-x}\text{Mn}_x\text{Se}$	53
	4.1 Numerical algorithm	53
	4.2 Inversion asymmetry effects on the bandstructure	56
	References	58

<b>V</b>	<b>SAMPLE PREPRATION</b>	<b>60</b>
	5.1 Crystal growth	60
	5.2 Crystal orientation	62
	5.3 Composition analysis	62
	5.4 Annealing	65
	5.5 Current and voltage leads	68
	References	69
<b>VI</b>	<b>EXPERIMENTAL TECHNIQUE</b>	<b>70</b>
	6.1 Shubnikov de Haas measurements	70
	6.2 Cryostats and magnets	74
	6.3 Methods of data analysis	77
	6.4 Magnetisation measurements	79
	References	81
<b>VII</b>	<b>EXPERIMENTAL RESULTS ON <math>\text{Hg}_{1-x}\text{Mn}_x\text{Se}</math> AND THEIR INTEEPRETATION</b>	<b>82</b>
	7.1 Bandparameters	82
	7.2 Magnetisation	84
	7.3 Shubnikov de Haas results and discussion	88
	7.3.1 Shubnikov de Haas oscillation period	88
	7.3.2 Nodes in the Shubnikov de Haas oscillation amplitude	92
	7.3.3 Exchange interaction	97
	7.3.4 Inversion asymmetry	102
	7.3.5 Zero-field splitting	110
	References	114
<b>VIII</b>	<b>EXPERIMENTAL RESULTS ON <math>(\text{Cd}_{1-x}\text{Mn}_x)_3\text{As}_2</math> AND THEIR INTERPRETATION</b>	<b>116</b>
	8.1 Bandparameters	116
	8.2 Magnetisation	118
	8.3 Shubnikov de Haas results and interpretation	120
	8.3.1 Anisotropy of the oscillation period	121
	8.3.2 Nodes in the oscillation period	123
	References	127

<b>IX</b>	<b>DISTORTED SHUBNIKOV DE HAAS SIGNALS</b>	128
9.1	Nodes in the Shubnikov de Haas oscillations due to beating effects	128
9.2	Second oscillation period	130
9.3	Appearance of the superconducting phase transition of solders in magnetoresistance measurements	135
	References	141
	<b>SUMMARY</b>	142
	<b>SAMENVATTING</b>	144



## CHAPTER I INTRODUCTION.

Semimagnetic Semiconductors (SMSC) or Diluted Magnetic Semiconductors (DMS) are semiconducting compounds in which magnetic ions are incorporated at substitutional positions of a host lattice. The substitution of magnetic ions introduces localised spins in the lattice. These localised spins drastically change both the semiconducting and the magnetic properties of the material compared to those of the non-magnetic host material. Due to this change of properties, SMSC have gained an increasing interest in the last decade. Two recent review papers on this subject have been written by Brandt and Moshchalkov [1] and by Lyapilin and Tsidilkovskii [2].

The semiconducting properties of SMSC are strongly influenced by the spin exchange interaction between the localised spins of the magnetic ions and the spins of the mobile band electrons. Compared to non-magnetic semiconductors, the exchange interaction drastically enhances all effects related to the spins of the band electrons. The orbital properties of the band electrons remain unchanged. At liquid helium temperatures this results in large splittings of the electron spin energies even at moderate magnetic fields of about 1 T. For example in wide-gap SMSC, gigantic Zeeman splittings up to 20 meV are observed [3], which lead to an enormous Faraday rotation [4]. In narrow-gap SMSC the spin splitting of a particular Landau level can even exceed the splitting between adjacent Landau levels. This gives rise to an anomalous behaviour of the amplitude of quantum oscillation effects [5].

The magnetic properties of SMSC arise from the localised magnetic atoms. The spins of these magnetic atoms interact with each other. However, this interaction is less strong than in magnetic semiconductors and therefore the spins still respond to an externally applied magnetic field. The magnetic properties are studied by measuring for example: the specific heat, the low field magnetic susceptibility and the magnetisation. In general at high temperatures ( $T > 50$  K) the magnetic susceptibility is well described by the Curie-Weiss law, with an antiferromagnetic spin-spin interaction. For lower temperatures ( $T < 30$  K) the susceptibility deviates from the Curie-Weiss law,

showing a paramagnetic behaviour. At much lower temperatures a phase transition to the spin-glass phase may occur. At the transition temperature a characteristic cusp in the susceptibility is observed, whereas no anomaly in the specific heat occurs.

The magnetic properties of SMSC and the mechanism responsible for the interaction between the localised spins are treated in [6,7] and will not be discussed in detail in this thesis. However, since the electronic properties are very sensitive to the state of the magnetic subsystem via the exchange interaction between localised spins and band electron spins, a good description of the magnetisation is necessary for the interpretation of experiments on the semiconducting properties of SMSC.

The organisation of this thesis is as follows:

Chapter 2 deals with the Shubnikov de Haas (SdH) effect. After a general introduction the effects of spin level splitting and the origin of nodes in the oscillation amplitude is discussed.

In chapter 3 we present the new bandstructure model, which we developed for the interpretation of our  $\text{Hg}_{1-x}\text{Mn}_x\text{Se}$  data. This new model is compared to the modified Pidgeon Brown model [5], which is used for the interpretation of data by other authors reporting on results on this material. Also the bandstructure model for  $(\text{Cd}_{1-x}\text{Mn}_x)_3\text{As}_2$  with tetragonally distorted crystal structure is given in this chapter.

In chapter 4 we discuss how the electron energy levels can be calculated numerically with the help of our new bandmodel. Also some examples of the effects of inversion asymmetry on the bandstructure are given.

The sample preparation is described in Chapter 5. Some attention is paid to our attempts to grow new semimagnetic materials containing Cr, Cu, Fe, Cd and Ni. We also give our results on annealing, used to change the carrier density and to improve the electron mobility.

Chapter 6 describes the experimental set-up for SdH and magnetisation measurements and the methods to analyse the results of these measurements.

Chapter 7 and 8 give the experimental results on  $\text{Hg}_{1-x}\text{Mn}_x\text{Se}$  and  $(\text{Cd}_{1-x}\text{Mn}_x)_3\text{As}_2$  respectively. In Chapter 7 we stress on the applica-

bility of our new bandstructure model described in Chapter 2. Also the effects of zero-field splitting are discussed.

Chapter 9 deals with distortions of the SdH signals due to carrier density inhomogeneities and superconducting phase transitions in contact solder materials.

Parts of this work have already been published [8-10].

### 1.1 History of SMSC

A long tradition exists in the research of II-VI semiconductors. Especially their ternary compounds like  $\text{Hg}_{1-x}\text{Cd}_x\text{Te}$  are widely investigated. The interest in these materials was stimulated by the possibility to use small-bandgap materials as infrared detectors. The bandgap can be adjusted by changing the composition, thus optimising the material as detector for specific infrared bands.

Although the idea to substitute mercury by manganese instead of cadmium in the II-VI compounds originates from 1963 [11], it lasted until the mid 1970's before this kind of material was prepared on a large scale. The Mn atoms are situated at random cation sites. Without external magnetic field the electronic properties of  $\text{Hg}_{1-x}\text{Mn}_x\text{Te}$ , such as the effective mass, resemble those of  $\text{Hg}_{1-y}\text{Cd}_y\text{Te}$ , in the case  $x$  and  $y$  are chosen such that both materials have an equal bandgap. However, the first magneto-optical measurements on  $\text{Hg}_{1-x}\text{Mn}_x\text{Te}$  [12] showed that in particular the behaviour of the spin states changes compared to the situation in  $\text{Hg}_{1-y}\text{Cd}_y\text{Te}$ . Later experiments showed that these spin states become strongly temperature dependent [13]. These anomalous spin effects were interpreted as the manifestation of the exchange interaction between the spins of the mobile band electrons and the spins of the d-electrons of the localised Mn atoms.

The family of SMSC is of course not limited to  $\text{Hg}_{1-x}\text{Mn}_x\text{Te}$  and  $\text{Cd}_{1-x}\text{Mn}_x\text{Te}$ . All Mn based semimagnetic compounds of the II-VI family are shown in fig. 1.1. This figure also shows the limits of solubility of Mn into these compounds. The new spin related phenomena stimulated also the search for semimagnetic compounds in the IV-VI family of lead salts, such as  $\text{Pb}_{1-x}\text{Mn}_x\text{Te}$  [14] and  $\text{Pb}_{1-x}\text{Mn}_x\text{S}$  [15]. II-V compounds like  $(\text{Cd}_{1-x}\text{Mn}_x)_3\text{As}_2$  [16] and  $(\text{Zn}_{1-x}\text{Mn}_x)_3\text{As}_2$  were prepared in the group

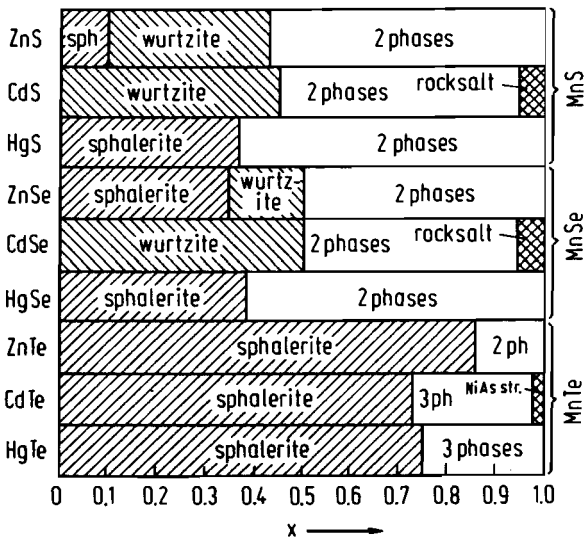


Fig. 1.1  
Solubility of Mn chalcogenides with II-VI compounds and resulting crystal structures.  $x$ : mole fraction of Mn chalcogenide.

Semiconductor Physics at the University of Technology in Eindhoven. For all these materials the exchange interaction between the spins of the band electrons and the spins of the Mn atoms is studied experimentally.

### 1.2 Bandstructure and exchange interaction

Kossut [17] has shown that this exchange interaction can be described theoretically by the Heisenberg type Hamiltonian

$$H_{\text{ex}} = \sum_{\mathbf{R}_i} J(\mathbf{r} - \mathbf{R}_i) \mathbf{S}_i \cdot \sigma \quad (1.1)$$

where  $J(\mathbf{r} - \mathbf{R}_i)$  is an exchange integral centered at site  $\mathbf{R}_i$ ,  $\mathbf{S}_i$  is the spin operator of the localised spin of the Mn atom at site  $\mathbf{R}_i$ , and  $\sigma$  is the spin operator of the mobile electron. The Hamiltonian in eq. 1.1 is averaged over the positions  $\mathbf{R}_i$  and over the values of the localised spins. This is justified by the argument that a mobile electron interacts simultaneously with a large number of manganese spins. In that case, the exchange contribution to the spin splitting

becomes proportional to the spin component parallel to the magnetic field  $\langle S_B \rangle$ .  $\langle S_B \rangle$  is directly related to the macroscopic magnetisation  $M$ , via  $M = -Ng\mu_B \langle S_B \rangle$ .  $N$  is the number of magnetic atoms in the crystal,  $g$  is the Landé factor and  $\mu_B$  the Bohr magneton. SMSC are mostly paramagnetic materials, whereas normal semiconductors are diamagnetic. The magnetisation of paramagnets depends strongly on temperature and magnetic field. Because the spin splitting is proportional to the magnetisation also the spin splitting varies rapidly with magnetic field and temperature. This strong variation of the spin splitting is a very characteristic property of SMSC.

The strength of the exchange interaction is described by two exchange integrals, usually denoted by  $\alpha$  and  $\beta$ . These parameters  $\alpha$  and  $\beta$  give the interaction strength between the localised magnetic atoms and the mobile band electrons with s and p-symmetric wave functions respectively.

The mechanism of the exchange interaction is not yet completely understood. The spatial range of  $J(\mathbf{r} - \mathbf{R})$  in eq. 1.1 is considered to be much smaller than the magnetic length  $\lambda = \sqrt{\hbar/eB}$  [13]. Theoretically the difference in sign and magnitude of the exchange parameters  $\alpha$  and  $\beta$  is ascribed either to the difference in overlap of the Mn 3d-electron wave functions with the wave functions of different symmetry of the band electrons [18] or to the hybridisation of the Mn 3d-levels with the valence band [19,20].

Experimentally the exchange interaction has been studied for a variety of materials using different methods. The first evidence for the validity of Kossut's theory was given in ref. [21]. This paper shows that the magnetisation and the exciton splitting measured for  $\text{Cd}_{1-x}\text{Mn}_x\text{Te}$  are proportional to each other. The second important aspect of this paper is that it gives a very useful semi-empirical formula to describe the magnetisation of SMSC. The Brillouin function, which is valid only for a system of non-interacting spins, is modified by introducing an adjustable saturation value of the magnetisation and an effective temperature to take into account the Mn-Mn spin interaction. By choosing these adjustable parameters temperature dependent, the modified Brillouin function gives a good description of the magnetisation in a broad range of magnetic field and temperature [22].

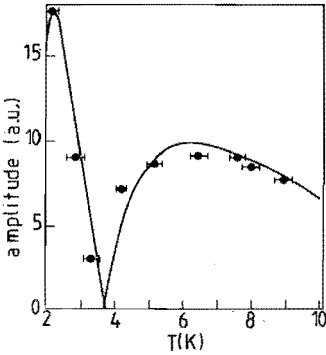


Fig. 1.2

Amplitude of SdH oscillations for  
 $\text{Hg}_{0.98}\text{Mn}_{0.02}\text{Te}$ ,  $n_e = 4.0 \cdot 10^{21} \text{ m}^{-3}$  [5].

The exchange interaction does not only influence magneto-optical phenomena but also quantum-transport phenomena. Ref. [5] reports on oscillations of the thermopower and on the SdH oscillations in the magnetoresistance in a degenerate semiconductor. In the magnetic field region where spin splitting of the magnetoresistance maxima is observed, the field positions of the peaks are strongly temperature dependent. For lower fields the amplitude of the SdH oscillations behaves non-monotonically as a function of temperature (Fig. 1.2). Even nodes in the oscillation amplitude can occur. Kossut [23] discusses the mechanism causing the nodes in the amplitude of the quantum oscillations. In a narrow-gap SMSC the spin splitting of a Landau level can surpass the splitting between adjacent Landau levels. The ratio  $\nu$  of these splittings can rapidly change due to the temperature dependence of the spin splitting, caused by the exchange interaction. Each time the splitting ratio  $\nu$  equals  $k + 1/2$ , with  $k$  being an integer value, a node occurs in the oscillation amplitude. Knowing the conditions for which nodes occur, one can in reverse use the occurrence of the nodes to study the spin splitting and consequently the exchange interaction in SMSC. Thus, the temperature dependence of the amplitude of SdH oscillations becomes a useful tool to study the exchange interaction. On the other hand, the nodes hamper the determination of the cyclotron effective mass from the temperature dependence of the oscillation amplitude like in ordinary semiconductors [24].

All the experiments mentioned above and many other magneto-optical and magneto-transport experiments aimed at a precise determination of

the values of the exchange integrals  $\alpha$  and  $\beta$ . These values are not yet well established experimentally. All authors agree that the signs for  $\alpha$  and  $\beta$  are opposite. However, the values of the exchange integrals for narrow-gap SMSC show a large scatter [1], which is unexplained until now. The scatter of the  $\alpha$  and  $\beta$  values leads to a clear need for more rigour in the experiments. Therefore we decided to re-examine some of these materials, emphasising in our experiments two aspects, which have been neglected by most other authors.

The first aspect is that most of the published values of  $\alpha$  and  $\beta$  were determined using magnetisation values, obtained from the interpolation of the results on other samples. Due to concentration gradients over the ingots, created during the crystal growth, it is very difficult to obtain an accurate value for the Mn concentration of the sample. This reduces the reliability of the interpolation. We avoid this problem by measuring the magnetisation on the same samples as used for the SdH experiments.

The second neglected aspect is the anisotropy of the spin splitting. Some of the host materials, on which the investigated SMSC are based, exhibit an anisotropic spin splitting. In the presence of Mn, where the spin splitting is enhanced by the isotropic exchange interaction, the splitting is still anisotropic. If one neglects the anisotropy, different spin splitting energies can be obtained experimentally for one single combination of temperature and magnetic field. It is evident that the interpretation of these results with an isotropic bandstructure model, as mostly has been done, leads to scatter in the values determined for the exchange integrals  $\alpha$  and  $\beta$ . To study the anisotropy effects of the spin splitting and the bandstructure in general, we performed our experiments on oriented single crystals.

We study the exchange interaction and the anisotropy of the bandstructure of two materials which look very promising with respect to the anisotropy aspect:  $\text{Hg}_{1-x}\text{Mn}_x\text{Se}$  and  $(\text{Cd}_{1-x}\text{Mn}_x)_3\text{As}_2$ .

$\text{Hg}_{1-x}\text{Mn}_x\text{Se}$  is based on HgSe. The host material has a cubic crystal structure. However, due to the lack of inversion symmetry in the zinc blende lattice, the spin splitting of the Landau levels is highly anisotropic [25]. Most of the papers on  $\text{Hg}_{1-x}\text{Mn}_x\text{Se}$  neglected the possible effects of anisotropy in the spin splitting [26-30]. The

first indication of anisotropy was given by Reifenberger and Schwarzkopf [31]. We also observed a strong anisotropy in the positions of the nodes in the SdH oscillation amplitude. The modified Pidgeon Brown model [5,32], which is used by most authors to interpret their data on narrow-gap SMSC, cannot explain this anisotropy. We thus developed a new model. Contrary to the Pidgeon Brown model we took into account the inversion asymmetry, because it is responsible for the strong anisotropy of the spin splitting. Our new model is based on a paper by Weiler et al. [33], where the complete Hamiltonian for the zinc blende structure is given, including inversion asymmetry effects. To explain the observed temperature dependence of the spin splitting as well, we extended this model by including the exchange interaction, typical for SMSC. Our new model accounts for both the temperature dependence and the anisotropy of the nodes observed in the SdH oscillation amplitude.

$(\text{Cd}_{1-x}\text{Mn}_x)_3\text{As}_2$  is based on the host material  $\text{Cd}_3\text{As}_2$ . This semiconductor is a zero-gap material with a tetragonal crystal structure, resulting in a highly anisotropic bandstructure [34] with an anisotropic spin splitting [35]. Also the bandstructure of the semimagnetic compound is predicted to be highly anisotropic [36]. Some experimental evidence for this anisotropy in  $(\text{Cd}_{1-x}\text{Mn}_x)_3\text{As}_2$  is given in [37]. We collected data from a set of samples with different Mn concentrations. These data showed only a small anisotropy, which decreased with increasing Mn concentration. A complete study of the composition dependence of the anisotropic bandparameters and of the exchange integrals  $\alpha$  and  $\beta$  turned out to be seriously hampered by technological problems, causing gradients of the carrier density and the Mn concentration in the crystals. Therefore we decided to interpret our data on  $(\text{Cd}_{1-x}\text{Mn}_x)_3\text{As}_2$  with an isotropic bandstructure model.

### 1.3 Trends in research and applications of SMSC

After having related the work in this thesis to other work on SMSC we discuss some new trends in the research and some applications of this class of materials at present.



## Zero-field splitting

Surprisingly after the initial success of Kossut's description of the exchange interaction [17] a discrepancy between this theory and the experiments was reported. The macroscopic magnetisation of SMSC is zero in the absence of a magnetic field and according to Kossut's theory the effects of the exchange interaction on the spin splitting should therefore also vanish in that case. However, in spin flip Raman scattering experiments on  $\text{Cd}_{1-x}\text{Mn}_x\text{Se}$ , a finite spin splitting for electrons bound to donors was observed in the absence of a magnetic field [38]. This so-called zero-field splitting is explained in terms of a bound magnetic polaron (BMP) where the spin of the electron bound to a donor aligns the Mn spins in a region surrounding the donor. The alignment results in a local magnetisation which induces a non-zero electron spin splitting [39].

Soon after this discovery, evidence for the existence of a free magnetic polaron was found [40,41]. Interband magneto-optical measurements on  $\text{Pb}_{1-x}\text{Mn}_x\text{Te}$  showed a finite splitting of the spin levels of free band electrons at zero field, indicating that the spin splitting is no longer completely proportional to the externally measured magnetisation [40]. The most direct proof of this zero-field splitting is the occurrence of the splitting of the zero-field spectra emitted by a  $\text{Pb}_{1-x}\text{Mn}_x\text{S}$  diode laser [41]. The splitting of the spectra is explained by finite spin splittings of the valence and the conduction band, allowing four electron-hole recombination energies. The four energies correspond to four wavelengths in the emission spectra. The splitting of the bands is proportional to the Mn concentration and does not occur in spectra of pure PbS lasers. Also for  $\text{Hg}_{1-x}\text{Mn}_x\text{Te}$  [42] and  $\text{Hg}_{1-x}\text{Mn}_x\text{Se}$  [43] indications for zero-field splitting were reported. Despite considerable efforts to describe the free magnetic polarons theoretically [44-46], a generally accepted theory has not yet been developed.

Most of the experiments mentioned above, showed the effects of the free magnetic polaron in the presence of a magnetic field. This means that these effects might influence the SdH oscillations as well. Due to the free magnetic polaron the spin splitting can increase up to a few meV at low magnetic fields. Therefore we have to pay attention to

this effect for an accurate determination of the exchange integrals from the spin splitting.

#### *New materials*

The logical extension of the research of Mn based ternary semiconducting compounds is the investigation of quaternary compounds like  $\text{Hg}_{1-x-y}\text{Cd}_y\text{Mn}_x\text{Te}$ . By changing the Cd concentration the energy bandgap can be varied independently of the Mn concentration. Thus one can check whether the bandgap influences the exchange integrals  $\alpha$  and  $\beta$ , for a constant Mn concentration. Also the dependence of  $\alpha$  and  $\beta$  on the Mn composition can be studied for a fixed bandgap. However, the reported values for  $\alpha$  and  $\beta$  [47,48] show a similar scatter as in the ternary compounds and so far no conclusions can be drawn from these experiments.

Apart from Mn there are of course other elements which can introduce localised magnetic moments in semiconductors. The lead salts  $\text{Pb}_{1-x}\text{Eu}_x\text{Te}$  [49] and  $\text{Pb}_{1-x}\text{Cd}_x\text{Te}$  [50] are reported to be SMSC. In contrast to Mn ions, where the magnetic moment originates from the 3d-shell, the magnetic moment in the rare earth ions Cd and Eu arises from the 4f-shell. The seven electrons in the half filled 4f-shell give rise to a spin of 7/2 instead of 5/2 for Mn. Furthermore the 4f-shell lies deep inside the ions while the 3d-shell of the transition metals is an external one. Thus Eu and Cd introduce new aspects in the study of the exchange interaction in these materials.

Also a few reports exist on  $\text{Hg}_{1-x}\text{Fe}_x\text{Te}$  [51] and  $\text{Zn}_{1-x}\text{Fe}_x\text{Se}$  [52]. Although the magnetic moments of Fe originate also from electrons in the 3d-shell,  $\text{Fe}^{2+}$  has six electrons in this shell. The ground state of the  $\text{Fe } 3d^6$  electronic configuration in a zinc blende lattice differs from that for  $\text{Mn } 3d^5$ . The  $\text{Fe } 3d^6$  ground states give rise to Van Vleck type paramagnetism, which is temperature independent. Therefore, exchange related effects are no longer temperature dependent in these Fe compounds.

A more intensively investigated Fe based material is  $\text{Hg}_{1-x}\text{Fe}_x\text{Se}$ . In this material Fe is a resonant donor, located in the conduction band [53]. This leads to stabilisation of a high carrier density [54]. Even at this high carrier density a remarkably high electron mobility was observed [55], which is explained by a space ordering in the

ionisation of the Fe donors [56]. Such a periodic array of ionised impurities leads to a reduced scattering as compared to random ionisation. The ionised donors are in the  $\text{Fe}^{3+}$  state.  $\text{Fe}^{3+}$  has the same  $3d^5$  configuration as Mn, and  $\text{Fe}^{3+}$  yields a similar temperature dependent magnetic behaviour [57]. Therefore spin related phenomena in  $\text{Hg}_{1-x}\text{Fe}_x\text{Se}$  can be temperature dependent, in contrast to  $\text{Hg}_{1-x}\text{Fe}_x\text{Te}$  and  $\text{Zn}_{1-x}\text{Fe}_x\text{Se}$ . In  $\text{Hg}_{1-x}\text{Fe}_x\text{Se}$  a strong anisotropy of the positions of the nodes in the SdH oscillation amplitude is reported [58,59]. Like in  $\text{Hg}_{1-x}\text{Mn}_x\text{Se}$  this anisotropy is related to the lack of inversion symmetry in the zinc blende lattice of HgSe.

### *Superlattices and heterostructures*

Recently the successful preparation of SMSC superlattices and heterostructures by molecular beam epitaxy has been reported [60], opening a new research area.

Analogous to the III-V  $\text{GaAs}/\text{AlGa}_{1-x}\text{As}$  quantum wells  $\text{CdTe}/\text{Cd}_{1-x}\text{Mn}_x\text{Te}$  wells are produced. Soon after the first reports on laser action in these structures [61] the tunability of the emitted laser radiation by an external magnetic field was reported [62].

A so-called spin superlattice was proposed in ref. [63]. The two materials of which this superlattice consists are to be chosen such that the orbital properties of the electrons are equal, but the spin properties are different. This can be done by stacking layers of non-magnetic  $\text{Hg}_{1-x}\text{Cd}_x\text{Se}$  and semimagnetic  $\text{Hg}_{1-y}\text{Mn}_y\text{Se}$ . The values of x and y are determined by the condition that the energy band gap must be equal for both materials. Due to the exchange interaction in the layers of  $\text{Hg}_{1-x}\text{Mn}_x\text{Se}$  the spin splitting of the electron energy levels varies periodically in the growth direction. Since the possibility of growing layers of Hg based SMSC has been demonstrated [64], the growth of spin superlattices can be expected in the near future.

The growth of high quality heterojunctions should allow the observation of the quantum Hall effect in semimagnetic II-VI structures. In fact the observation of the quantum Hall effect in SMSC has already been reported [65]. In these experiments the two-dimensional electron gas was formed in an inversion layer on a grain boundary in polycrystalline  $\text{Hg}_{1-x}\text{Mn}_x\text{Te}$ . The possibility in SMSC to influence the spin level splitting separately from the Landau splitting via the exchange

interaction, might increase the understanding of the spin behaviour of a two-dimensional electron gas.

#### *Magnetic properties studied by electron spin properties*

Due to the exchange interaction the electronic properties are strongly influenced by the magnetic atoms. Therefore, an anomaly in the behaviour of the magnetic system can result in an anomaly of the electron behaviour. This means that the study of the electronic properties can yield information on anomalies in the magnetic properties.

Faraday rotation is used to detect spin-glass transitions in  $\text{Hg}_{1-x}\text{Mn}_x\text{Te}$  [66,67] and  $\text{Cd}_{1-x}\text{Mn}_x\text{Te}$  [68]. Furthermore, Faraday rotation can be used to study the relaxation behaviour of the localised spins near the spin-glass transition [69].

Also the Hall effect can be used to detect the spin-glass transition [70]. For example in experiments on  $\text{Hg}_{1-x}\text{Mn}_x\text{Te}$  under hydrostatic pressure, it is much easier to detect the spin-glass transition by an anomaly in the Hall effect than by the usual susceptibility measurement. These experiments are of interest, because hydrostatic pressure changes the bandgap, which causes a shift of the freezing temperature where the spin-glass transition occurs [71].

#### *Influence of electron spins on the Mn spins*

Via the very same spin exchange interaction, which transfers the influence of the magnetic system to the band electrons, the band electrons can also influence the magnetic system. Usually the localised spins dominate the band electron spins. Recently an experiment on  $\text{Hg}_{0.88}\text{Mn}_{0.12}\text{Te}$  in which the opposite occurs has been published [72]. Electrons are pumped from the valence band to the conduction band by polarised laser radiation. This causes a polarisation of the free carriers in the direction of the light propagation. Via the exchange interaction this leads to an orientation of the Mn ions. The magnetic moment of the oriented Mn spins is measured with a SQUID (superconducting quantum interference device). Measurements on  $\text{Hg}_{1-x}\text{Cd}_x\text{Te}$  and InSb, showed no magnetisation, thus proving that the magnetisation is caused by the alignment of Mn spins.

Another effect in which electrons influence the magnetic behaviour was published by Story et al. [73]. In  $\text{Pb}_{1-x-y}\text{Sn}_x\text{Mn}_y\text{Te}$  a ferromagnetic

phase transition occurs as a function of the carrier density. Although the abruptness of the transition is not yet understood, the influence of the carriers on the magnetic properties is related to the RKKY interaction, where the Mn-Mn interaction is mediated via the band electrons.

#### *Dynamics of the exchange interaction*

The study of the dynamic behaviour of the exchange interaction has only just started. Two independent experiments measured the time scale on which aligned localised Mn spins orient the mobile electron spins.

Awschalom et al. [74] use picosecond laser pulses to create excitons. In these excitons a large Zeeman splitting occurs due to the exchange interaction. This splitting grows with increasing polarisation of the spins of the electrons involved. The time dependence of the growth of the splitting is monitored by measuring the Faraday rotation of delayed probe laser pulses transmitted through the sample. In  $\text{Cd}_{0.82}\text{Mn}_{0.18}\text{Te}$  the time needed to reach maximum polarisation is about 300 ps, which is much longer than the exciton creation time of 20 ps [74]. For lower Mn concentrations more than 300 ps is needed to reach maximum polarisation.

A similar experiment on  $\text{Cd}_{1-x}\text{Mn}_x\text{Se}$  has been reported by Zayhowski et al. [75]. They studied the photoluminescence spectra of excitons as a function of time. The excitons were created by 5 ps laser pulses. After creation of the excitons the luminescence peak energy shifts as a function of time. The maximum energy shift is the same as measured in the case of continuous illumination. The time in which the maximum shift (and maximum electron spin polarisation) is reached, is of the same order of magnitude as for  $\text{Cd}_{1-x}\text{Mn}_x\text{Te}$ . Again the polarisation speed depends on the Mn concentration.

Studies of the dynamic behaviour will result in a more detailed description of the exchange interaction, than the usual model with the static exchange integrals  $\alpha$  and  $\beta$ .

#### *Applications*

Analogous to the  $\text{Hg}_{1-x}\text{Cd}_x\text{Te}$  compounds  $\text{Hg}_{1-x}\text{Mn}_x\text{Te}$  looks very promising for the application as infrared detector. The advantage of semimagnetic over non-magnetic materials is that the addition of Mn

atoms yields the possibility of tuning the sensitivity by an external magnetic field. The preparation and performance of the first semimagnetic infrared detector was reported in ref. [76]. For further progress in the application of SMSC a clear understanding of the behaviour of impurities and defects is necessary. A great deal of knowledge concerning doping and annealing is already gathered from experiments on non-magnetic materials. However, although the electronic properties of semimagnetic compounds resemble in general those of the host materials, there are also some striking differences. Due to the effect of the spin exchange on acceptor levels, an extremely large negative magnetoresistance occurs in  $\text{Hg}_{1-x}\text{Mn}_x\text{Te}$  [77]. In the field range from 0 to 7 T, the resistance drops over 6 orders of magnitude. This large negative magnetoresistance limits the magnetic field range in which  $\text{Hg}_{1-x}\text{Mn}_x\text{Te}$  detectors can be used. On the other hand the new effects due to the exchange interaction provide new tools to study the behaviour of donors and acceptors in II-VI compounds [78].

## REFERENCES

- [1] N.B. Brandt, V.V. Moshchalkov, *Advances in Physics* 33, 193 (1984).
- [2] I.I. Lyapilin, I.M. Tsidilkovskii, *Sov. Phys. Usp.* 28, 349 (1985).
- [3] M. Dobrowolska, H.D. Drew, J.K. Furdyna, T. Ichiguchi, A. Witowski, P.A. Wolff, *Phys. Rev. Lett.* 49, 845 (1982).
- [4] J.A. Caj, R.R. Gałazka, M. Nawrocki, *Sol. St. Comm.* 25, 193 (1978).
- [5] M. Jaczynski, J. Kossut, R.R. Gałazka, *Phys. Stat. Sol. (b)* 88, 73 (1978).
- [6] C.J.M. Denissen, Ph.D. thesis, Eindhoven University of Technology, Eindhoven, 1986.
- [7] R.R. Gałazka, in *Lecture Notes in Physics* no 152 (Springer Verlag, Berlin 1982) p. 294.
- [8] H.M.A. Schleijsen, F.A.P. Blom, *Phys. Stat. Sol. (b)* 135, 605 (1986).
- [9] H.M.A. Schleijsen, F.A.P. Blom, J.H. Wolter, *Sol. St. Comm.* 61, 231 (1987).
- [10] A.W. Buij, H.M.A. Schleijsen, F.A.P. Blom, *J. Appl. Phys.* 59, 4108 (1986).
- [11] R.T. Delves, B. Lewis, *Physics Chem. Solids* 24, 549 (1963).
- [12] G. Bastard, C. Rigaux, A. Mycielski, *Phys. Stat. Sol. (b)* 79, 585 (1977).
- [13] G. Bastard, C. Rigaux, Y. Guldner, J. Mycielski, A. Mycielski, *Journal de Physique*, 39, 87 (1978).
- [14] J. Niewodniczanska-Zawadzka, J. Kossut, A. Sandauer, W. Dobrowolski in *Lecture Notes in Physics* no 152 (Springer Verlag, Berlin 1982) p. 326.
- [15] G. Karczewski, M. Klimkiewicz, I. Glass, A. Szerbakow, R. Behrendt, *Appl. Phys. A* 29, 49 (1982).
- [16] J.J. Neve, C.J.R. Bouwens, F.A.P. Blom, *Sol. St. Comm.* 38, 27 (1981).
- [17] J. Kossut, *Phys. Stat. Sol. (b)* 78, 537 (1976).

- [18] Yu. G. Semenov, B.D. Shanina, Phys. Stat. Sol. (b) 104, 631 (1981).
- [19] A.K. Bhattacharjee, G. Fishman, B. Coqblin, Physica 117B & 118B, 449 (1983).
- [20] K.C. Hass, B.E. Larsson, H. Ehrenreich, A.E. Carlsson, J. Magn. Mater. 54-57, 1283 (1986).
- [21] J. Gaj, R. Planel, G. Fishman, Sol. St. Comm. 29, 435 (1979)
- [22] W. Dobrowolski, M. v. Ortenberg, A.M. Sandauer, R.R. Gałazka, A. Mycielski, R. Pauthenet in Lecture Notes in Physics no 152 (Springer Verlag, Berlin 1982) p. 302.
- [23] J. Kossut, Sol. St. Comm. 27, 1237 (1978).
- [24] M. Jaczynski, W. Dobrowolski, Phys. Stat. Sol. (b) 102, 195 (1980).
- [25] D.C. Seiler, R.R. Gałazka, W.M. Becker, Phys. Rev. B3, 4274 (1971).
- [26] S. Takeyama, R.R. Gałazka, Phys. Stat. Sol. (b) 96, 413 (1979).
- [27] P. Byszewski, M.Z. Cieplak, A. Mongird-Gorska, J. Phys. C: Sol. State Phys. 13, 5383 (1980).
- [28] I.I. Lyapilin, A.I. Ponomarev, G.I. Kharus, N.P. Cavaleshko, P.D. Maryanchuk, Sov. Phys. JETP 58, 953 (1983).
- [29] M. Dobrowolska, W. Dobrowolski, R.R. Gałazka, A. Mycielski, Phys. Stat. Sol. (b) 105, 477 (1981).
- [30] A. Witowski, K. Pastor, J.K. Furdyna, Phys. Rev. B26, 931 (1982).
- [31] R. Reifengerger, D.A. Schwarzkopf, Phys. Rev. Lett. 50, 907 (1983).
- [32] C.R. Pidgeon, R.N. Brown, Phys. Rev. 146, 575 (1966).
- [33] M.H. Weiler, R.L. Aggarwal, B. Lax, Phys. Rev. B17, 3269 (1978).
- [34] J. Bodnar, Proc. Int. Conf. Phys. Narrow-Gap Semicond., Warsaw 1977 (Polish Scientific Publ., Warsaw, 1978) p. 311.
- [35] P.R. Wallace, Phys. Stat. Sol. (b) 92, 49 (1979).
- [36] J.J. Neve, J. Kossut, C.M. v. Es, F.A.P. Blom, J. Phys. C: Sol. State Phys. 15, 4795 (1982).
- [37] J.J. Neve, Ph.D. thesis, Eindhoven University of Technology, Eindhoven, 1984.
- [38] M. Nawrocki, R. Planel, G. Fishman, R. Gałazka, Phys. Rev. Lett. 46, 725 (1981).



- [39] R. Planel in Lecture Notes in Physics no. 177 (Springer Verlag, Berlin 1983) p. 441.
- [40] H. Pascher, E.J. Fantner, G. Bauer, W. Zawadzki, M. v. Ortenberg, Sol. St. Comm. 48, 461 (1983).
- [41] G. Karczewski, L. Kowalczyk, Sol. St. Comm. 48, 653 (1983).
- [42] R. Stepniewski, Acta Physica Polonica A69, 1001 (1986).
- [43] W. Staguhn, Ph.D. thesis, Julius Maximilians Universität, Würzburg, 1984.
- [44] M. v. Ortenberg, Sol. St. Comm. 52, 111 (1984).
- [45] A. Golnik, A. Twardowski, J. Gaj, J. Cryst. Growth 72, 376 (1985).
- [46] R. Stepniewski, Sol. St. Comm. 58, 19 (1986).
- [47] J. Niewodniczanska-Zawadzka, T. Piotrowski, J. Kossut, J. Cryst. Growth 72, 398 (1985).
- [48] N. Miura, S. Takeyama, S. Tanaka, N. Yamada, Proc. 18th Int. Conf. on the Phys. of Semicond., Stockholm, 1986. ( World Scientific Publ. Co. Singapore 1987 ), p. 1775.
- [49] R. Faymonville, B. Harbecke, A. Krost, K.E. Ambrosch, E. Fantner, G. Bauer, Verhandlungen der DPG, Frühjahrstagung Freudenstadt 1983, Festkörper Physik, p. 646.
- [50] M. Averous, B.A. Lombos, C. Fau, E. Ilbnoelghazi, J.C. Tedenac, G. Brun, M.A. Bartkowski, Phys. Stat. Sol. (b) 131, 759 (1985).
- [51] S. Abdel-Maksoud, C. Fau, J. Calas, M. Averous, B. Lombos, G. Brun, J.C. Tedenac, Sol. St. Comm. 54, 811 (1985) and references therein.
- [52] A. Twardowski, M. v. Ortenberg, M. Demianiuk, J. Cryst. Growth 72, 401 (1985).
- [53] A. Mycielski, P. Dzwonkowski, B. Kowalski, B.A. Orlowski, M. Dobrowolska, M. Arciszewska, W. Dobrowolski, J.M. Baranowski, J. Phys. C: Sol. State Phys. 19, 3605 (1986).
- [54] M. Vaziri, U. Debska, R. Reifenberger, Appl. Phys. Lett. 47, 407 (1985).
- [55] M. Vaziri, R. Reifenberger, Phys. Rev. B32, 3291 (1985).
- [56] J. Mycielski, Sol. St. Comm. 60, 165 (1986).

- [57] M. Vaziri, D.A. Schwarzkopf, R. Reifenger, Phys. Rev. B31, 3811 (1985).
- [58] M. Vaziri, R. Reifenger, Phys. Rev. B33, 5585 (1985).
- [59] N.C. Gluzman, L.D. Sabirzyanova, I.M. Tsidilkovskii, L.D. Paranchich, S.Yu. Paranchich, Sov. Phys. Semicond. 20, 55 (1986).
- [60] L.A. Kolodziejski, T. Sakamoto, R.L. Gunshor, S. Datta, Appl. Phys. Lett. 44, 799 (1984).
- [61] R.N. Bicknell, N.C. Giles-Taylor, D.K. Blanks, J.F. Schetzina, N.C. Anderson, W.D. Laidig, Appl. Phys. Lett. 46, 1122 (1985).
- [62] E.D. Isaacs, D. Heiman, J.J. Zayhowski, R.N. Bicknell, J.F. Schetzina, Appl. Phys. Lett. 48, 275 (1986).
- [63] M. v. Ortenberg, Phys. Rev. Lett. 49, 1041 (1982).
- [64] K.A. Harris, S. Hwang, Y. Lansari, J.W. Cook, J.F. Schetzina, Appl. Phys. Lett. 49, 713 (1986).
- [65] T. Dietl, Symposium on Semimagnetic Semiconductors Aussois, France, 1985, unpublished.  
G. Grabecki, T. Suski, T. Dietl, T. Skoskiewicz, J. Przeor, 15th School on the Physics of Semiconducting compounds, Jaszowiec Ustron 1986, to be published in Acta Physica Polonica.
- [66] A. Mycielski, C. Rigaux, M. Menant, T. Dietl, M. Otto, Sol. St. Comm. 50, 257 (1984).
- [67] C. Rigaux, A. Mycielski, G. Barilero, M. Menant, Phys. Rev. B34, 3313 (1986).
- [68] E. Kierzek-Pecold, W. Szymanska, R.R. Gałazka, Sol. St. Comm. 50, 685 (1984).
- [69] M. Ayadi, J. Ferré, A. Mauger, R. Triboulet, Phys. Rev. Lett. 57, 1165 (1986).
- [70] N.B. Brandt, V.V. Moshchalkov, L. Skrbek, A.N. Taldenkov, S.M. Chudinov, JETP Lett. 35, 401 (1982).
- [71] N.B. Brandt, V.V. Moshchalkov, A.O. Orlov, L. Skrbek, I.M. Tsidilkovskii, S.M. Chudinov, Sov. Phys. JETP 57, 614 (1983).
- [72] H. Krenn, W. Zawadzki, C. Bauer, Phys. Rev. Lett. 55, 1510 (1985).

- [73] T. Story, R.R. Gałazka, R.B. Frankel, P.A. Wolff, Phys. Rev. Lett. 56, 777 (1986).
- [74] D.D. Awschalom, J.H. Halbout, S. von Molnar, T. Siegrist, F. Holtzberg, Phys. Rev. Lett. 55, 1128 (1985).
- [75] J.J. Zayhowski, C. Jagannath, R.N. Kershaw, D. Ridgley, K. Dwight, A. Wold, Sol. St. Comm. 55, 941 (1985).
- [76] P. Becla, J. Vac. Sci. Technol. A4, 2014 (1986).
- [77] T. Wojtowicz, A. Mycielski, Physica 117B & 118B, 476 (1983).
- [78] J. Mycielski in Lecture Notes in Physics 177 (Springer Verlag, Berlin 1983) p. 431.

## CHAPTER II THE SHUBNIKOV DE HAAS EFFECT.

The Shubnikov de Haas effect is the oscillatory behaviour of the magnetoresistance appearing in degenerate semiconductors or semimetals at low temperatures and in high magnetic fields. The first observations of oscillations in the electrical resistivity as a function of the magnetic field were reported by Shubnikov and de Haas [1] in 1930. The origin of these oscillations was not understood at that time. The basis of the explanation was given by Landau [2] and Peierls [3] who predicted the splitting of the energy bands in a set of subbands in the presence of a magnetic field. It lasted until the late 1950's before the first quantitative theories of the SdH effect were published by Argyres [4] and Adams and Holstein [5]. Reviews on theory and experiments were given by Landwehr [6], Roth and Argyres [7] and Hajdu and Landwehr [8].

In this chapter we first explain the origin of the SdH effect using the free electron model. The second part of this chapter gives an analytical expression for the SdH oscillations. The third part discusses the effects of the electron spin level splitting on the SdH oscillation amplitude. In the last part we relate the spin splitting to bandstructure effects.

### 2.1 The free electron model for the Shubnikov de Haas oscillations

The origin of the SdH oscillations can be easily understood from the motion of a free electron gas in a magnetic field. In the case of a n-type semiconductor, with an isotropic parabolic bandstructure, the effective mass approximation can still be used and the energies of the electrons in the presence of a magnetic field  $B$  parallel to the  $z$ -axis are given by

$$E = \hbar\omega_c (n + 1/2) + \frac{\hbar^2 k_z^2}{2m^*} \pm \frac{g^* \mu_B B}{2}, \quad n = 0, 1, 2, \dots \quad (2.1)$$

This is a series of equidistant subbands separated by the Landau splitting  $\Delta E_L = \hbar\omega_c$ , where  $\omega_c = eB/m^*$  is the cyclotron frequency. The last term in eq. 2.1 represents the spin splitting of the Landau levels:  $\Delta E_{sp} = g^* \mu_B B$ , where  $g^*$  is the effective g-factor.

As a consequence of the quantisation of the electron motion perpendicular to the magnetic field, the density of states as a function of energy changes drastically in the presence of a magnetic field. Without field the electron states are uniformly distributed in k-space. In the presence of a magnetic field parallel to the z-direction, the occupied electron states lie on a series of coaxial cylinders, around the  $k_z$ -axis. In a degenerate system only k-states lying inside the Fermi surface are occupied. The density of states is now given by [9]

$$g(E) = \frac{1}{4\pi^2} \left[ \frac{2m^*}{\hbar} \right]^{3/2} \sum_{n=0}^{\infty} \sum_{+,-} \frac{\hbar \omega_c}{(E - (n+1/2)\hbar\omega_c \pm g^* \mu_B B/2)^{1/2}} \quad (2.2)$$

This function is plotted in fig. 2.1. At the bottom of each subband, where the energy equals  $(n+1/2)\hbar\omega_c \pm g^* \mu_B B/2$ ,  $g(E)$  shows a singularity. For simplicity the effective g-factor is taken equal to zero in fig. 2.1.

In real solids the electrons will be scattered, resulting in level broadening. Taking into account this level broadening, the singularities will disappear. Maxima in the density of states will persist as long as the energy separation of the levels is much larger than the level broadening  $k_B T$ . Thus the first condition for the observation of the SdH effect is given by

$$\hbar\omega_c \gg k_B T \quad (2.3)$$

The second condition for a quantised motion of the electrons in a plane perpendicular to the magnetic field, is given by the fact that the electrons must be able to perform complete cyclotron orbits, before being scattered. Under the assumption of an electron relaxation time  $\tau$ , this condition can be written as

$$\omega_c \tau > 1 \quad (2.4)$$

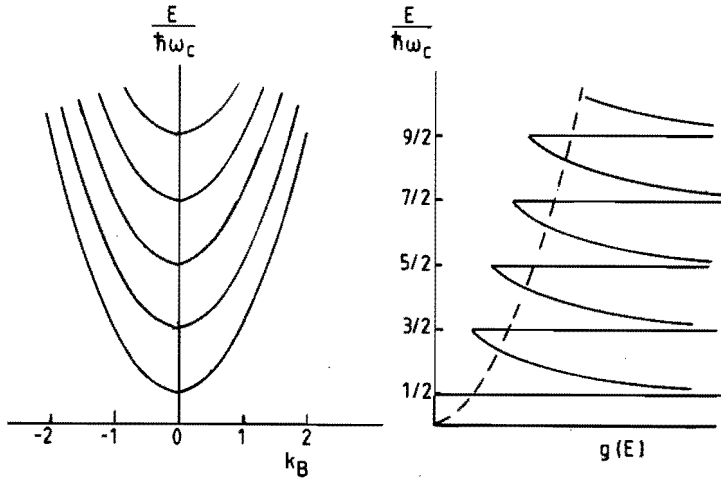


Fig. 2.1 Energy levels (a) and density of states  $g(E)$  (b) in a magnetic field. The dashed curve in (b) gives the density of states without magnetic field.

Under the conditions given by eq. 2.3 and 2.4 the density of states shows maxima at the bottom of the magnetic subbands. When the magnetic field increases, the level separation increases. Now each time the bottom of a subband crosses the Fermi energy  $E_F$ , a maximum in the density of states crosses the Fermi energy. Therefore, an increase of the magnetic field causes periodic variations of the density of states at the Fermi energy. These variations affect the electron scattering, giving rise to periodic oscillations in the resistance [4].

In fact the Fermi energy depends on the magnetic field in an oscillatory manner as well. However, when the number of Landau levels below the Fermi energy is sufficiently large, the oscillatory behaviour of the Fermi energy can be neglected. This condition can be written as

$$E_F \gg \hbar\omega_c \quad (2.5)$$

In general the conditions 2.3, 2.4 and 2.5 are fulfilled in our experiments on degenerate n-type semiconductors with a high electron mobility at low temperatures and high magnetic fields.

Assuming now that the Fermi energy remains constant when the magnetic field increases, it is easily seen that the oscillations are periodic in  $1/B$ . In general the oscillation period  $P$  is directly related to the geometry of the Fermi surface by the relation [10]

$$P = \left[ \frac{2\pi e}{\hbar S_m} \right]_{E=E_F} \quad (2.6)$$

where  $S_m$  is the extremal cross sectional area of the Fermi surface perpendicular to the magnetic field. In the case of a non-spherical Fermi surface,  $S_m$  and consequently  $P$  depend on the orientation of the crystal with respect to the magnetic field (fig. 2.2). The other way around the anisotropy of the oscillation period can then be used to determine the orientation of the crystals.

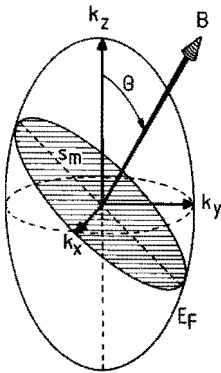


Fig. 2.2  
Extremal cross sectional area  $S_m$   
of the Fermi surface perpendicular  
to the magnetic field  $B$ .

For a spherical Fermi surface,  $S_m$  equals  $\pi k_F^2$  where  $k_F$  is the  $k$ -value at the Fermi surface. In that case  $P$  depends only on the electron density  $n_e$

$$P = \frac{2 e}{\hbar} \left[ 3\pi^2 n_e \right]^{-2/3} \quad (2.7)$$

## 2.2 Quantitative expression for the Shubnikov de Haas oscillations

Adams and Holstein [5] were the first to develop a quantum theory of electrical conduction in crossed electric and magnetic fields. Their expression for the oscillatory part of the conductivity consists of two contributions. One contribution originates from the scattering of electrons between different subbands. The other contribution arises from electron scattering within the subbands. The second contribution becomes only important for the lowest quantum numbers  $n$ , and will therefore be omitted in our case.

The resulting expression for the oscillatory part of the transverse magnetoresistance obtained by Adams and Holstein has been generalised by Lifshitz and Kosevich who included effects of anisotropic and non-parabolic bands [11]. Dingle took into account the collision broadening [12] and Cohen and Blount introduced the effects of spin splitting [13]. The analytical expression for the SdH oscillations then becomes [9]

$$\frac{\Delta\rho}{\rho_0} = \frac{c}{\hbar} \frac{k_0}{e} \frac{T}{m_0} \frac{m_c^*}{m_0} \left(\frac{P}{B}\right)^{1/2} \sum_{r=1}^{\infty} \left[ \frac{r^{1/2} e^{-r\beta m_c^* T_D / (m_0 B)}}{\sinh(r\beta m_c^* T / (m_0 B))} \right]^* \cos\left[\frac{2\pi r}{PB} - \frac{\pi}{4} - 2\pi r\gamma\right] \cos(r\pi\nu) \quad (2.8)$$

where  $\beta = 2\pi^2 m_0 k_0 / (\hbar e) = 14.693 (T/K)$  and  $c = 5\pi^2 / \sqrt{2}$ .  $\rho_0$  is the classical magnetoresistance.  $T_D = \hbar / (\pi k_0 \tau)$  is the Dingle temperature, describing the effect of collision broadening of the levels.  $P$  is the oscillation period and  $m_c^*$  is the cyclotron effective mass.  $\gamma$  is a phase factor which is 1/2 for a parabolic band. For other bandstructures the deviation of  $\gamma$  from 1/2 depends on energy and magnetic field [14]. However, this deviation is shown to be very small [15].  $\nu$  is the ratio between the spin splitting and the Landau splitting, given by  $\nu = g^* \mu_B B / (\hbar \omega_c) = \frac{1}{2} (m_c^* / m_0) g^*$ . In the derivation of eq. 2.8 the amplitudes of the oscillations due to the scattering of electrons with spin-up and spin-down are assumed to be equal.



A similar expression for the longitudinal magnetoresistance oscillations was obtained by Argyres [4]. In that case the constant  $c$  equals  $\pi^2/\sqrt{2}$ . The intra-subband scattering contribution which has been neglected for the transverse case does not exist in the longitudinal case.

### 2.3 Spin effects on the Shubnikov de Haas amplitude

In the theoretical expression for the SdH effect (eq. 2.8) the amplitude of each harmonic of the oscillations is multiplied by a factor  $\cos(\pi\nu)$ . This factor is introduced when the spin splitting is taken into account. Each time  $\nu$  equals  $k + 1/2$  with  $k$  being an integer value, the amplitude of the first harmonic vanishes. If the amplitudes of the higher harmonics are sufficiently damped a spin splitting zero or node in the SdH amplitude is observed. An example of such a SdH signal is given in fig. 2.3. The fact that the amplitude vanishes only over a small field range implies that  $\nu$  varies rapidly with magnetic field.

We follow the discussion of the mechanism which causes these nodes, as given by Kossut [16]. Fig. 2.4 gives a simplified picture of the broadened energy levels for different  $\nu$  values. The Landau splitting  $\hbar\omega_c$  is kept constant. The level broadening is chosen to be equal to  $\hbar\omega_c/2$ . For  $\nu = 0$  and  $\nu = 0.2$  the Landau levels are still separated. The splitting of the spin levels cannot be observed. For  $\nu = 0.5$  the

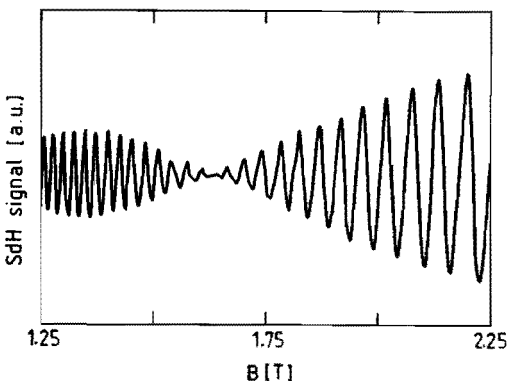


Fig. 2.3  
Typical SdH recorder trace in which a spin splitting node in the oscillation amplitude occurs.

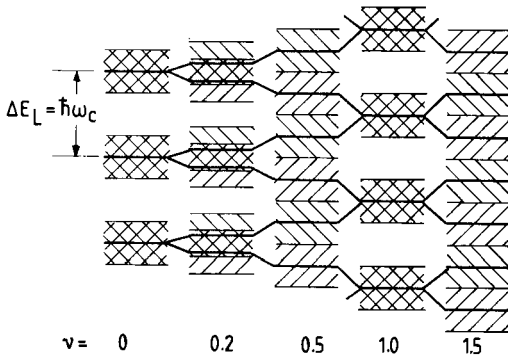


Fig. 2.4 Scheme of spin split Landau levels. The shaded areas represent the broadening of the levels, equal to half the Landau splitting. For  $\nu = 0, 0.2,$  and  $1$  the (nearly) degenerate levels can be observed separately. For  $\nu = 0.5$  and  $1.5$  the level broadening prevents the levels to be seen separately.

levels cannot be seen separately and therefore the amplitude of the SdH signal vanishes. For increasing values of  $\nu$ , these situations will alternately return. As can be seen from fig. 2.4, the interpretation of the spin splitting nodes is not unambiguous, because for each integer  $k$ -value in  $\nu = k + 1/2$ ,  $\nu$  satisfies the condition for the appearance of nodes. In the chapters on the experimental results we show how to solve this problem.

If the level broadening is smaller, the amplitude of the higher harmonics in the SdH signal is larger. In that case the spin splitting of the Landau levels can be observed directly, if the  $\nu$ -value is large enough. This is illustrated in fig. 2.5. Now the level broadening equals  $0.2 \hbar\omega_c$ . Up to  $\nu = 0.2$  the spin levels cannot be observed separately. For  $\nu = 0.5$  the levels are clearly separated and thus the oscillation frequency doubles. The doubling of the frequency vanishes again when the  $\nu$ -value approaches 1. An example of a SdH signal showing the oscillation frequency doubling is given in fig. 2.6.

In our experimental conditions the spin effects mostly result in a node in the SdH amplitude, whereas the frequency doubling occurs only rarely.

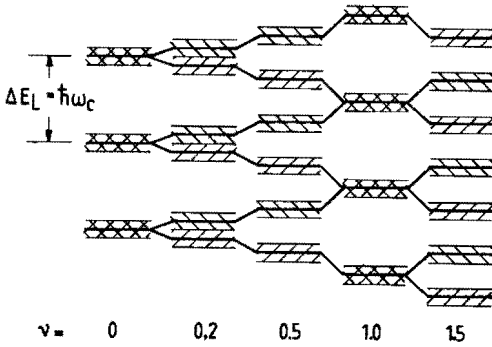


Fig. 2.5 Scheme of spin split Landau levels. The shaded areas represent the broadening of the levels, equal to 0.2 times the Landau splitting. For  $\nu = 0, 0.2$ , and  $1$  the spin levels are (nearly) degenerate and can therefore not be seen separately. For  $\nu = 0.5$  and  $1.5$  the levels are separated far enough, doubling the number of observable levels.

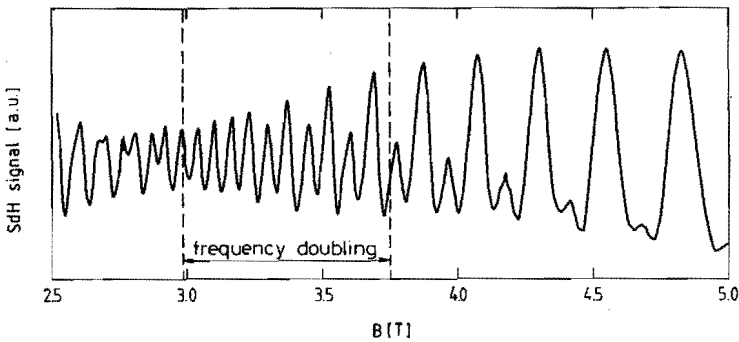


Fig. 2.6 Typical SdH recoder trace in which the second harmonic dominates the first harmonic and the oscillation frequency doubles in a limited field range.

## 2.4 Splitting of the electron spin levels

In this section we discuss briefly the mechanisms which can cause the rapid variation of  $\nu$  with magnetic field, necessary to observe nodes in the SdH amplitude. In the expression for  $\nu$  ( $\nu = g^* (m_c^*/m_o)/2$ ) only the effective  $g$  factor depends on temperature and magnetic field. The electron spin level splitting  $\Delta E_{sp}$  can be considered as the superposition of three contributions: the spin-orbit coupling, the inversion asymmetry and the exchange interaction respectively.

$$\Delta E_{sp} = \Delta E_{sp\ o} + \Delta E_{sp\ ia} + \Delta E_{sp\ ex} \quad (2.9)$$

The spin-orbit contribution is temperature independent and varies linear in  $B$ . Because the Landau splitting  $\Delta E_L$  varies linear in  $B$  as well, the ratio  $\Delta E_{sp\ o}/\Delta E_L$  is constant. Therefore the spin-orbit contribution does not cause nodes in the oscillation amplitude.

The inversion asymmetry contribution varies non-linear with magnetic field, as is demonstrated in chapter 4. This can lead to nodes in the SdH oscillation amplitude under the conditions given in section 2.3. The first observation of nodes in the SdH effect caused by inversion asymmetry effects were reported by Whitsett [17] in 1965. Because the inversion asymmetry is temperature independent, these nodes did not show any temperature dependence.

The contribution due to the exchange interaction is proportional to the average Mn spin component parallel to the magnetic field  $\langle S_B \rangle$ , which strongly varies with temperature and magnetic field. This results in temperature dependent nodes. This temperature dependence of the nodes is very characteristic for SMSC, as first shown by Jaczynski et al. [18].

Because the appearance of the nodes is caused by the splitting of the electron spin levels, one can in reverse use these nodes to study the spin splitting and consequently the bandstructure effects contributing to the spin splitting.

## REFERENCES

- [1] L. Shubnikov, W.J. de Haas, Leiden Comm. 207a, 207c, 207d, 210a (1930).
- [2] L.D. Landau, Z. Phys. 64, 629 (1930).
- [3] R.E. Peierls, Z. Phys. 80, 763 (1933).
- [4] P.N. Argyres, Phys. Rev. 109, 1115 (1958).
- [5] E.N. Adams, T.D. Holstein, J. Phys. Chem. Solids 10, 254 (1959).
- [6] G. Landwehr in Physics of Solids in Intense Magnetic Fields, ed. E. Haidemenakis, (Plenum Press, New York, 1969) p. 145.
- [7] L.M. Roth, P.N. Argyres in Semiconductors and Semimetals, vol. 1, ed. by R.K. Willardson and A.C. Beer, (Academic Press, New York, 1966), p. 159.
- [8] J. Hajdu, G. Landwehr in Strong and Ultrastrong Magnetic Fields, ed. by F. Herlach, (Springer Verlag, Berlin, 1985), p. 17.
- [9] J.J. Neve, Ph.D. thesis, Eindhoven University of Technology, Eindhoven, 1984.
- [10] L. Onsager, Phil. Mag. 43, 1006 (1952).
- [11] I.M. Lifshitz, A.M. Kosevich, Sov. Phys. JETP 2, 636 (1956).
- [12] R.B. Dingle, Proc. Roy. Soc. A211, 517 (1952).
- [13] M.H. Cohen, E.I. Blount, Phil. Mag. 5, 115 (1960).
- [14] L.M. Roth, Phys. Rev. 145, 434 (1966).
- [15] D. Shoenberg, Magnetic Oscillations in Metals, (Cambridge University Press, Cambridge, 1984), p. 487.
- [16] J. Kossut, Sol. St. Comm. 27, 1237 (1978).
- [17] C.R. Whitsett, Phys. Rev. 138, A829 (1965).
- [18] M. Jacyński, J. Kossut, R.R. Gałazka, Phys. Stat. Sol. (b) 88, 73 (1978).

## CHAPTER III BANDMODELS FOR SEMIMAGNETIC SEMICONDUCTORS.

In this chapter we introduce the bandstructure models for  $\text{Hg}_{1-x}\text{Mn}_x\text{Se}$  and  $(\text{Cd}_{1-x}\text{Mn}_x)_3\text{As}_2$ . This chapter is divided in two parts: the first part deals with the bandstructure of  $\text{Hg}_{1-x}\text{Mn}_x\text{Se}$ , the second with the bandstructure of  $(\text{Cd}_{1-x}\text{Mn}_x)_3\text{As}_2$ .

For the interpretation of our results on  $\text{Hg}_{1-x}\text{Mn}_x\text{Se}$  we need a bandmodel which includes the effects of both inversion asymmetry and exchange interaction. Since such a model did not exist, we developed a new model including both effects. Our model combines elements of two old models. The inversion asymmetry aspect is taken from the bandmodel for non-magnetic semiconductors as developed by Weiler et al. [1]. The exchange interaction is treated in the same way as in the modified Pidgeon Brown model [2,3].

We start the first part of this chapter with a short introduction to the bandstructure of non-magnetic narrow-gap and zero-gap semiconductors in general. Then we introduce the model by Weiler et al. After that, we show how we extended this model to SMSC by including the exchange interaction. In the last section of part one we point out the differences between our new model and the modified Pidgeon Brown model.

The bandstructure model for  $(\text{Cd}_{1-x}\text{Mn}_x)_3\text{As}_2$  was developed by Neve et al. [4] and is given in the second part of this chapter. Since this model has very much in common with the model for  $\text{Hg}_{1-x}\text{Mn}_x\text{Se}$ , we only briefly describe the model and point out the differences between the models for  $\text{Hg}_{1-x}\text{Mn}_x\text{Se}$  and  $(\text{Cd}_{1-x}\text{Mn}_x)_3\text{As}_2$ .

### 3.1.1 Bandstructure of a narrow-gap semiconductor

The bandstructure of narrow-gap semiconductors is usually described by a four-band model. This normally ordered bandstructure is illustrated in fig. 3.1a. The  $\Gamma_6$  conduction band, which has the symmetry of atomic s-functions is separated by the energy gap  $E_g$  from the two-fold degenerate  $\Gamma_8$  level. The  $\Gamma_8$  bands are the light hole and the heavy hole bands. The  $\Gamma_7$  level is split off by the spin-orbit inter-

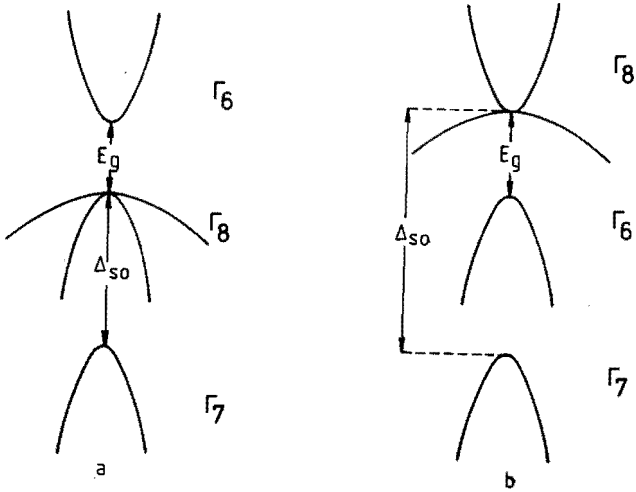


Fig. 3.1 Bandstructure for narrow-gap semiconductors (a) normally ordered, (b) inverted.

action energy  $\Delta_{so}$  from the  $\Gamma_8$  level. The  $\Gamma_7$  and  $\Gamma_8$  levels have the symmetry of atomic p-functions.

Zero-gap semiconductors like HgSe and  $Cd_3As_2$  have the inverted bandstructure (fig. 3.1b). The  $\Gamma_6$  band becomes a valence band and the  $\Gamma_8$  light hole band becomes the conduction band. The energy gap  $E_g$ , defined as  $E(\Gamma_6) - E(\Gamma_8)$ , becomes negative. In the case of low Mn concentrations  $x$ , the SMSC  $Hg_{1-x}Mn_xSe$  and  $(Cd_{1-x}Mn_x)_3As_2$  are zero-gap materials. With increasing Mn concentration  $|E_g|$  decreases, and at a certain value of  $x$ , the bandstructure changes from the inverted to the normal one. The samples used in our experiments are all zero-gap materials.

Calculating the bandstructure of a zero-gap or a narrow-gap semiconductor one has to take into account several aspects:

- i) Due to the small energy gap between the  $\Gamma_6$  and the  $\Gamma_8$  band, the interaction between these bands causes a strong non-parabolicity, as shown by Kane [5]. As a second consequence of the interaction between the bands, the wave functions of the band electrons are mixtures of the  $\Gamma_6$ ,  $\Gamma_7$  and  $\Gamma_8$  states.

- ii) The lack of inversion symmetry of the zinc blende lattice allows k-linear terms in the Hamiltonian.
- iii) Since the  $\Gamma_6$ ,  $\Gamma_7$  and  $\Gamma_8$  energy distances are not small compared to the energy distance to higher bands, the warping of the bands due to the influence of these higher bands has to be taken into account.

### 3.1.2 Bandstructure of a semiconductor with zinc blende symmetry

To calculate the energy levels one has to solve the Schrödinger equation

$$\mathcal{H} \psi(\mathbf{r}) = E \psi(\mathbf{r}) \quad (3.1)$$

The eigenfunctions  $\psi(\mathbf{r})$  are of the form

$$\psi(\mathbf{r}) = \sum_{i=1}^4 f_i(\mathbf{r}) U_i(\mathbf{r}) \quad (3.2)$$

where the summation is over all bands.  $U_i(\mathbf{r})$  is the periodic part of the Bloch function, taken at each band extremum, satisfying eq. 3.1 at the centre of the Brillouin zone. Away from the  $\Gamma$ -point the wave function is a mixture of these so-called basis functions. When the electron spin is taken into account the number of basis functions is doubled. Weiler et al. [1] use the set of basis functions given by

$$\begin{aligned} |U_1\rangle &= |S\uparrow\rangle \\ |U_3\rangle &= -\frac{i}{\sqrt{2}}|(X + iY)\uparrow\rangle \\ |U_5\rangle &= -\frac{i}{\sqrt{6}}|(X + iY)\uparrow + 2Z\downarrow\rangle \\ |U_7\rangle &= -\frac{i}{\sqrt{3}}|(X + iY)\uparrow - Z\downarrow\rangle \\ |U_2\rangle &= |S\downarrow\rangle \\ |U_6\rangle &= -\frac{i}{\sqrt{6}}|(X + iY)\downarrow - 2Z\uparrow\rangle \\ |U_4\rangle &= -\frac{i}{\sqrt{2}}|(X - iY)\downarrow\rangle \\ |U_8\rangle &= -\frac{i}{\sqrt{3}}|(X + iY)\downarrow + Z\uparrow\rangle \end{aligned} \quad (3.3)$$



$|U_1\rangle$  and  $|U_2\rangle$  correspond to the  $\Gamma_6$  states,  $|U_3\rangle$ ,  $|U_5\rangle$ ,  $|U_4\rangle$  and  $|U_6\rangle$  to the  $\Gamma_8$  states and  $|U_7\rangle$  and  $|U_8\rangle$  to the  $\Gamma_7$  states.  $\uparrow$  and  $\downarrow$  are the spin-up and spin-down functions. Due to the actual choice of combinations of functions, the basis functions are not pure spin functions any more.  $|S\rangle$  and  $|X\rangle$ ,  $|Y\rangle$ ,  $|Z\rangle$  are periodic functions which have the symmetry of atomic s and p-functions respectively. To obtain the  $8 \times 8$  Hamiltonian matrix, Weiler et al. used the method of invariants. This method requires the matrix to be invariant under all symmetry operations of the  $T_d$  group, which represents the symmetry of the zinc blende lattice. The allowed matrix elements are obtained using the tables of coupling coefficients for the  $T_d$  group as given by Koster et al. [6]. The matrix includes terms up to second order in  $k$  and to first order in the magnetic field  $B$ . The Hamiltonian matrix thus obtained is a  $8 \times 8$  matrix given by

$$\mathcal{H} = \begin{vmatrix} \mathcal{H}_a & \mathcal{H}_b^\dagger \\ \mathcal{H}_b & \mathcal{H}_c \end{vmatrix} \quad (3.4)$$

The matrices  $\mathcal{H}_a$ ,  $\mathcal{H}_b$  and  $\mathcal{H}_c$  are given in tables 3.1a, b and c respectively.

Table 3.1a.  $k \cdot p$  Hamiltonian matrix for a zinc blende semiconductor.

The basis states are defined in eq. 3.3.

The upper triangle is the Hermitian conjugate of the lower one

	$ 1\rangle$	$ 3\rangle$	$ 5\rangle$	$ 7\rangle$
$\langle 1 $	$E_g + (F + \frac{1}{2}) \frac{(\hbar k)^2}{2m}$ $+ (N_1 + \frac{1}{2}) H_z$			
$\langle 3 $	$\frac{1}{\sqrt{2}} P k_- + \frac{1}{\sqrt{2}} G F_4^+$ $+ \frac{1}{2} N_3 H^+$	$\frac{1}{2} \gamma_1 \frac{(\hbar k)^2}{2m} + \frac{1}{2} \gamma_2 F_3^1$ $\frac{3}{2} (\kappa + \frac{9}{4} q) H_z$		
$\langle 5 $	$\frac{1}{\sqrt{6}} P k_+ + \frac{1}{\sqrt{6}} G F_4^-$ $+ \frac{1}{2} \sqrt{3} N_3 H^-$	$\frac{1}{2} \gamma_2 F_3^2 + i \frac{1}{2} \sqrt{3} \gamma_3 F_4^z$ $+ C k_z$	$\frac{1}{2} \gamma_1 \frac{(\hbar k)^2}{2m} - \frac{1}{2} \gamma_2 F_3^1$ $+ \frac{1}{2} (\kappa + \frac{1}{4} q) H_z$	
$\langle 7 $	$\frac{1}{\sqrt{3}} P' k_+ + \frac{1}{\sqrt{3}} G' F_4^-$	$\frac{1}{\sqrt{2}} \gamma_2 F_3^2 - i \frac{1}{2} \sqrt{6} \gamma_3 F_4^z$ $+ \frac{1}{\sqrt{2}} C' k_z$	$\frac{1}{\sqrt{2}} \gamma_2 F_3^1$	$-A_{so} \frac{1}{2} \gamma_1 \frac{(\hbar k)^2}{2m}$ $+ (\kappa' + \frac{1}{2}) H_z$

Table 3.1b.

	$ 1\rangle$	$ 3\rangle$	$ 5\rangle$	$ 7\rangle$
$\langle 2 $	$(N_1 + \frac{1}{2})H^+$	$N_2 F_3^1 + N_3 H_z$	$-\sqrt{\frac{2}{3}}Pk_z + i\sqrt{\frac{2}{3}}CF_4^z$ $-N_2 F_3^2$	$-\frac{1}{\sqrt{3}}P'k_z + \frac{i}{\sqrt{3}}C'F_4^z$
$\langle 6 $	$-\sqrt{\frac{2}{3}}Pk_z - i\sqrt{\frac{2}{3}}CF_4^z$ $+N_2 F_3^2$	$\frac{1}{2}\sqrt{3}\gamma_3 F_4^+ - \frac{1}{2}Ck_-$ $-\frac{1}{2}\sqrt{3}(\kappa + \frac{7}{4})H^+$	$\frac{1}{2}\sqrt{3}Ck_+$ $-(\kappa + \frac{5}{2})H^-$	$\frac{3}{\sqrt{8}}\gamma_3 F_4^- - \sqrt{\frac{3}{8}}C'k_+$ $+\frac{1}{\sqrt{8}}(\kappa'' + 1)H^-$
$\langle 4 $	$-N_2 F_3^1 + N_3 H_z$	$-\frac{1}{2}\sqrt{3}Ck_+ - \frac{3}{4}qH^-$	$\frac{1}{2}\sqrt{3}\gamma_3 F_4^+ - \frac{1}{2}Ck_-$ $\frac{1}{2}\sqrt{3}(\kappa + \frac{7}{4})H^+$	$-\sqrt{\frac{3}{8}}\gamma_3 F_4^+ - \frac{1}{\sqrt{8}}C'k_-$ $-\frac{\sqrt{3}}{8}(\kappa'' + 1)H^+$
$\langle 8 $	$\frac{1}{\sqrt{3}}P'k_z + \frac{i}{\sqrt{3}}C'F_4^z$	$-\sqrt{\frac{3}{8}}\gamma_3 F_4^+ + \frac{1}{\sqrt{8}}C'k_-$ $+\sqrt{\frac{3}{8}}(\kappa'' + 1)H^+$	$\frac{3}{\sqrt{8}}\gamma_3 F_4^- + \sqrt{\frac{3}{8}}C'k_+$ $\frac{1}{\sqrt{8}}(\kappa'' + 1)H^-$	$-(\kappa' + \frac{1}{2})H^-$

Table 3.1c.

	$ 2\rangle$	$ 6\rangle$	$ 4\rangle$	$ 8\rangle$
$\langle 2 $	$E_g + (F + \frac{1}{2})\frac{(\hbar k)^2}{2m}$ $-(N_1 + \frac{1}{2})H_z$			
$\langle 6 $	$\frac{1}{\sqrt{6}}Pk_- + \frac{1}{\sqrt{6}}CF_4^-$ $\frac{1}{2}\sqrt{3}N_3 H^+$	$\frac{1}{2}\gamma_1 \frac{(\hbar k)^2}{2m} - \frac{1}{2}\gamma_2 F_3^1$ $\frac{1}{2}(\kappa + \frac{1}{4})H_z$		
$\langle 4 $	$\frac{1}{\sqrt{2}}Pk_+ + \frac{1}{\sqrt{2}}C'F_4^-$ $\frac{1}{2}N_3 H^-$	$\frac{1}{2}\gamma_2 F_3^2 + i\frac{1}{2}\sqrt{3}\gamma_3 F_4^z$ $-Ck_z$	$\frac{1}{2}\gamma_1 \frac{(\hbar k)^2}{2m} + \frac{1}{2}\gamma_2 F_3^1$ $+\frac{3}{2}(\kappa + \frac{9}{4})H_z$	
$\langle 8 $	$\frac{1}{\sqrt{3}}P'k_- + \frac{1}{\sqrt{3}}C'F_4^+$	$\frac{1}{\sqrt{2}}\gamma_2 F_3^1$ $\frac{1}{\sqrt{2}}(\kappa'' + 1)H_z$	$\frac{1}{\sqrt{2}}\gamma_2 F_3^2 - i\frac{1}{2}\sqrt{6}\gamma_3 F_4^z$ $+\frac{1}{\sqrt{2}}C'k_z$	$-A_{so} \frac{1}{2}\gamma_1 \frac{(\hbar k)^2}{2m}$ $-(\kappa' + \frac{1}{2})H_z$

In table 3.1 the following abbreviations are used

$$k^2 \equiv k_x^2 + k_y^2 + k_z^2$$

$$k_{\pm} \equiv k_x \pm ik_y$$

$$F_3^1 \equiv (2k_z^2 - k_x^2 - k_y^2) \frac{\hbar^2}{2m}$$

$$F_3^2 \equiv \sqrt{3}(k_x^2 - k_y^2) \frac{\hbar^2}{2m}$$

$$F_4^{\pm} \equiv \{k_z, k_{\pm}\} \frac{\hbar^2}{2m} \equiv (k_z k_{\pm} + k_{\pm} k_z) \frac{\hbar^2}{2m}$$

$$F_4^Z \equiv \{k_x, k_y\} \frac{\hbar^2}{2m}$$

$$H_z \equiv i[k_x, k_y] \frac{\hbar^2}{2m}$$

$$H^{\pm} \equiv \pm[k_{\pm}, k_z] \frac{\hbar^2}{2m}$$

The operator  $k$  is defined as  $k = (p + A)$  where  $p$  is the momentum and  $A$  is the vector potential of the magnetic field.

The most important parameters in this model are the bandgap energy  $E_g$ , the momentum matrix elements  $P$  and  $P'$  and the spin-orbit split off energy  $\Lambda_{so}$ . In the case all other parameters are set equal to zero the bandstructure is isotropic. The anisotropy of the bandstructure is caused by two mechanisms. The first is the warping of the bands and the second is the lack of inversion symmetry in the zinc blende lattice. Both mechanisms are described by the parameters which are listed in table 3.2.

$\gamma_1, \gamma_2, \gamma_3, \kappa$  and  $q$  are the so-called higher band parameters, describing the warping of the  $\Gamma_8$  band due to the influence of higher

Table 3.2: Parameters of the  $k \cdot p$  Hamiltonian among the  $\Gamma_6, \Gamma_7$  and  $\Gamma_8$  band-edge states

$f(\mathbf{k})$	$k_x, k_y, k_z$	$k^2$	$2k_z^2 - k_x^2 - k_y^2$ $\sqrt{3}(k_x^2 - k_y^2)$	$\{k_y, k_z\}$ , $\{k_x, k_z\}$ , $\{k_x, k_y\}$ .	$i[k_y, k_z]$ $i[k_z, k_x]$ $i[k_x, k_y]$
$\langle \Gamma_6   f(\mathbf{k})   \Gamma_6 \rangle$		F			$N_1$
$\langle \Gamma_8   f(\mathbf{k})   \Gamma_8 \rangle$	C	$\gamma_1$	$\gamma_2$	$\gamma_3$	$\kappa, q$
$\langle \Gamma_7   f(\mathbf{k})   \Gamma_7 \rangle$		$\gamma_1'$			$\kappa'$
$\langle \Gamma_6   f(\mathbf{k})   \Gamma_8 \rangle$	P		$N_2$	C	$N_3$
$\langle \Gamma_6   f(\mathbf{k})   \Gamma_7 \rangle$	P'			C'	
$\langle \Gamma_7   f(\mathbf{k})   \Gamma_8 \rangle$	C'		$\gamma_2'$	$\gamma_3'$	$\kappa''$

$\Gamma_8$  bands.  $\gamma_1'$ ,  $\kappa'$  describe the warping of the  $\Gamma_7$  band by higher  $\Gamma_7$  bands.  $\gamma_2'$ ,  $\gamma_3'$ ,  $\kappa''$  do the same for the warping of  $\Gamma_8$  bands by  $\Gamma_7$  bands.  $F$  describes the warping of the  $\Gamma_6$  bands.  $N_1$  and  $q$  contribute to the spin splitting of the  $\Gamma_6$  and  $\Gamma_8$  bands.  $C$  and  $C'$  terms couple  $\Gamma_6$  bands to  $\Gamma_8$  and  $\Gamma_7$  bands respectively.  $C$  and  $C'$  are constants describing interactions linear in  $k$  between  $\Gamma_8$  and  $\Gamma_8$  and  $\Gamma_7$  respectively. The parameters  $C$ ,  $C'$ ,  $G$ ,  $G'$ ,  $N_2$  and  $N_3$  are the inversion asymmetry parameters. In the single group representation the warping parameters and their primed equivalents become equal:  $\gamma_1 = \gamma_1'$ ,  $\gamma_2 = \gamma_2'$ ,  $\gamma_3 = \gamma_3'$  and  $\kappa = \kappa' = \kappa''$ . The same holds for the momentum matrix elements  $P = P'$  and the inversion asymmetry parameters  $C = C'$  and  $G = G'$ .

### 3.1.3 Extension of the bandstructure model to SMSC

So far the model is valid only for non-magnetic semiconductors. In the case of SMSC the exchange interaction between the spins of the mobile electrons and the spins of the localised magnetic atoms has to be taken into account. We include the exchange interaction in the Weiler model analogous to the way in which this interaction was included in the Pidgeon Brown model.

As has been shown by Kossut [7] the exchange Hamiltonian has the form

$$\mathcal{H}_{\text{ex}} = \sum_{\mathbf{R}_i} J(\mathbf{r} - \mathbf{R}_i) \boldsymbol{\sigma} \cdot \mathbf{S}_i \quad (3.5)$$

where  $\boldsymbol{\sigma}$  is the spinoperator of an electron,  $\mathbf{S}_i$  is the total spin operator of the magnetic atom at site  $\mathbf{R}_i$  and  $J$  is the corresponding exchange integral. Because the electron wave function is extended over a large number of lattice sites, we can consider the exchange interaction in terms of the virtual crystal approximation. Now we treat the magnetic atoms, which are randomly substituted at cation sites, as if they substitute a fraction  $x$  of each cation at every cation site. Then we can replace  $J(\mathbf{r} - \mathbf{R}_i)$  by  $x J(\mathbf{r} - \mathbf{R})$  where  $\mathbf{R}$  gives the coordinate of every cation site in the lattice.  $x$  is the fraction of cations of the host lattice replaced by magnetic atoms. This transformation has the advantage that the total Hamiltonian has now again the periodicity of

Table 3.3. Exchange interaction matrix elements

	1⟩	3⟩	5⟩	7⟩	2⟩	6⟩	4⟩	8⟩
⟨1	$\frac{\alpha}{2} \times S_z$	0	0	0	$\frac{\alpha}{2} \times S^-$	0	0	0
⟨3	0	$\frac{\beta}{2} \times S_z$	0	0	0	$\frac{\beta}{2\sqrt{3}} \times S^-$	0	$\frac{\beta}{\sqrt{6}} \times S^-$
⟨5	0	0	$-\frac{\beta}{6} \times S_z$	$\frac{\sqrt{2}}{3} \beta \times S_z$	0	$\frac{\beta}{3} \times S^+$	$\frac{\beta}{2\sqrt{3}} \times S^-$	$-\frac{\beta}{3\sqrt{2}} \times S^+$
⟨7	0	0	$\frac{\sqrt{2}}{3} \beta \times S_z$	$\frac{\beta}{6} \times S_z$	0	$\frac{\beta}{3\sqrt{2}} \times S^+$	$-\frac{\beta}{\sqrt{6}} \times S^-$	$-\frac{\beta}{6} \times S^+$
⟨2	$\frac{\alpha}{2} \times S^+$	0	0	0	$-\frac{\alpha}{2} \times S_z$	0	0	0
⟨6	0	$\frac{\beta}{2\sqrt{3}} \times S^+$	$\frac{\beta}{3} \times S^-$	$\frac{\beta}{3\sqrt{2}} \times S^-$	0	$\frac{\beta}{6} \times S_z$	0	$\frac{\sqrt{2}}{3} \beta \times S_z$
⟨4	0	0	$\frac{\beta}{2\sqrt{3}} \times S^+$	$-\frac{\beta}{\sqrt{6}} \times S^+$	0	0	$-\frac{\beta}{2} \times S_z$	0
⟨8	0	$\frac{\beta}{\sqrt{6}} \times S^+$	$-\frac{\beta}{3\sqrt{2}} \times S^-$	$-\frac{\beta}{6} \times S^-$	0	$\frac{\sqrt{2}}{3} \beta \times S_z$	0	$-\frac{\beta}{6} \times S_z$

the host lattice. The resulting matrix elements are given in table 3.3. The exchange integrals  $\alpha$  and  $\beta$  describe the interaction strength for band electrons with wave functions with s and p-like symmetry respectively. The exchange constants are defined as

$$\begin{aligned}\alpha &= \langle S | J | S \rangle / \Omega_0 \\ \beta &= \langle X | J | X \rangle / \Omega_0\end{aligned}\quad (3.6)$$

where  $\Omega_0$  is the unit cell volume.  $S_x^\pm = S_x \pm iS_y$ , and  $S_z$  yield the components of the spins of the magnetic atoms. Because the electron wave function is very extended the influence of the magnetic atoms can be averaged. This assumption is analogous to the effective field approximation in the theory of magnetism. If a magnetic field is applied parallel to the [001]-axis, the exchange matrix is considerably simplified. In that case  $\langle S^+ \rangle = \langle S^- \rangle = 0$  and the only non-vanishing element is the spin component parallel to the magnetic field  $\langle S_z \rangle$ . For an arbitrary oriented magnetic field a coordinate transformation has to be performed. Also in that case only the spin component parallel to the field remains, and is written as  $\langle S_B \rangle$ .

The spin component parallel to the field is directly related to the magnetisation  $M = -Ng\mu_B \langle S_B \rangle$ .  $\langle S_B \rangle$  can be described by a semi-empirical formula given by Caj et al. [8]

$$\langle S_B \rangle = S_0 B_{5/2} \left[ \frac{5\mu_B B}{k_0 (T + T_0)} \right] \quad (3.7)$$

where  $B_{5/2}$  is the Brillouin function.  $S_0$  and  $T + T_0$  define an adjustable saturation value of the magnetisation and an effective temperature respectively. These adjustable parameters take into account the effects of the mutual interaction of the Mn spins.  $S_0$  and  $T_0$  depend on the temperature and composition  $x$ , and can be obtained from fits of magnetisation measurements. In the absence of a magnetic field  $\langle S_B \rangle$  equals zero. In that case all exchange matrix elements in the Hamiltonian vanish and a SMSC behaves like a normal non-magnetic semiconductor.

### 3.1.4 Bandstructure in a quantising magnetic field

In the presence of a quantising magnetic field the motion of electrons can be considered as a superposition of a free motion parallel to the magnetic field and a circular motion perpendicular to the magnetic field. The energy of the motion parallel to the field is still quasi-continuous. The energy of the circular motion is quantised. We have to perform a coordinate transformation on the Hamiltonian in table 3.1. In the case the field is in the (110)-plane at an angle  $\vartheta$  from the [001]-axis the transformation is given by

$$\begin{aligned} k_x &= 1/\sqrt{2} (ck_1 - k_2 + sk_3) \\ k_y &= 1/\sqrt{2} (ck_1 + k_2 + sk_3) \\ k_z &= -sk_1 + ck_3 \end{aligned} \quad (3.8)$$

where  $s = \sin \vartheta$  and  $c = \cos \vartheta$ .  $k_3$  yields the component of the momentum parallel to the field and is therefore written as  $k_B$ . The matrix elements of the exchange Hamiltonian (table 3.3) also depend on the coordinates and have to be transformed too. However, after averaging, the spin components of the localised moments become scalars and are therefore invariant under coordinate transformation.

After the transformation of the coordinates, we can use the commutation rules

$$\begin{aligned} [k_1, k_2] &= -i/\lambda^2 \\ [k_2, k_B] &= [k_1, k_B] = 0 \end{aligned} \quad (3.9)$$

where  $\lambda = \sqrt{\hbar/eB}$  is the classical cyclotron radius.  $k_1$  and  $k_2$  can be written in terms of raising and lowering operators

$$\begin{aligned} k_1 &= 1/\sqrt{2}\lambda (a+a^\dagger) \\ k_2 &= 1/\sqrt{2}\lambda (a-a^\dagger) \end{aligned} \quad (3.10)$$

$a^\dagger$  and  $a$  are raising and lowering operators for harmonic oscillator functions  $\Phi_n$

$$\begin{aligned} a^\dagger \Phi_n &= \sqrt{n+1} \Phi_{n+1} \\ a \Phi_n &= \sqrt{n} \Phi_{n-1} \end{aligned} \quad (3.11)$$

$N$  is the number operator

$$N\Phi_n = a^\dagger a\Phi_n = n\Phi_n \quad (3.12)$$

The resulting Hamiltonian matrix is a  $8 \times 8$  matrix

$$\mathcal{H} = \begin{vmatrix} \mathcal{H}_a & \mathcal{H}_b^\dagger \\ \mathcal{H}_b & \mathcal{H}_c \end{vmatrix} \quad (3.13)$$

The matrices  $\mathcal{H}_a$ ,  $\mathcal{H}_b$  and  $\mathcal{H}_c$  are given in table 3.4a, b and c respectively. The upper triangle of the matrices  $\mathcal{H}_a$  and  $\mathcal{H}_c$  is the Hermitian conjugate of the lower triangle. In these matrices we used the following abbreviations

$$\begin{aligned} E_p &= p^2 \hbar^2 / 2m \\ \gamma' &= \gamma_3 + (\gamma_2 - \gamma_3) \left[ \frac{3c^2 - 1}{2} \right]^2 \\ \gamma'' &= \frac{1}{3} \gamma_2 + \frac{2}{3} \gamma_3 + \frac{1}{6} (\gamma_2 - \gamma_3) \left[ \frac{3c^2 - 1}{2} \right]^2 \\ \gamma''' &= \frac{2}{3} \gamma_2 + \frac{1}{3} \gamma_3 - \frac{2}{3} (\gamma_2 - \gamma_3) \left[ \frac{3c^2 - 1}{2} \right]^2 \end{aligned}$$



Table 3.4a. Matrix elements of  $\mathcal{H}'_{\alpha}$ 

	$ 1\rangle$	$ 3\rangle$	$ 5\rangle$	$ 7\rangle$
$\langle 1 $	$E_g + 2[F(2N+1) + N_1 + N + 1]\mu_B B$ $+ (F+1/2)\frac{\hbar^2}{m} k_B^2$ $+ \frac{\alpha}{2} \times \langle S_B \rangle$			
$\langle 3 $	$(\mu_B B E_p)^{1/2} a$ $+ i(g_1 + e_1 + f_1)$	$-[(\gamma_1 + \gamma')(2N+1) + 3\kappa]\mu_B B$ $-(\gamma_1 - 2\gamma')\frac{\hbar^2}{2m} k_B^2$ $+ \mu_1 + q_1 + ic_1 + \frac{\beta}{2} \times \langle S_B \rangle$		
$\langle 5 $	$-\left[\frac{\mu_B B E_p}{3}\right]^{1/2} a^\dagger$ $i\sqrt{3}\left(-\frac{1}{3}g_1^\dagger - e_1^\dagger - f_1\right)$	$2\sqrt{3} \mu_B B \gamma''(a^\dagger)^2$ $+ \mu_2 + q_2 + ic_2$	$-[(\gamma_1 - \gamma')(2N+1) - \kappa]\mu_B B$ $-(\gamma_1 + 2\gamma')\frac{\hbar^2}{2m} k_B^2$ $- \mu_1 + q_5 + 3ic_1 - \frac{\beta}{6} \times \langle S_B \rangle$	
$\langle 7 $	$\left[\frac{2\mu_B B E_p}{3}\right]^{1/2} a^\dagger$ $i\sqrt{\frac{2}{3}}g_1^\dagger$	$-2\sqrt{6} \mu_B B \gamma''(a^\dagger)^2$ $-\sqrt{2} \mu_2 + ic_5$	$\sqrt{2}[\gamma'(2N+1) - \kappa - 1]\mu_B B$ $-\sqrt{2} \gamma \frac{\hbar^2}{m} k_B^2$ $-\sqrt{2} \mu_1 + ic_6 - \frac{\sqrt{2}}{3} \beta \times \langle S_B \rangle$	$-A_{SO} - [\gamma_1(2N+1) - 2\kappa - 1]\mu_B B$ $-\gamma \frac{\hbar^2}{2m} k_B^2$ $+ \frac{\beta}{6} \times \langle S_B \rangle$

Table 3.4b. Matrix elements of  $\mathcal{H}_b$ 

	$ 1\rangle$	$ 3\rangle$	$ 5\rangle$	$ 7\rangle$
$\langle 2 $	0	$-i(e_3 - f_3)$	$-\left[\frac{2\mu_B E_p}{3}\right]^{1/2} \lambda_{k_B}$ $-i(g_2 + e_2 - f_2)$	$-\left[\frac{\mu_B E_p}{3}\right]^{1/2} \lambda_{k_B}$ $-\frac{i}{\sqrt{2}} g_2$
$\langle 6 $	$-\left[\frac{2\mu_B E_p}{3}\right]^{1/2} \lambda_{k_B}$ $+i(g_2 + e_2 + f_2)$	$2\sqrt{6} \gamma''' \mu_B B \lambda_{k_B} a^\dagger$ $+ \mu_3 + q_3 + ic_3$	$q_6 + i\sqrt{3} c_3^\dagger$	$6\gamma''' \mu_B B \lambda_{k_B} a$ $+\frac{\sqrt{3}}{2} \mu_3^\dagger + i\sqrt{3} c_7^\dagger$
$\langle 4 $	$i(e_3 + f_3)$	$q_4 + ic_4$	$-2\sqrt{6} \gamma''' \mu_B B \lambda_{k_B} a^\dagger$ $-\mu_3 + q_3 + ic_3$	$-\sqrt{3} \gamma''' \mu_B B \lambda_{k_B} a^\dagger$ $-\frac{1}{\sqrt{2}} \mu_3 - ic_7$
$\langle 8 $	$\left[\frac{\mu_B E_p}{3}\right]^{1/2} \lambda_{k_B}$ $i\frac{1}{\sqrt{2}} g_2$	$2\sqrt{3} \gamma''' \mu_B B \lambda_{k_B} a^\dagger$ $-\frac{1}{\sqrt{2}} \mu_3 + ic_7$	$6\gamma''' \mu_B B \lambda_{k_B} a$ $+\frac{\sqrt{3}}{2} \mu_3^\dagger - i\sqrt{3} c_7^\dagger$	0

Table 3.4c. Matrix elements of  $\mathcal{H}_c$

	$ 2\rangle$	$ 6\rangle$	$ 4\rangle$	$ 8\rangle$
$\langle 2 $	$E_g + 2[F(2N+1) - N_1 + N]\mu_B B$ $+ (F+1/2)\frac{\hbar^2}{m}$ $- \frac{\alpha}{2} \times \langle S_B \rangle$			
$\langle 6 $	$\left[\frac{\mu_B B E_p}{3}\right]^{1/2} a$ $+ i\sqrt{3}\left(\frac{1}{3}g_1 - e_1 - f_1\right)$	$-[(\gamma_1 - \gamma')(2N+1) + \kappa]\mu_B B$ $- (\gamma_1 + 2\gamma')\frac{\hbar^2}{2m} k_B^2$ $- \mu_1 - q_5 - 3ic_1 + \frac{\beta}{6} \times \langle S_B \rangle$		
$\langle 4 $	$-\left[\frac{\mu_B B E_p}{3}\right]^{1/2} a^\dagger$ $- i(g_1^\dagger + e_1^\dagger - f_1)$	$2\sqrt{3} \mu_B B \gamma'' (a^\dagger)^2$ $- \mu_2 - q_2 - ic_2$	$-[(\gamma_1 + \gamma')(2N+1) - 3\kappa]\mu_B B$ $- (\gamma_1 - 2\gamma')\frac{\hbar^2}{2m} k_B^2$ $+ \mu_1 - q_1 - ic_1 - \frac{\beta}{2} \times \langle S_B \rangle$	
$\langle 8 $	$\left[\frac{2\mu_B B E_p}{3}\right]^{1/2} a$ $i\sqrt{\frac{2}{3}} g_1$	$-2[\gamma'(2N+1) + \kappa + 1]\mu_B B$ $+ \sqrt{2} \gamma' \frac{\hbar^2}{m} k_B^2$ $+ \sqrt{2} \mu_1 - ic_6 - \sqrt{\frac{2}{3}} \beta \times \langle S_B \rangle$	$2\sqrt{6} \mu_B B \gamma'' a^2$ $+ \sqrt{2} \mu_2^\dagger - ic_5^\dagger$	$-A_{so} - [\gamma_1(2N+1) + 2\kappa + 1]\mu_B B$ $- \gamma_1 \frac{\hbar^2}{2m} k_B^2$ $- \frac{\beta}{6} \times \langle S_B \rangle$

The warping terms  $q$  and  $\mu$  are given by

$$\begin{aligned}
 q_1 &\equiv -\frac{3}{4} q\mu_B B (3c^4 - 2c^2 + 8) \\
 q_2 &\equiv -\frac{3\sqrt{3}}{4} q\mu_B B s^2(3c^2 - 1) \\
 q_3 &\equiv \frac{3\sqrt{3}}{4} q\mu_B B sc(3c^2 - 1) \\
 q_4 &\equiv -\frac{3}{4} q\mu_B B sc(3c^2 - 5) \\
 q_5 &\equiv \frac{1}{4} q\mu_B B (27c^4 - 18c^2 - 10) \\
 q_6 &\equiv \frac{9}{4} q\mu_B B sc(3c^2 - 1)
 \end{aligned} \tag{3.14}$$

$$\begin{aligned}
 \mu_1 &\equiv -\frac{3}{2} \mu\mu_B B (3c^2 - 1)[s^2(a^2 + a^\dagger)^2 - 2\sqrt{2} sc\lambda k_B(a + a^\dagger)] \\
 \mu_2 &\equiv \frac{1}{2}\sqrt{3} \mu\mu_B B \{[s^2(3c^2 - 1)(2N + 1 - 2\lambda^2 k_B^2) - (c^2 - 3)(3c^2 - 1)a^2 + \\
 &\quad 2\sqrt{2}sc\lambda k_B[(5 - 3c^2)a - (3c^2 - 1)a^\dagger]]\} \\
 \mu_3 &\equiv -\sqrt{3} \mu\mu_B B \{sc[(3c^2 - 1)(2N + 1 - 2\lambda^2 k_B^2) - (5 - 3c^2)a^2 + (3c^2 - 1)a^\dagger]^2 + \\
 &\quad 2\sqrt{2}s^2(3c^2 - 1)\lambda k_B a\}
 \end{aligned} \tag{3.15}$$

where  $\mu = \frac{1}{2} (\gamma_3 - \gamma_2)$ .

The inversion asymmetry terms are given by

$$\begin{aligned}
 c_1 &\equiv \frac{1}{8}\sqrt{6} \frac{C}{\lambda} s(3c^2 - 1)(a - a^\dagger) \\
 c_2 &\equiv \frac{1}{8}\sqrt{2} \frac{C}{\lambda} [5s(3c^2 - 1)a^\dagger - 3s(1 + c^2)a - 2\sqrt{2} c(3c^2 - 1)\lambda k_B] \\
 c_3 &\equiv \frac{1}{8}\sqrt{2} \frac{C}{\lambda} [12s^2ca^\dagger + 2c(3c^2 - 1)a - \sqrt{2} s(3c^2 - 1)\lambda k_B] \\
 c_4 &\equiv \frac{1}{8}\sqrt{6} \frac{C}{\lambda} [2c(3c^2 - 1)a^\dagger + 3\sqrt{2} s(1 + c^2)\lambda k_B] \\
 c_5 &\equiv \frac{1}{4} \frac{C}{\lambda} [s(3c^2 - 1)a^\dagger + 3s(1 + c^2)a - \sqrt{2} c(3c^2 - 1)\lambda k_B] \\
 c_6 &\equiv \frac{1}{4}\sqrt{3} \frac{C}{\lambda} [s(3c^2 - 1)(a + a^\dagger) + 3\sqrt{2} s^2c\lambda k_B] \\
 c_7 &\equiv \frac{1}{4} \frac{C}{\lambda} [3s^2ca^\dagger - c(3c^2 - 1)a - \sqrt{2} s(3c^2 - 1)\lambda k_B]
 \end{aligned} \tag{3.16}$$

$$g_1 \equiv \frac{G\mu_B B}{\sqrt{2}} [-s(3c^2-1)(2N+1-2\lambda^2 k_B^2 + a^2) - 3s(1+c^2)a^{\dagger 2} - 6\sqrt{2} s^2 c \lambda k_B a + 2\sqrt{2} c(3c^2-1)\lambda k_B a^{\dagger}] \quad (3.17)$$

$$g_2 \equiv \frac{2G\mu_B B}{\sqrt{2}} [3s^2 c(2N+1-2\lambda^2 k_B^2) - c(3c^2-1)(a^2 + a^{\dagger 2}) - 2\sqrt{2} s(3c^2-1)\lambda k_B (a + a^{\dagger})]$$

$$e_1 \equiv \frac{1}{2} N_2 \mu_B B [-s(3c^2-1)(2N+1-2\lambda^2 k_B^2 + 3a^2) + 3s(1+c^2)a^{\dagger 2} - 12\sqrt{2} s^2 c \lambda k_B a]$$

$$e_2 \equiv -\sqrt{3} N_2 \mu_B B [c(3c^2-1)(a^2 - a^{\dagger 2}) + \sqrt{2} s(3c^2-1)\lambda k_B (a - a^{\dagger})] \quad (3.18)$$

$$e_3 \equiv -N_2 \mu_B B [c(3c^2-1)(2N+1-2\lambda^2 k_B^2) - 6s^2 c a^{\dagger 2} + 3\sqrt{2} s(1+c^2)\lambda k_B a + 3\sqrt{2} s(3c^2-1)\lambda k_B a^{\dagger}]$$

$$f_1 \equiv N_3 \mu_B B s(3c^2-1)$$

$$f_2 \equiv -3\sqrt{3} N_3 \mu_B B s^2 c \quad (3.19)$$

$$f_3 \equiv -N_3 \mu_B B c(3c^2-1)$$

The eigenvectors of the matrix can now be written in terms of harmonic oscillator functions

$$|U(n)\rangle = \begin{bmatrix} a_1^n \Phi_n \\ a_3^n \Phi_{n-1} \\ a_5^n \Phi_{n+1} \\ a_7^n \Phi_{n+1} \\ a_2^n \Phi_n \\ a_6^n \Phi_{n-1} \\ a_4^n \Phi_{n+1} \\ a_8^n \Phi_{n-1} \end{bmatrix} + \sum_{\substack{l=-\infty \\ l \neq 0}}^{\infty} \begin{bmatrix} a_1^{n+l} \Phi_{n+l} \\ a_3^{n+l} \Phi_{n-1+l} \\ a_5^{n+l} \Phi_{n+1+l} \\ a_7^{n+l} \Phi_{n+1+l} \\ a_2^{n+l} \Phi_{n+l} \\ a_6^{n+l} \Phi_{n-1+l} \\ a_4^{n+l} \Phi_{n+1+l} \\ a_8^{n+l} \Phi_{n-1+l} \end{bmatrix} \quad (3.20)$$

The series expansion of the eigenvector is necessary because of the presence of the warping terms  $q$  and  $\mu$  and the inversion asymmetry terms  $c$ ,  $e$ ,  $f$  and  $g$ . These terms contain raising and lowering operators up to second order, thus coupling oscillator functions of index  $n$  with those with indices  $n-3$ ,  $n-2$ ,  $n-1$ ,  $n+1$ ,  $n+2$  and  $n+3$ . Therefore each eigenfunction becomes an infinite series of harmonic oscillator functions. Substitution of an eigenfunction of this kind in eq. 3.1 results in a Hamiltonian matrix of infinite size.

To each Landau number  $n$  belong eight energy eigenvalues: two for each of the four bands. One of the two energies corresponds to the spin-up level and one to the spin-down level.

The numerical method to obtain the eigenvalues is discussed in the next chapter.

### 3.1.5 *Modified Pidgeon Brown model*

The modified Pidgeon Brown model [2] is the extension to SMSC of the bandstructure model for narrow-gap semiconductors in magnetic fields as given by Pidgeon and Brown [3]. The exchange interaction is incorporated in the Hamiltonian in the same way as we incorporated this interaction in the Hamiltonian matrix by Weiler et al.

The modified Pidgeon Brown model treats the bandstructure in principle in the same way as our new model. The first difference is that all terms proportional to  $k_B$  are neglected. The second and most important difference is that the Pidgeon Brown model neglects all inversion asymmetry terms and most of the warping terms. The neglect of these terms removes the coupling between adjacent Landau levels. The eigenfunctions are no longer infinite series of coupled harmonic oscillator functions, but can be written as

$$|U(n)\rangle = \begin{bmatrix} a_1 & \Phi_n \\ a_3 & \Phi_{n-1} \\ a_5 & \Phi_{n+1} \\ a_7 & \Phi_{n+1} \\ a_2 & \Phi_n \\ a_6 & \Phi_{n-1} \\ a_4 & \Phi_{n+1} \\ a_8 & \Phi_{n-1} \end{bmatrix} \quad (3.21)$$

The Hamiltonian is considerably simplified and can be written as an 8x8 matrix H

$$H = \begin{vmatrix} H_a & 0 \\ 0 & H_b \end{vmatrix} \quad (3.22)$$

where  $H_a$  and  $H_b$  are 4x4 matrices given by eqs. 3.23 and 3.24 respectively.

In the case we put  $k_B$  and all warping and inversion asymmetry parameters equal to zero in our model, the remaining matrix elements in our Hamiltonian differ slightly from those in eqs. 3.23 and 3.24, because our set of basis functions differs from the set used by Pidgeon and Brown. However, the eigenenergies of the Pidgeon Brown Hamiltonian and our new Hamiltonian are the same in that case.

Comparing the size of the matrices of eqs. 3.23 and 3.24 to the infinite size of the Hamiltonian including the inversion asymmetry, it is clear that it is preferable to use the Pidgeon Brown Hamiltonian for the numerical calculation of the energy eigenvalues in the case the inversion asymmetry can be neglected.

	$ 1\rangle$	$ 3\rangle$	$ 5\rangle$	$ 7\rangle$
$\langle 1 $	$E_g + 2[F(2N+1) + N+1]\mu_B B$ $+ \frac{\alpha}{2} \times \langle S_B \rangle$			
$\langle 3 $	$-i(\mu_B B E_p)^{1/2} a$	$-[(\gamma_1 + \gamma')(2N+1) + 3\kappa]\mu_B B$ $+ \frac{\beta}{2} \times \langle S_B \rangle$		
$\langle 5 $	$-i \left[ \frac{\mu_B B E_p}{3} \right]^{1/2} a^\dagger$	$-2\sqrt{3} \mu_B B \gamma'' (a^\dagger)^2$	$-[(\gamma_1 - \gamma')(2N+1) - \kappa]\mu_B B$ $- \frac{\beta}{6} \times \langle S_B \rangle$	
$\langle 7 $	$\left[ \frac{2\mu_B B E_p}{3} \right]^{1/2} a^\dagger$	$i\sqrt{6} \mu_B B \gamma' (a^\dagger)^2$	$-i\sqrt{2}[\gamma'(2N+1) - \kappa]\mu_B B$ $- \frac{\sqrt{2}}{3} \beta \times \langle S_B \rangle$	$-A_{so} - [\gamma_1(2N+1) - 2\kappa]\mu_B B$ $+ \frac{\beta}{6} \times \langle S_B \rangle$

(3.23)

The upper triangle is the Hermitian conjugate of the lower one.



	$ 2\rangle$	$ 6\rangle$	$ 4\rangle$	$ 8\rangle$
$\langle 2 $	$E_g + 2[F(2N+1) - N]\mu_B B$ $-\frac{\alpha}{2} x \langle S_B \rangle$			
$\langle 6 $	$-i \left[ \frac{\mu_B B E_p}{3} \right]^{1/2} a$	$-[(\gamma_1 - \gamma')(2N+1) + \kappa]\mu_B B$ $+\frac{\beta}{6} x \langle S_B \rangle$		
$\langle 4 $	$-i(\mu_B B E_p)^{1/2} a^\dagger$	$-\sqrt{3} \mu_B B \gamma'' (a^\dagger)^2$	$-[(\gamma_1 + \gamma')(2N+1) - 3\kappa]\mu_B B$ $-\frac{\beta}{2} x \langle S_B \rangle$	
$\langle 8 $	$\left[ \frac{2\mu_B B E_p}{3} \right]^{1/2} a$	$-i\sqrt{2}[\gamma'(2N+1) + \kappa]\mu_B B$ $-i\frac{\sqrt{2}}{3} \beta x \langle S_B \rangle$	$-i2\sqrt{6} \mu_B B \gamma' a^2$	$-\Lambda_{so} - [\gamma_1(2N+1) + 2\kappa]\mu_B B$ $-\frac{\beta}{6} x \langle S_B \rangle$

(3.24)

The upper triangle is the Hermitian conjugate of the lower one.

### 3.2 Bandstructure of a semiconductor with tetragonal symmetry

The crystal structure of  $(\text{Cd}_{1-x}\text{Mn}_x)_3\text{As}_2$  is rather complicated. However, it may be approximated by a cubic structure with an additional tetragonal distortion. Bodnar [9] developed a bandstructure model for the host lattice  $\text{Cd}_3\text{As}_2$  based on this assumption. In this model all inversion asymmetry terms and all warping terms are neglected. However, the bandstructure is still highly anisotropic, due to the tetragonal distortion of the lattice. The lower symmetry of the lattice due to this distortion lifts the degeneracy of the  $\Gamma_8$  bands for  $k = 0$ . The splitting of the  $\Gamma_8$  bands is characterised by the crystal field splitting parameter  $\delta$ .

Due to the tetragonal distortion  $|Z\rangle$  is no longer equivalent to  $|X\rangle$  and  $|Y\rangle$ . Therefore two different momentum matrix elements are defined:  $P_{//}$  and  $P_{\perp}$ . In principle the spin-orbit splitting parameter  $\Delta_{\text{so}}$  is also anisotropic, but this anisotropy has been neglected since there exist no experimental data to justify such a refinement.

Neve et al. [4] extended this model to SMSC by including the exchange interaction. Due to the lower symmetry of the crystal also the exchange parameter  $\beta$  becomes anisotropic

$$\begin{aligned}\beta_{//} &\equiv \langle Z|J|Z\rangle/\Omega_0 \\ \beta_{\perp} &\equiv \langle X|J|Z\rangle/\Omega_0 = \langle Y|J|Y\rangle/\Omega_0\end{aligned}\quad (3.25)$$

The set of basis functions used by Neve et al. [4] differs from the set given in eq. 3.3.

$$\begin{aligned}|U_1\rangle &= |iS\downarrow\rangle \\ |U_2\rangle &= |iS\uparrow\rangle \\ |U_3\rangle &= |1/\sqrt{2} (X-iY)\downarrow\rangle \\ |U_4\rangle &= |1/\sqrt{6} (X-iY)\uparrow + 2/\sqrt{6} Z\downarrow\rangle \\ |U_5\rangle &= |-1/\sqrt{6} (X+iY)\downarrow + 2/\sqrt{6} Z\uparrow\rangle \\ |U_6\rangle &= |1/\sqrt{2} (X+iY)\uparrow\rangle \\ |U_7\rangle &= |-1/\sqrt{3} (X-iY)\uparrow + 1/\sqrt{3} Z\downarrow\rangle \\ |U_8\rangle &= |1/\sqrt{2} (X-iY)\downarrow + 1/\sqrt{3} Z\uparrow\rangle\end{aligned}\quad (3.26)$$

The resulting matrix elements are given in table 3.5, where

$$\begin{aligned}
 a &= 1/2 \alpha \times \langle S_z \rangle & a^\pm &= 1/2 \alpha \times \langle S_z^\pm \rangle \\
 b &= 1/2 \beta_\perp \times \langle S_z \rangle & c^\pm &= 1/2 \beta_\perp \times \langle S_z^\pm \rangle \\
 b &= 1/2 \beta_\parallel \times \langle S_z \rangle & d^\pm &= 1/2 \beta_\parallel \times \langle S_z^\pm \rangle
 \end{aligned}
 \tag{3.27}$$

To obtain the Hamiltonian matrix for an arbitrary oriented magnetic field, the coordinate transformation given in eq. 3.8 has to be performed.

Due to the tetragonal lattice distortion the expressions for  $k$  in terms of raising and lowering operators become more complicated than those in eq. 3.10. Therefore terms quadratic in the raising and lowering operators occur in the Hamiltonian. However, the terms of higher order do not contribute significantly to the energy eigenvalues of the conduction band and can therefore be neglected [4]. Then it is possible to derive a determinantal equation of eighth degree and solve this numerically to obtain the energy eigenvalues.

#### REFERENCES

- [1] M.H. Weiler, R.L. Aggarwal, B. Lax, Phys. Rev. B17, 3269 (1978).
- [2] M. Jaczynski, J. Kossut, R.R. Gałazka, Phys. Stat. Sol. (b) 88, 73 (1978).
- [3] C.R. Pidgeon, R.N. Brown, Phys. Rev. 146, 575 (1966).
- [4] J.J. Neve, J. Kossut, C.M. van Es, F.A.P. Blom, J. Phys. C: Solid State Phys. 15, 4795 (1982).
- [5] E.O. Kane, J. Phys. Chem. Solids 1, 249 (1957).
- [6] G.F. Koster, J.O. Dimmock, R.C. Wheeler, H. Statz, Properties of the thirty two point groups (MIT, Cambridge, 1966).
- [7] J. Kossut, Phys. Stat. Sol. (b) 78, 537 (1976).
- [8] J.A. Caj, R. Planel, G. Fishman, Sol. St. Comm. 29, 435 (1979).
- [9] J. Bodnar, Proc. Int. Conf. Phys. Narrow Gap Semicond., Warsaw 1977 (Polish Scient. Publ., Warsaw, 1978) p. 311.

Table 3.5 Matrix elements of the Hamiltonian for a tetragonally distorted lattice

	$ 1\rangle$	$ 2\rangle$	$ 3\rangle$	$ 4\rangle$	$ 5\rangle$	$ 6\rangle$	$ 7\rangle$	$ 8\rangle$
$\langle 1 $	$E_g - a$	$a^+$	$P_{\perp} k_-$	$\sqrt{\frac{2}{3}} P_{//} k_z$	$-\sqrt{\frac{1}{3}} P_{\perp} k_+$	0	$\sqrt{\frac{1}{3}} P_{//} k_z$	$\sqrt{\frac{2}{3}} P_{\perp} k_+$
$\langle 2 $	$a^-$	$E_g + a$	0	$\sqrt{\frac{1}{3}} P_{\perp} k_-$	$\sqrt{\frac{2}{3}} P_{//} k_z$	$P_{\perp} k_+$	$-\sqrt{\frac{2}{3}} P_{\perp} k_-$	$\sqrt{\frac{1}{3}} P_{//} k_z$
$\langle 3 $	$P_{\perp} k_+$	0	$-b$	$\sqrt{\frac{1}{3}} d^+$	0	0	$-\sqrt{\frac{2}{3}} d^+$	0
$\langle 4 $	$\sqrt{\frac{2}{3}} P_{//} k_z$	$\sqrt{\frac{1}{3}} P_{\perp} k_+$	$\sqrt{\frac{1}{3}} d^-$	$-\frac{1}{3}(2\delta + 2b' - b)$	$\frac{2}{3} c^+$	0	$-\frac{\sqrt{2}}{3}(\delta + b' + b)$	$\frac{\sqrt{2}}{3} c^+$
$\langle 5 $	$-\sqrt{\frac{1}{3}} P_{\perp} k_-$	$\sqrt{\frac{2}{3}} P_{//} k_z$	0	$\frac{2}{3} c^-$	$-\frac{1}{3}(2\delta + b - 2b')$	$-\sqrt{\frac{1}{3}} d^+$	$\frac{\sqrt{2}}{3} c^-$	$\frac{\sqrt{2}}{3}(b + b' - \delta)$
$\langle 6 $	0	$P_{\perp} k_-$	0	0	$-\sqrt{\frac{1}{3}} d^-$	$b$	0	$\sqrt{\frac{2}{3}} d^-$
$\langle 7 $	$\sqrt{\frac{1}{3}} P_{//} k_z$	$-\sqrt{\frac{2}{3}} P_{\perp} k_+$	$-\sqrt{\frac{2}{3}} d^-$	$-\frac{\sqrt{2}}{3}(\delta + b + b')$	$\frac{\sqrt{2}}{3} c^+$	0	$-\Delta_{so} - \frac{1}{3}(\delta + b' - 2b)$	$\frac{1}{3} c^+$
$\langle 8 $	$\sqrt{\frac{2}{3}} P_{\perp} k_-$	$\sqrt{\frac{1}{3}} P_{//} k_z$	0	$\frac{2}{3} c^-$	$\frac{\sqrt{2}}{3}(b + b' - \delta)$	$\sqrt{\frac{2}{3}} d^+$	$\frac{1}{3} c^-$	$\Delta_{so} - \frac{1}{3}(\delta + 2b - b')$

CHAPTER IV NUMERICAL CALCULATION OF THE ELECTRON ENERGY LEVELS

IN  $\text{Hg}_{1-x}\text{Mn}_x\text{Se}$ .

In this chapter we discuss how the energy eigenvalues can be obtained from the Hamiltonian of our new bandmodel. The results of the calculations illustrate some effects of the inversion asymmetry on the bandstructure in the presence of a magnetic field.

4.1 Numerical algorithm

In the previous chapter we have shown that the Hamiltonian matrix of our new model becomes of infinite size due to the coupling between the Landau levels. Numerically we can treat only finite matrices. Therefore the matrix has to be truncated: each eigenfunction corresponding to Landau level  $n$  is constructed from only  $2j+1$  oscillator functions. Eq. 3.20 then becomes

$$|U(n)\rangle = \begin{bmatrix} a_1^n \phi_n \\ a_3^n \phi_{n-1} \\ a_5^n \phi_{n+1} \\ a_7^n \phi_{n+1} \\ a_2^n \phi_n \\ a_6^n \phi_{n-1} \\ a_4^n \phi_{n+1} \\ a_8^n \phi_{n-1} \end{bmatrix} + \sum_{\substack{l = -j \\ l \neq 0}}^j \begin{bmatrix} a_1^{n+l} \phi_{n+l} \\ a_3^{n+l} \phi_{n+1+l} \\ a_5^{n+l} \phi_{n+1+l} \\ a_7^{n+l} \phi_{n+1+l} \\ a_2^{n+l} \phi_{n+l} \\ a_6^{n+l} \phi_{n-1+l} \\ a_4^{n+l} \phi_{n+1+l} \\ a_8^{n+l} \phi_{n-1+l} \end{bmatrix} \quad (4.1)$$

Doing this, the influence of oscillator functions with index higher than  $n+j$  and lower than  $n-j$  is neglected. This is allowed, since the coupling between the central oscillator function with index  $n$  and the other oscillator functions gradually decreases with increasing value of  $l$ . A good approximation of the eigenenergies for Landau level  $n$  can be obtained by choosing  $j$  large enough.

Table 4.1.  
Bandparameters for HgSe [2]

$E_g$	= -0.274 eV
$P$	= $7.2 \cdot 10^{-10}$ eVm
$\Delta_{so}$	= 0.39 eV
$\gamma_1$	= 5.77
$\gamma_2$	= -1.17
$\gamma_3$	= -0.57
$\kappa$	= 0.98
$F$	= 0

To determine the actual choice of  $j$ , we tested the accuracy of the energy eigenvalues obtained from our truncated matrix. For this test we used the set of bandparameters for HgSe in table 4.1. For the Fermi energy and the inversion asymmetry we used values, typical for the samples in our experiments:  $E_F = 100$  meV and  $C = 3.0 \cdot 10^{-11}$  eVm. The magnetic field was varied from 0.5 T to 2.5 T, corresponding to the field range in which the data were taken in the experiments.

Since we are only interested in the energy levels close to the Fermi energy, we choose the Landau number  $n$  of the central level of the truncated matrix in such a way that the corresponding energy level is as close as possible to the Fermi energy. Then we increase  $j$  until the energies corresponding to the five central levels change less than 0.1 percent. To fulfil this convergency criterion over the magnetic field range from 0.5 to 2.5 T, we have to take into account eleven Landau levels (i.e.  $j = 5$ ).

The choice of  $j$  equal to 5 implies that the 8 eigenfunctions for the Landau level  $n$  are constructed from  $8 \times (2j+1) = 88$  eigenfunctions. To obtain the energy eigenvalues we have to solve an  $88 \times 88$  matrix. Our numerical procedure yields the 88 eigenvalues simply in ascending order without referring to either Landau number or spin direction.

The identification of these eigenenergies can be difficult in the case the spin splitting exceeds the Landau splitting. In that case the spin-up and spin-down level belonging to the same Landau number are no longer adjacent. This large splitting can arise due to effects of the exchange interaction or the inversion asymmetry. The method to identify the energy levels is illustrated in fig. 4.1 for the case the spin splitting is caused by the exchange interaction. Without exchange interaction or inversion asymmetry the spin splitting is less than half the Landau splitting. In that case the levels can easily be identified with the corresponding Landau number and spin direction (left part of fig. 4.1 where  $\alpha = \beta = 0$ ). During a gradual increase of  $\alpha$  the levels shift and even cross each other. When  $\alpha$  has reached its final value of  $-0.8$  eV (middle part of fig. 4.1) we start increasing  $\beta$ . In the right part of fig. 4.1,  $\beta$  reaches  $1.3$  eV. Although we have a spin splitting 2.5 times as large as the Landau splitting, the levels can still be identified by tracing back their origin.

Problems in the identification of the levels due to level crossing caused by a large inversion asymmetry splitting can be solved in a similar way.

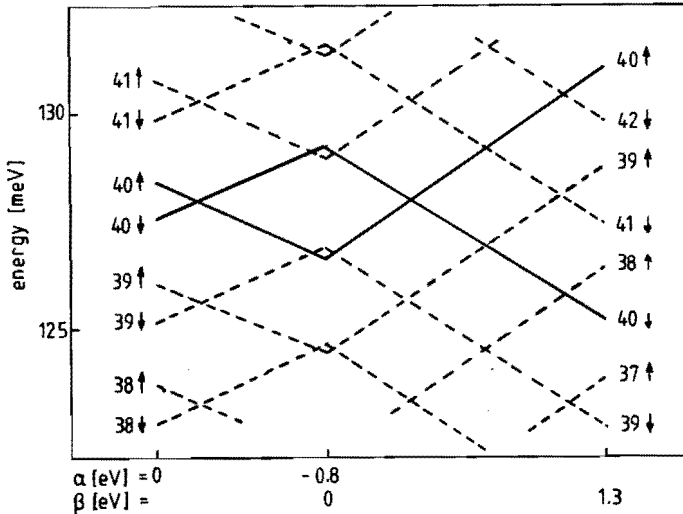


Fig. 4.1 Identification of spin split Landau levels, calculated for  $\text{Hg}_{0.975}\text{Mn}_{0.025}\text{Se}$  for  $B = 0.85$  T,  $\parallel [110]$  at 2.03 K. The levels are calculated as a function of the exchange interaction parameters. The inversion asymmetry parameters are equal to zero. Further explanation is given in the text.

#### 4.2 Inversion asymmetry effects on the bandstructure

Using the algorithm outlined above, our model allows for the first time to calculate the effects of the inversion asymmetry on the bandstructure of a narrow-gap semiconductor. We illustrate some of these effects with calculations using parameters typical for the materials in our experiments. For clarity the exchange interaction is neglected in these calculations by putting  $\alpha$  and  $\beta$  equal to zero.

First we calculate the orientation dependence of the spin splitting. The anisotropy of the spin splitting changes its shape due to the inversion asymmetry. The spin splitting without inversion asymmetry is

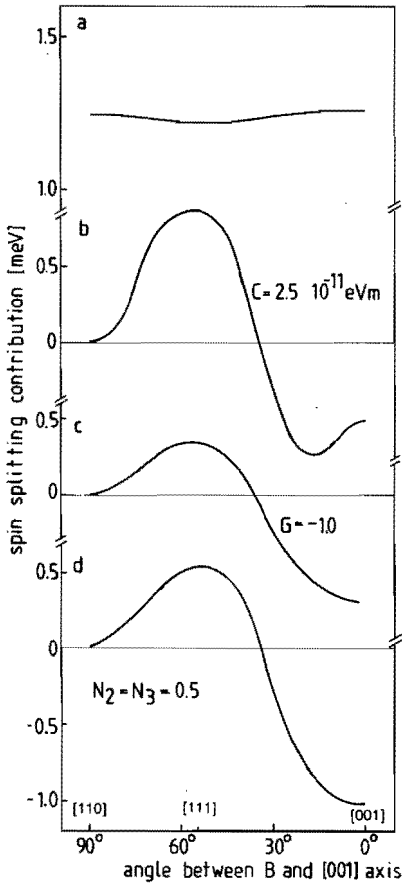


Fig. 4.2

Anisotropy of the spin splitting of the conduction band, calculated for HgSe. The splitting is decomposed in two parts. (a) splitting without inversion asymmetry. (b), (c) and (d) inversion asymmetry contribution to the splitting due to parameters  $C$ ,  $G$  and  $N_2=N_3$  respectively. The splitting is calculated for a Fermi energy of 80 meV.



shown in fig. 4.2a. This splitting is only slightly anisotropic. The part of the spin splitting arising from the inversion asymmetry is shown in fig. 4.2b, c and d. For each curve only one of the inversion asymmetry parameters differs from zero. Following Weiler et al. [1] we assume  $N_2$  equal to  $N_3$ . The splittings are calculated for  $B = 1$  T and  $E_F = 80$  meV, and the set of bandparameters for HgSe in table 4.1. From fig. 4.2 it is clear that all inversion asymmetry parameters cause a similar angular dependence of the splitting. For  $B \parallel [110]$  there is no inversion asymmetry contribution to the spin splitting.

Next we calculate the field dependence of the inversion asymmetry contribution to the spin splitting. The magnetic field is oriented parallel to the [001]-axis. For these calculations we use the parameters for  $\text{Hg}_{0.975}\text{Mn}_{0.025}\text{Se}$ , which we have taken equal to the HgSe parameters except the bandgap energy  $E_g = -165$  meV. The Fermi energy equals 130 meV. The results of the field dependence of the inversion asymmetry contribution to the spin splitting are given in table 4.2. for  $C = 1.0 \cdot 10^{-11}$  eVm,  $G = -1.0$  and  $N_2 = N_3 = 0.5$ . All energies are given in meV.  $\Delta E_{sp}$  is the total spin splitting.  $\Delta E_{sp o}$  is the spin splitting without inversion asymmetry.  $\Delta E_{sp ia}$  is the change of the spin splitting due to the inversion asymmetry. The last column lists the ratio of spin splittings with and without inversion asymmetry. From this table we conclude that the inversion asymmetry contribution to the spin splitting decreases with increasing magnetic field.

The influence of the inversion asymmetry on the spin splitting also depends on the Fermi energy. To calculate the energy dependence we used the same parameters as we used to check the field dependence. The field is 1.5 T and the Fermi energies are 130 meV and 110 meV. The results are given in table 4.3. The headings of the columns have the same meaning as in table 4.2.  $\theta$  denotes the angle between the magnetic field and the [001]-axis, with the magnetic field in the (110)-plane. We conclude that the inversion asymmetry contribution to the spin splitting decreases with decreasing Fermi energy.

REFERENCES

- [1] M.H. Weiler, R.L. Aggarwal, B. Lax, Phys. Rev. B17, 3269 (1978)  
 [2] R.R. Gałazka, W. Dobrowolski, J.C. Thuillier, Phys. Stat. Sol. (b) 98, 97 (1980)

Table 4.2 Magnetic field dependence of the inversion asymmetry part of the spin splitting. All energies are given in meV. the magnetic field is oriented parallel to the [001] axis. The Fermi energy is 130 meV.

$$C = 1 \cdot 10^{-11} \text{ eVm}$$

B[T]	$\Delta E_{sp}$ [meV]	$\Delta E_{sp o}$	$\Delta E_{sp ia}$	$\Delta E_{sp ia} / \Delta E_{sp o}$
0.5	-0.14	0.57	-0.71	1.25
1.0	0.63	1.06	-0.43	0.41
1.5	1.25	1.55	-0.30	0.19
2.0	1.82	2.05	-0.22	0.10

$$C = -1.0$$

B[T]	$\Delta E_{sp}$	$\Delta E_{sp o}$	$\Delta E_{sp ia}$	$\Delta E_{sp ia} / \Delta E_{sp o}$
0.5	-0.92	0.57	-1.48	2.60
1.0	0.02	1.06	-1.04	0.98
1.5	0.78	1.55	-0.77	0.51
2.0	1.45	2.05	-0.60	0.29

$$N_2 = N_3 = 0.5$$

B[T]	$\Delta E_{sp}$	$\Delta E_{sp o}$	$\Delta E_{sp ia}$	$\Delta E_{sp ia} / \Delta E_{sp o}$
0.5	-1.79	0.57	-2.36	4.14
1.0	-0.95	1.06	-2.01	1.89
1.5	0.01	1.55	-1.54	0.99
2.0	0.84	2.05	-1.29	0.63

Table 4.3. Energy dependence of the inversion asymmetry part of the spin splitting, for different orientations of the magnetic field. All energies are given in meV.

$$E_F = 130 \text{ meV}$$

$\theta$	$\Delta E_{sp o}$	$C = 2 \cdot 10^{-11} \text{ eVm}$		$G = -1.0$		$N_2 = N_3 = 0.5$	
		$\Delta E_{sp}$	$\Delta E_{sp ia}$	$\Delta E_{sp}$	$\Delta E_{sp ia}$	$\Delta E_{sp}$	$\Delta E_{sp ia}$
0	1.55	0.52	-1.03	0.70	-0.78	0.01	-1.54
15	1.54	0.84	-0.76	0.99	-0.56	0.36	-1.19
30	1.53	1.48	-0.06	1.41	-0.12	1.32	-0.21
45	1.52	2.12	0.60	1.89	0.37	2.35	0.83
60	1.52	2.23	0.71	1.97	0.46	2.53	1.01
75	1.53	1.83	0.30	1.71	0.18	1.93	0.40
90	1.54	1.54	0.00	1.54	0.00	1.54	0.00

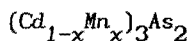
$$E_F = 110 \text{ meV}$$

$\theta$	$\Delta E_{sp o}$	$C = 2 \cdot 10^{-11} \text{ eVm}$		$G = -1.0$		$N_2 = N_3 = 0.5$	
		$\Delta E_{sp}$	$\Delta E_{sp ia}$	$\Delta E_{sp}$	$\Delta E_{sp ia}$	$\Delta E_{sp}$	$\Delta E_{sp ia}$
0	1.79	0.98	-0.82	1.27	-0.52	0.84	-0.95
15	1.78	1.21	-0.58	1.39	-0.40	1.06	-0.73
30	1.77	1.72	-0.06	1.69	-0.08	1.64	-0.13
45	1.76	2.21	0.45	1.99	0.23	2.24	0.48
60	1.76	2.29	0.53	2.04	0.28	2.34	0.58
75	1.77	1.99	0.22	1.88	0.11	1.98	0.21
90	1.78	1.78	0.00	1.78	0.00	1.78	0.00

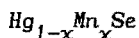
## CHAPTER V SAMPLE PREPARATION.

In this chapter the preparation of the samples is described: crystal growth, orientation and composition checks, annealing procedures and attachment of current and voltage leads. This chapter mainly deals with the materials  $(\text{Cd}_{1-x}\text{Mn}_x)_3\text{As}_2$  and  $\text{Hg}_{1-x}\text{Mn}_x\text{Se}$ . In the sections on crystal growth and composition analysis also our efforts to grow new semimagnetic materials are discussed.

### 5.1 Crystal growth



All samples used in the experiments were grown by the Bridgman method. The  $(\text{Cd}_{1-x}\text{Mn}_x)_3\text{As}_2$  samples were grown in the group Semiconductor Physics of the Physics Department at our University. To grow the  $(\text{Cd}_{1-x}\text{Mn}_x)_3\text{As}_2$  crystals stoichiometric amounts of the pure elements were sealed in a quartz ampoule which was evacuated to  $10^{-5}$  mbar. The ampoule was heated up to  $750^\circ\text{C}$ , which is above the melting point of  $\text{Cd}_3\text{As}_2$  ( $721^\circ\text{C}$  [1]). To ensure a thorough mixing, the temperature was kept at  $750^\circ\text{C}$  for several days and in some cases the ampoule was vibrated. Then the actual crystal growth started, by moving the ampoule in a temperature gradient, as shown in fig. 5.1. The velocity of the ampoule was typically 1 mm per hour. In this way good single crystals of  $(\text{Cd}_{1-x}\text{Mn}_x)_3\text{As}_2$  could be obtained.



The  $\text{Hg}_{1-x}\text{Mn}_x\text{Se}$  samples were grown in the Institute of Physics of the Polish Academy of Sciences in Warsaw. The method to grow these crystals [2] was basically the same as for  $(\text{Cd}_{1-x}\text{Mn}_x)_3\text{As}_2$ . The elements were heated above the melting point of  $\text{HgSe}$  ( $799^\circ\text{C}$  [3]).

#### New materials

Several attempts were made to grow other semimagnetic compounds of the II-V family. For all these attempts the Bridgman method was used. Only  $(\text{Zn}_{1-x}\text{Mn}_x)_3\text{As}_2$  alloys and mixtures of  $(\text{Cd}_{1-x}\text{Mn}_x)_3\text{As}_2$  and

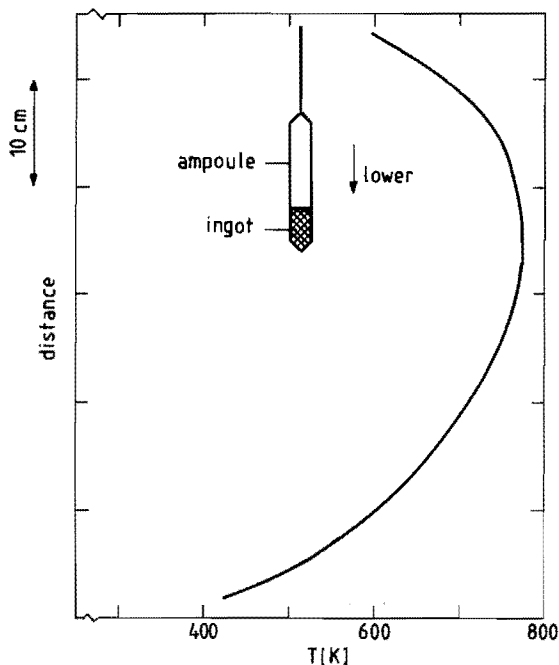


Fig. 5.1  
Temperature profile  
through which the sche-  
matically shown ampoule  
is moved.

$(\text{Zn}_{1-x}\text{Mn}_x)_3\text{As}_2$  could be grown as homogeneous single crystals. The  $(\text{Zn}_{1-x}\text{Mn}_x)_3\text{As}_2$  charge was heated to 1100 °C, which is above the melting temperature of  $\text{Zn}_3\text{As}_2$  (1015 °C [1]).

Although  $\text{Cd}_3(\text{As}_{1-y}\text{P}_y)_2$  and  $\text{CdSnAs}_2$  could be grown successfully as homogeneous crystals, the attempts to substitute a fraction of the Cd atoms by Mn failed. In these attempts the melts of the stoichiometric amounts of Cd-Mn-As-P and Cd-Mn-Sn-As were heated to 770 °C and 650 °C respectively.

In order to substitute the Cd atoms in  $\text{Cd}_3\text{As}_2$  by other atoms than Mn, ampoules were prepared with stoichiometric amounts of Cd, As and one of the following elements: Gd (925 °C), Cu (800 °C), Ni (850 °C), Fe (900 °C) and Cr (880 °C). The melts were heated to the temperatures between brackets. We did not succeed in growing these materials as homogeneous crystals as will be discussed in the section on the composition analysis. Also in the case of II-VI compounds it turned out to be impossible to dissolve elements other than Mn and Fe [4]. It is unclear why other elements do not dissolve homogeneously in II-V and II-VI compounds.

## 5.2 Crystal orientation

The as-grown samples were oriented with the standard von Laue X-ray back-reflection method. After obtaining the correct orientation, the crystals were cut with a wire saw into slabs of approximately 1 mm thickness. From these slabs the samples for the magnetoresistance measurements were cut. The bar shaped samples have typical dimensions of  $1 \times 1 \times 8$  mm. The long edge of the sample was cut parallel to a [100] or a [110] crystal axis, according to the desired experimental configuration.

## 5.3 Composition analysis

### *Mn concentration*

Three different methods were used to analyse the alloy composition: wet chemical analysis, particle induced X-ray emission (PIXE) and electron microprobe analysis.

The wet chemical analyses were performed at the Analytische Laboratorien in Elbach, Germany. This method gives the value of the average concentration of Mn in a volume of  $1 \text{ mm}^3$ . The uncertainty in the concentration values  $\Delta x/x$  is less than 2 percent for this method.

The PIXE measurements were done in the group Particle Physics of the Physics Department at our University [5]. Applying this method the samples are placed in a beam of protons, accelerated by a cyclotron to 3 MeV. The wavelength of the induced X-rays allows to identify the atoms present in the alloy. The concentrations of these atoms can be determined from the intensity of the X-rays. PIXE measurements are very sensitive and have a detection limit better than 1 ppm. The relative accuracy of this method is  $\Delta x/x = 10$  percent. A disadvantage of the apparatus used, is that the smallest spot, which can be examined on a sample, has a diameter of 2 mm. This makes homogeneity checks impossible.

This disadvantage can be overcome by using the Electron Microprobe Analysis [6]. These measurements were done in the group Physical Chemistry of the Chemistry Department at our University. This technique is similar to PIXE, only now the X-rays are induced by electrons

Table 5.1 Mn fraction  $x$  of the  $(\text{Cd}_{1-x}\text{Mn}_x)_3\text{As}_2$  and

$\text{Hg}_{1-x}\text{Mn}_x\text{Se}$  samples

$(\text{Cd}_{1-x}\text{Mn}_x)_3\text{As}_2$	Chem. Analysis	El. Micropr.	PIXE
1/4 CMA 3B	0.0022		0.0023
1/2 CMA 4B	0.0050		0.0070
3/4 CMA 2A	0.0071		0.0070
1 CMA 7B	0.0098	0.0099	0.0120
3/2 CMA 1A	0.0167	0.017	0.017
2 CMA 11B	0.0166	0.0169	0.017
4 CMA 5A	0.0322	0.0328	0.0317
$\text{Hg}_{1-x}\text{Mn}_x\text{Se}$			
2113-4	0.0056		
2114-4	0.014		
0.024	0.025		
2138-2-1	0.05		
153	0.10		
5 HMS	0.057		
0.2 HMS	0.0048		

with energies between 10 keV and 30 keV. The relative accuracy of this method is  $\Delta x/x = 2$  percent for  $x > 0.01$ . The electron beam diameter is smaller than  $1 \mu\text{m}$ . By moving the sample with respect to the electron beam, different spots of the sample surface can be analysed, which allows to determine the sample homogeneity. The results of the composition analysis for the samples used in our experiments are given in table 5.1.

From table 5.1 we conclude that the results for  $(\text{Cd}_{1-x}\text{Mn}_x)_3\text{As}_2$  obtained by the three methods agree quite well with each other. For  $\text{Hg}_{1-x}\text{Mn}_x\text{Se}$  we therefore decided to determine the composition only by one method.

#### Homogeneity of the Mn distribution

In ternary compounds grown by the Bridgman method, the composition is in general not homogeneous over the ingot. For  $(\text{Cd}_{1-x}\text{Mn}_x)_3\text{As}_2$ , this was tested by determination of the composition along the growth direction of the crystal. The result is shown in fig. 5.2 [7]. The Mn concentration is given versus the distance to the bottom of the ingot.

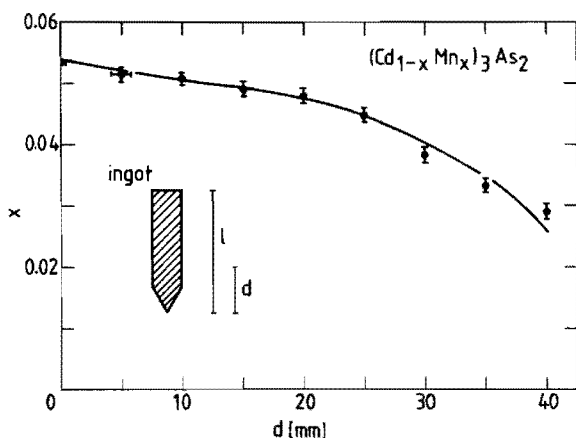


Fig. 5.2

Mn concentration dependence in the ingot as a function of  $d$ . The solid line represents eq. 5.1 with  $k = 1.2$ ,  $x_o = 0.045$  and  $l = 40$  mm [7].

It is clear that a large variation of Mn concentration may occur in one crystal. The concentration profile can be given by [8]:

$$x(d) = k x_o (1 - d/l)^{k-1}, \quad (5.1)$$

where  $x(d)$  is the Mn concentration as a function of the distance  $d$  to the bottom of the crystal.  $x_o$  is the initial value of the Mn concentration in the liquid and  $l$  is the length of the ingot.  $k$  is the ratio of the concentrations of Mn in the liquid and solid at the crystal-melt interface and is assumed to be independent of composition. The solid curve in fig. 5.2 is a fit using eq. 5.1 [7]. It is clear from the result of this  $(Cd_{1-x}Mn_x)_3As_2$  sample that the best homogeneity of the samples is expected when they are taken from slices which are cut perpendicular to the growth direction. This condition may be in conflict with the desired orientation of the crystal axis parallel to the long edge of the sample. In the case the long edge of the sample is not in the plane perpendicular to the growth direction a gradient in the Mn concentration can occur in the samples. Since we want to study anisotropy effects, we give priority to the correct crystal orientation over the possible problems arising from gradients in the Mn concentration.

A similar compositional inhomogeneity was also reported for  $Hg_{1-x}Mn_xSe$  [9]. In a typical sample with nominal  $x = 0.15$ , values of



$x = 0.05, 0.09, 0.13$  and  $0.22$  are measured. The Mn concentration gradient in  $\text{Hg}_{1-x}\text{Mn}_x\text{Se}$  is also caused by a significant difference in the composition of the solid and liquid phases during the sample growth. In the case of  $\text{Hg}_{1-x}\text{Mn}_x\text{Se}$  the growth direction is parallel to the  $[110]$ -axis. This implies that we can always find the  $[001]$  or  $[1\bar{1}0]$ -direction in a slice of the ingot, cut perpendicular to the growth direction. Therefore, the Mn concentration gradient along the growth direction does not conflict with the desired crystal orientation.

More severe kinds of inhomogeneities are observed in the  $\text{CdMnAsP}$  ingots. The analysis shows that a large fraction of the Mn reacted with P to MnP. Only a very small part of Mn ( $<0.5$  percent) dissolved in the  $\text{Cd}_3(\text{As}_{1-x}\text{P}_x)_2$  lattice. The inclusions of pure Cd and MnP make this ingot useless for further measurements.

In the case of  $\text{CdMnSnAs}$  some of the Mn dissolved. However, because inclusions of MnAs and SnAs occurred, this material could not be used in further measurements.

The attempts to dilute other elements than Mn in  $\text{Cd}_3\text{As}_2$  resulted in pure  $\text{Cd}_3\text{As}_2$  crystals with inclusions either of the pure element which was to be diluted or inclusions of a mixture of this element with As.

#### 5.4 Annealing

In order to obtain samples suitable for SdH measurements, it was necessary to anneal the as-grown crystals under different conditions. The as-grown  $(\text{Cd}_{1-x}\text{Mn}_x)_3\text{As}_2$  crystals already have an electron mobility, high enough to allow the observation of the SdH effect. However, the electron density of these materials is always in the range of  $2.0 \cdot 10^{24} \text{ m}^{-3}$  to  $5.0 \cdot 10^{24} \text{ m}^{-3}$ . For the determination of the band-structure parameters from the SdH measurements one needs also samples with electron densities below  $1.0 \cdot 10^{24} \text{ m}^{-3}$ . Therefore the  $(\text{Cd}_{1-x}\text{Mn}_x)_3\text{As}_2$  samples were subjected to an annealing procedure. The results of two sets of samples with  $x = 0.0075$  and  $x = 0.05$  are given in fig. 5.3. Of each Mn concentration, one sample was sealed with a piece of pure Cd in a quartz ampoule, a second sample with a piece of

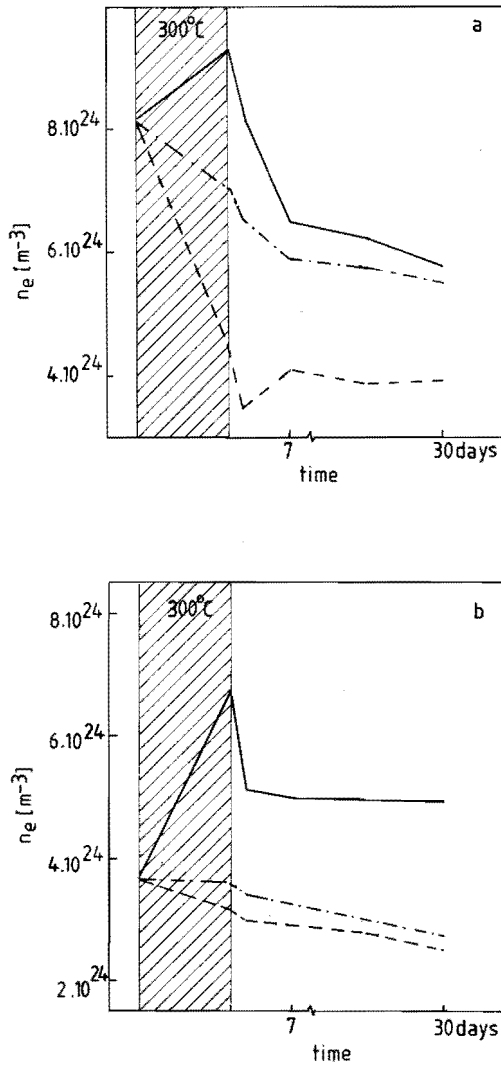


Fig. 5.3 Annealing history of  $(\text{Cd}_{1-x}\text{Mn}_x)_3\text{As}_2$  samples:  $x = 0.05$  (a) and  $x = 0.0075$  (b). The samples are annealed in Cd atmosphere (solid curve), As atmosphere (dashed curve) or in vacuum (dash-dotted curve).

As and a third without addition. To be able to compare the effects of annealing, we selected for each Mn concentration as-grown samples with equal carrier density. The furnace temperature was 300 °C. The electron densities of the samples were determined with the v.d. Pauw method [10]. The electron densities before, immediately after 72 hours annealing at 300 °C and after annealing at 120 °C in air, are shown in fig. 5.3. After annealing 17 days at 300 °C the annealing effect was the same as after 3 days at 300 °C. The lowest electron density obtained for  $x = 0.05$  is  $3.0 \cdot 10^{24} \text{ m}^{-3}$  and for  $x = 0.0075$  is  $1.5 \cdot 10^{24} \text{ m}^{-3}$ . Although a systematic analysis of the annealing effects was only done for these two Mn concentrations, the annealing of samples with other Mn concentrations yields similar results. The value of the lowest carrier density which could be obtained depends on the Mn composition. This value increases with increasing Mn content.

For  $\text{Hg}_{1-x}\text{Mn}_x\text{Se}$  and  $\text{HgSe}$  the annealing was not only used to change the carrier density but also to improve the electron mobility. For these materials, we followed the annealing procedure for  $\text{HgSe}$  as given by Brebrick and Strauss [11]. The samples were sealed in evacuated quartz ampoules together with a piece of Se. To avoid that the

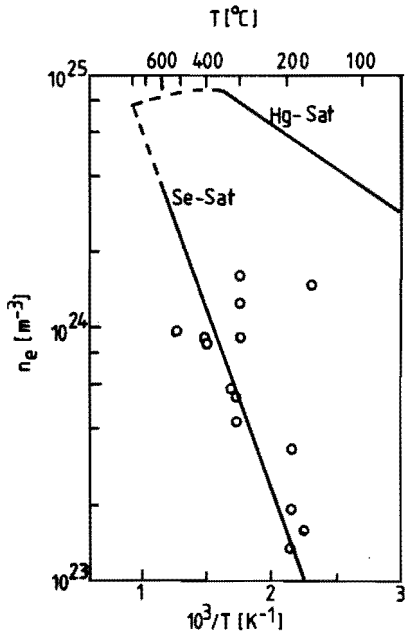


Fig. 5.4  
Variation of the electron density of  $\text{HgSe}$  samples with annealing temperature. The solid curves represent the electron densities as obtained in a Se or a Hg-saturated atmosphere in [11]. The circles represent our results.

liquid Se covered the sample when the annealing temperature was raised above the melting point of Se, the Se and the sample were separated by a constriction in the ampoule. By varying the annealing temperature, a broad range of electron densities could be obtained. Our results for HgSe are compared with the results of Brebrick and Strauss [11] in fig. 5.4. The deviation of our results from those of [11] are due to the annealing history of our samples. This indicates that in the cases where the deviations appear, the annealing period was not long enough to obtain a homogeneous electron distribution in the crystals.

For  $\text{Hg}_{1-x}\text{Mn}_x\text{Se}$  we obtained similar results. Contrary to the case of  $(\text{Cd}_{1-x}\text{Mn}_x)_3\text{As}_2$  we did not observe a relation between the Mn content and the minimum carrier density.

### 5.5 *Current and voltage leads*

The SdH magnetoresistance measurements are carried out with a four-point technique. The leads are of 50  $\mu\text{m}$  diameter copper wire. For  $(\text{Cd}_{1-x}\text{Mn}_x)_3\text{As}_2$  the leads are soldered to the sample with Rose metal (52.5-Bi, 32-Pb, 15.5-Sn). Some peculiarities in the magnetoresistance occurring when this solder material passes the superconducting-normal metal transition are reported in chapter 9. In the case of  $\text{Hg}_{1-x}\text{Mn}_x\text{Se}$  and HgSe the leads are attached with Demetron Silverpaint.

## REFERENCES

- [1] D.N. Nasledov, V.Ya. Shevchenko, *Phys. Stat. Sol. (a)* 15, 9 (1973).
- [2] A. Pajaczkowska, A. Rabenau, *Mat. Res. Bull.* 12, 183 (1977).
- [3] Landolt Börnstein, *Numerical data and functional relationships in science and technology, New Series, Vol. 176*, Springer Verlag, Berlin 1982, p. 236.
- [4] R.R. Gałazka, private communication.
- [5] H.P.M. Kivits, Ph.D. thesis, Eindhoven University of Technology, Eindhoven, 1980.
- [6] S.J.B. Reed, *Electron microprobe analysis*, Cambridge University Press (1975).
- [7] C.J.M. Denissen, Ph.D. thesis, Eindhoven University of Technology, Eindhoven, 1986.
- [8] J. Brice, in *Selected Topics in Solid Stat. Physics, Vol. 5*, ed. by E.P. Wohlfarth (Wiley, New York 1965) p. 73.
- [9] M. Vaziri, U. Debska, R. Reifenberger, *Appl. Phys. Lett.* 47, 407 (1985).
- [10] L.J. v.d. Pauw, *Philips Res. Rep.* 13, 1 (1958).
- [11] R.F. Brebrick, A.J. Strauss, *Proc. of Int. Conf. on II-VI Semicond. Comp.*, ed. D.G. Thomas (W.A. Benjamin Inc. New York, 1967), p. 425.

## CHAPTER VI EXPERIMENTAL TECHNIQUE.

This chapter deals with the experimental set-up. We start with the set-up for the SdH measurements. After a general description of the measuring circuit, we treat in more detail the field modulation technique, used to detect the small magnetoresistance oscillations of the SdH effect. We give the characteristics of the three magnet systems and corresponding cryostats we used in our experiments.

After a description of the experimental hardware we show how to extract the experimental parameters like the oscillation period, the carrier density and the spin splitting from our data.

At the end of this chapter a description of the Foner magnetometer used for the magnetisation measurements is given.

### 6.1 Shubnikov de Haas measurements

#### *Measuring circuit*

The experimental set-up for the SdH measurements is schematically shown in fig. 6.1. The sample (S) is placed in a magnetic field generated by the coils B1 and B2. If a constant DC current is passed through the sample S, the voltage drop across the sample is directly proportional to the resistivity. We used DC currents between 50 mA and 100 mA. The oscillatory component of the magnetoresistance is very small compared to the large non-oscillatory background. To be able to separate the small oscillatory component  $V_{osc}(B)$  from the background  $V_0(B)$ , magnetic field modulation and phase-sensitive detection are used [1,2]. An oscillator (OSC) generates a sine wave with  $\omega = 31$  Hz or 60 Hz, which is amplified (AMP) to drive the modulation coils (MC). A reference signal is sent to the lock-in amplifier. Because of the high input impedance of the lock-in and the low resistivity of the sample a 1 : 1000 impedance matching transformer (TRAFO) is used to connect the voltage probes of the sample to the lock-in. The lock-in amplifier selects the frequency components equal ( $\omega$ ) or twice ( $2\omega$ ) the modulation frequency from the input signal. Assuming that no background signal  $V_0$  or induction voltage due to the field modulation

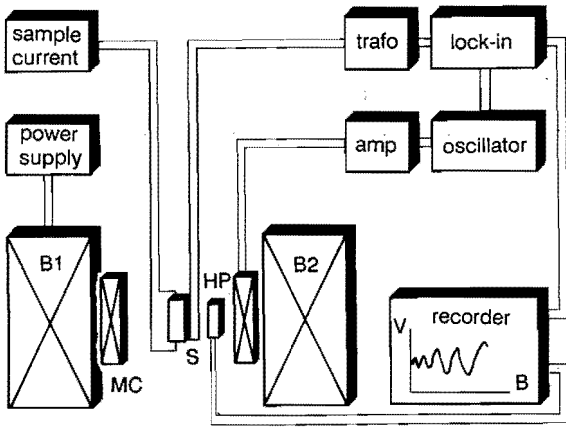


Fig. 6.1 Schematic drawing of the measuring circuit.  
Explanation is given in the text.

passes the lock-in amplifier, the lock-in output is proportional to the oscillatory part of the magnetoresistance  $\rho_{osc}$ .

The lock-in output is plotted versus the voltage of a Hall probe (HP) on a X-Y-recorder, resulting in a plot of the SdH oscillations versus the DC magnetic field. In order to avoid deformation of the recorded SdH signal, the time constant of the detection system must be at least ten times smaller than the time required to record one complete SdH oscillation [3]. This time can be varied by changing the sweep speed of the DC magnetic field.

Instead of collecting the SdH data on recorder graphs, the data can also be stored directly in a computer. The lock-in output and the analog output of a DC voltmeter, measuring the Hall voltage, are connected to an analog-digital converter. The Hall voltage cannot be measured directly by the computer because the oscillatory component of the modulation field adds an AC voltage to the Hall signal. The measuring program collects data in a pre-selected field range. The Hall voltages, for which the lock-in output is measured, are calculated in such a way that the data are collected at equidistant intervals in  $1/B$ .

### Field modulation

The modulation coils superimpose a small field  $B_m \cos(\omega t)$  on the slowly increasing main field  $B_o(t)$ . The field can now be written as  $B(t) = B_o(t) + B_m \cos(\omega t)$ . Substituting this in the expression for the oscillating magnetoresistance (eq. 2.8) yields

$$\frac{\Delta \rho}{\rho_o} = \sum_{r=1}^{\infty} A_r(B, T) \cos \left[ \frac{2\pi r}{PB_o + PB_m \cos(\omega t)} - \phi'_r \right] \quad (6.1)$$

where  $A_r(B, T)$  and  $\phi'_r$  are short notations for the amplitude and phase factors. The amplitude factor  $A_r(B, T)$  varies only very slowly with magnetic field and is therefore considered constant over the modulation field range. Under the condition  $B_m \ll B_o$ , eq. 6.1 can be rewritten as

$$\begin{aligned} \frac{\Delta \rho}{\rho_o} = \sum_{r=1}^{\infty} A_r(B, T) \left\{ \cos \left[ \frac{2\pi r}{PB_o} - \phi'_r \right] \cos(\alpha r \cos(\omega t)) \right. \\ \left. + \sin \left[ \frac{2\pi r}{PB_o} - \phi'_r \right] \sin(\alpha r \cos(\omega t)) \right\} \quad (6.2) \end{aligned}$$

Where  $\alpha = 2\pi B_m / (PB_o^2)$ . The factors  $\cos(\alpha r \cos(\omega t))$  and  $\sin(\alpha r \cos(\omega t))$  can be expressed in series of Bessel functions [4]. Substituting these series in eq. 6.2 we obtain

$$\begin{aligned} \frac{\Delta \rho}{\rho_o} = \sum_{r=1}^{\infty} A_r(B, T) \\ \left\{ \left[ J_o(\alpha r) + 2 \sum_{n=1}^{\infty} (-1)^n J_{2n}(\alpha r) \cos(2n\omega t) \right] \cos \left[ \frac{2\pi r}{PB_o} - \phi'_r \right] \right. \\ \left. + \left[ 2 \sum_{n=1}^{\infty} J_{2n+1}(\alpha r) \cos((2n+1)\omega t) \right] \sin \left[ \frac{2\pi r}{PB_o} - \phi'_r \right] \right\} \quad (6.3) \end{aligned}$$



From this equation we can see that field modulation, with frequency  $\omega$ , introduces harmonic frequency components in the magnetoresistance, and consequently in the voltage measured over the sample. Detection of the fundamental ( $\omega$ ) or the second ( $2\omega$ ) harmonic component of the signal results in DC lock-in output voltages given by

$$V_{\text{osc}(\omega)} = c \sum_{\Gamma} 2 A_{\Gamma}(B,T) J_1(r\alpha) \sin\left[\frac{2\pi r}{PB} - \phi'_{\Gamma}\right] \quad (6.4a)$$

$$V_{\text{osc}(2\omega)} = c \sum_{\Gamma} -2 A_{\Gamma}(B,T) J_2(r\alpha) \cos\left[\frac{2\pi r}{PB} - \phi'_{\Gamma}\right] \quad (6.4a)$$

where  $c$  is a proportionality constant. We see that in both cases the amplitude of each harmonic  $r$  is multiplied by a Bessel function factor  $J_1(r\alpha)$  or  $J_2(r\alpha)$ . Each time  $J_1(\alpha)$  or  $J_2(\alpha)$  equals zero, the amplitude of the first harmonic  $r=1$  vanishes. If the higher harmonics are sufficiently damped even the total SdH signal vanishes. This kind of nodes in the SdH amplitude can easily be distinguished from the nodes caused by the spin splitting (chapter 2), because the field position of the Bessel nodes changes when the amplitude of the modulation field is changed. An experimental SdH signal ( $P = 0.0275 \text{ T}^{-1}$  and

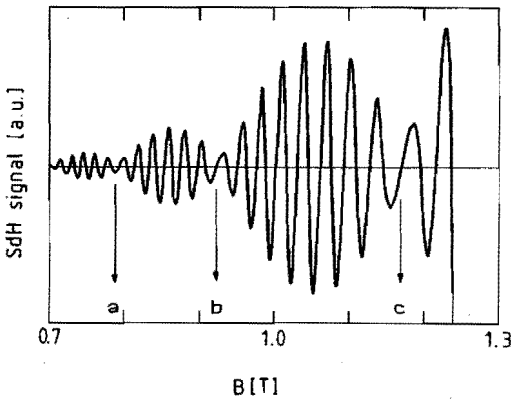


Fig. 6.2 An experimental SdH signal showing nodes in the amplitude due to the field modulation. The nodes indicated by a, b and c correspond to the nodes in the Besselfunction  $J_2(\alpha)$  as shown in fig. 6.3.

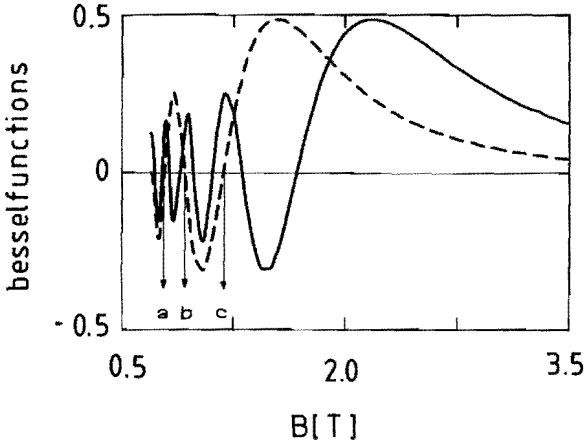


Fig. 6.3 The Besselfunctions  $J_2(\alpha)$  (dashed curve) and  $J_2(2\alpha)$  (solid curve) as a function of the main field B.  $P = 0.0275 \text{ T}^{-1}$  and  $B_m = 0.317 \text{ T}$  are the same as in fig. 6.2.

$B_m = 0.0317 \text{ T}$ ) showing the zeroes in  $J_2(\alpha)$  is given in fig. 6.2. The zeroes indicated by a, b and c correspond to  $\alpha = 11.62$ ,  $\alpha = 8.42$  and  $\alpha = 5.13$  respectively.

A second effect of the modulation is that the amplitude of the higher harmonics can be relatively increased compared to the amplitude of the first harmonic. This is shown in fig. 6.3.  $J_2(2\alpha)$  reaches its maximum at a field where  $J_2(\alpha)$  has already passed its maximum.

## 6.2 Cryostats and magnets

The SdH experiments were performed in three different set-ups. Most of the experiments were done in the low field set-up as shown in fig 6.4. By pumping the He vapour in the He bath cryostat (1) the temperature can be controlled between 1.4 K and 4.2 K. The He vapour pressure can be read at a Hg manometer. The He cryostat is enclosed in a liquid nitrogen cryostat (2). The "tail" of these cryostats is mounted between the poles (3) of a water-cooled electromagnet (4) which generates fields up to 2.1 T. The main field is measured by a Hall probe (5). The field is modulated by a pair of Helmholtz like

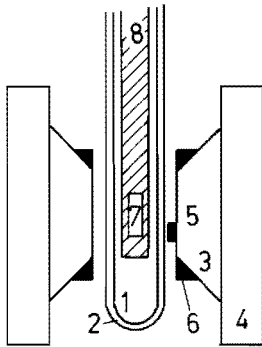


Fig. 6.4  
 Low field set-up with He bath cryostat.  
 The numbers are explained in the text.

coils (6) which are attached to the poles. The modulation amplitude is field dependent due to saturation effects of the iron core. The sample holder can be rotated around a vertical axis, allowing to measure the dependence of the magnetoresistance on the field orientation.

A second low field set-up is shown in fig. 6.5. Due to the essentially different construction of the cryostat, also temperatures above 4.2 K can be reached. The sample (1) is mounted on a sampleholder (2)

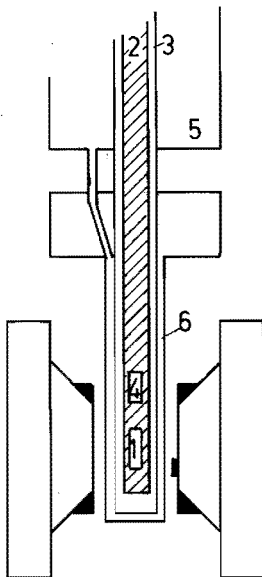


Fig. 6.5  
 Low field set-up for experiments in the  
 temperature range from 1.5 to 25 K.  
 The numbers are explained in the text.

which is placed in the sample tube (3). The sample tube is filled with He exchange gas to provide a good thermal conductivity between the He reservoirs (5) and (6) and the sample. For measurements below 4.2 K, the temperature is controlled in the same way as in the set-up described above. The temperature is measured by a carbon glass resistor (4) positioned close to the sample. For measurements above 4.2 K the temperature is defined by the equilibrium between the heat input of a heating wire close to the sample and the cooling power of the He bath at 4.2 K, surrounding the sample tube. In this way temperatures up to 25 K can be obtained. The magnet system with modulation coils and Hall probe are basically the same as in the other low field set-up. The maximum field is 1.5 T. Again the sample can be rotated around a vertical axis.

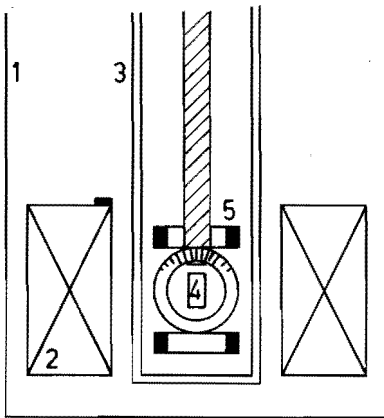


Fig. 6.6  
High field set-up with He bath insert dewar. The numbers are explained in the text.

The high field set-up (fig. 6.6) consists of a stainless steel cryostat (1) and a He-cooled superconducting solenoid (2). This magnet system generates fields up to 6 T. To be able to control the sample temperature separately from the main bath an insert cryostat (3) is placed in the center of the coil. The samples are placed on a rotatable sample holder (4). The modulation field is generated by a pair of Helmholtz coils (5). The Hall probe (6) is mounted on top of the superconducting coil. The sample can be rotated around a horizontal axis, perpendicular to the magnetic field.

### 6.3 Methods of data analysis

#### The Shubnikov de Haas oscillation period

As can be seen in eq. 2.6 the SdH oscillation period is inversely proportional to the extremal cross sectional area of the Fermi surface perpendicular to the magnetic field. Therefore an analysis of the oscillation period  $P$  as a function of the crystal orientation with respect to the magnetic field is a useful tool to study the shape of the Fermi surface. The oscillation period is determined by the following procedure. When only the first harmonic can be observed  $\Delta\rho/\rho_0$  can be written as

$$\frac{\Delta\rho}{\rho_0} = A_1(B,T) \cos\left[\frac{2\pi}{PB} - 2\pi\gamma - \frac{\pi}{4}\right] \cos(\pi\nu) \quad (6.5)$$

Maxima of the oscillations occur at

$$\left[\frac{2\pi}{P(\vartheta)B} - 2\pi\gamma - \frac{\pi}{4}\right] = m\pi \quad (6.6)$$

where  $m$  is an integer.  $\gamma$  is independent of magnitude and orientation of the field in the range where the data are taken. A plot of the reciprocals of the field positions of the maxima versus integers, gives a straight line. The slope of this line corresponds to the oscillation period  $P(\vartheta)$ . Repeating this procedure for different orientations yields the angular dependence of the period  $P(\vartheta)$ .

A more accurate method to determine the orientation dependence of the oscillation period was first used by Seiler [5]. Assuming  $\gamma$  and  $m$  to be constant, it is easily seen that the product  $P(\vartheta)B$  is constant in eq. 6.6. This implies that the field positions of the oscillation maxima shift when the oscillation period changes with orientation. The relative change in the period can be obtained by measuring the shift of these field positions using the relation

$$\frac{\Delta P}{P_0} = \frac{P_0 - P(\vartheta)}{P_0} = \frac{B(\vartheta) - B_0}{B(\vartheta)} \quad (6.7)$$

$P_0$  is the reference period determined by the procedure given above.  $B_0$  is the reference field. This procedure can only be used in the case the oscillations are not distorted by nodes in the amplitude of the oscillations.

Knowing the shape of the anisotropy in the oscillation period we can determine the orientation of the magnetic field with respect to the crystal axes. The samples are mounted with their long edge and corresponding crystal axis perpendicular to the magnetic field. In that case we only know in which crystallographic plane the field is. The exact orientation has to be determined by searching maxima and minima in the oscillation period. This is illustrated for a  $\text{Hg}_{1-x}\text{Mn}_x\text{Se}$  sample in fig. 6.7. In this case the magnetic field is in the (110)-plane, and the oscillation period has maxima for  $B \parallel [110]$  and  $B \parallel [001]$  and a minimum for  $B \parallel [111]$ .

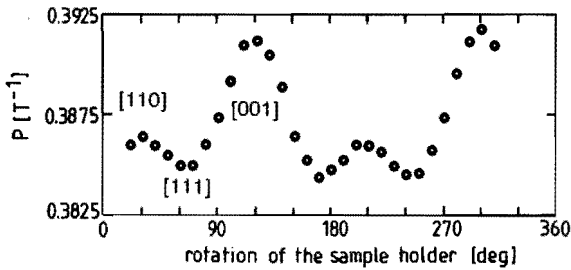


Fig. 6.7 Anisotropy of the SdH oscillation period for  $B$  in the (110)-plane. The magnetic field orientations are indicated for the maxima and minima.

#### The carrier density

As already has been shown in the chapter on the SdH effect, the carrier density can be obtained from the oscillation period

$$n_e = \frac{1}{3\pi^2} \left[ \frac{2e}{\hbar} \right]^{3/2} P^{-3/2} \quad (6.8)$$

in the case the Fermi surface is spherical. The anisotropy in the oscillation period due to warping can be neglected for the determination of the carrier density. For the ellipsoidal Fermi surface of  $(\text{Cd}_{1-x}\text{Mn}_x)_3\text{As}_2$  the carrier density is given by

$$n_e = \frac{1}{3\pi^2} \left[ \frac{2e}{\hbar} \right]^{3/2} \left[ P_o P_{9o}^2 \right]^{-1/2} \quad (6.9)$$

where  $P_o$  and  $P_{9o}$  are the oscillation periods for  $B \parallel [001]$  and  $B \parallel [100]$  respectively.

#### *The cyclotron effective mass*

Examination of the theoretical expression for the amplitude of the SdH oscillations shows that the cyclotron effective mass can be determined from the temperature dependence of the SdH amplitude at constant field. However, in SMSC the  $\cos(r\pi\nu)$  factor in the expression for the SdH amplitude is temperature dependent too. This fact hampers the determination of effective cyclotron masses in SMSC. Instead of going into a difficult analysis of the experimental data to obtain the effective masses, the masses we needed for the interpretation of the data were obtained from calculations using the bandstructure models given in chapter 3.

#### *The spin splitting*

As already discussed in the chapter on the SdH effect the spin splitting of the Landau levels can be studied by using the nodes in the oscillation amplitude. For the combination of field strength, field orientation and temperature where the node occurs we can calculate the Landau splitting  $\Delta E_L$  from our band model. Via  $\nu = \Delta E_{sp} / \Delta E_L$  we can determine the spin splitting using the condition that  $\nu = k + 1/2$  in a node. The method to determine the actual value of  $k$  will be discussed in the chapter on the experimental results on  $Hg_{1-x}Mn_xSe$ .

### 6.4 Magnetisation measurements

Magnetisation measurements in fields up to 6 T and temperatures between 1.4 and 25 K were performed with a vibrating sample magnetometer. A apparatus like this was first designed by Foner [6]. A sample is placed in a uniform magnetic field which induces a magnetic moment proportional to the magnetisation in the sample. During a

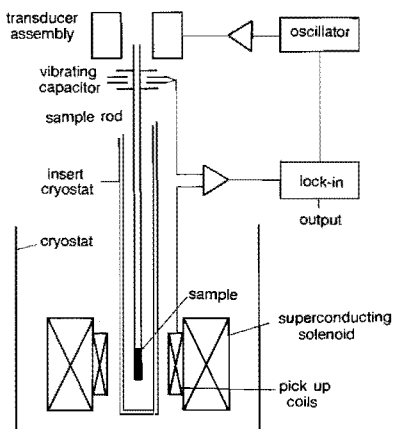


Fig. 6.8  
Schematic drawing of the  
Foner magnetometer.

sinusoidal motion of the sample the magnetic moment induces an electric signal in suitably located pick-up coils.

A schematic drawing of the magnetometer is given in Fig. 6.8. The sample is mounted on a slender rod which is placed in a double walled tube. The sample tube itself is filled with He exchange gas. The He gas pressure in the space between the double walls can be controlled in order to create the optimal heat exchange over the whole temperature range of operation.

The sample rod is connected to a transducer assembly, located above the magnet. The transducer converts a sinusoidal drive signal into a vertical sinusoidal vibration of the sample rod. The pick-up coils are mounted inside the cryostat. The AC signal from the pick-up coils is proportional to the magnitude of the induced moment ( $M$ ), the frequency ( $\omega$ ) and the amplitude ( $A$ ) of the oscillation. The induced voltage is given by

$$V_{\text{coil}} = -L \frac{d\Phi}{dt} = -f i \omega A M \exp(i\omega t) \quad (6.10)$$

where  $f$  is a proportionality constant. This constant can be found by calibration of the magnetometer with a pure nickel sample of which the magnetisation is accurately known.



The data can be collected with a computer in a similar way as the SdH data. The parameters  $S_0$  and  $T_0$  in the modified Brillouin function (eq. 3.7) are obtained with a least squares fitting program.

#### REFERENCES

- [1] A. Goldstein, S.J. Williamson, S. Foner, Rev. Sci. Instr. 36, 1356 (1965).
- [2] L.S. Lerner, Phys. Rev. 127, 1480 (1962).
- [3] J.J. Neve, Ph.D. thesis, Eindhoven University of Technology Eindhoven, 1984.
- [4] G. Arfken, Mathematical Methods for Physicists, 3rd ed. (Academic Press inc. New York, 1985).
- [5] D.C. Seiler, Phys. Rev. B1, 2824 (1970).
- [6] S. Foner, Rev. Sci. Instr. 27, 548 (1956), 30 548 (1959).

## CHAPTER VII EXPERIMENTAL RESULTS ON $\text{Hg}_{1-x}\text{Mn}_x\text{Se}$ AND THEIR INTERPRETATION.

This chapter deals with the experimental results on  $\text{Hg}_{1-x}\text{Mn}_x\text{Se}$  and their interpretation. Most of the bandparameters used for the interpretation of our experimental results are taken from literature. The actual choice of the parameter values is discussed in the first section of this chapter. The parameters describing the magnetic behaviour of the Mn spins are obtained from magnetisation measurements. The analysis of the SdH measurements concentrates on the anisotropy of the oscillation period and of the field positions of the nodes in the oscillation amplitude. For the interpretation of the nodal positions we use our new bandstructure model presented in chapter 3. The additional parameters describing the exchange interaction and the inversion asymmetry are determined from our experimental results. Finally we discuss the effects of splitting of the electron spin levels in the absence of a magnetic field.

### 7.1 Bandparameters

As in all compound semiconductors the energy bandgap of  $\text{Hg}_{1-x}\text{Mn}_x\text{Se}$  varies with composition. Takeyama et al. [1] found the following empirical relation

$$E_g = -0.270 + 4.4 x \text{ eV} \quad (7.1)$$

which was corroborated by other authors in independent experiments [2,3]. The momentum matrix element  $P = 7.2 \cdot 10^{-10} \text{ eVm}$  and the spin-orbit split off energy  $\Delta_{so} = 0.39 \text{ eV}$  are taken equal to those of HgSe [4]. Although several papers report a composition dependence of  $P$  and  $\Delta_{so}$  [1,3,5], Byszewski et al. [2] found a negligible shift of the calculated field positions of the SdH oscillation peaks due to variation of these parameters.

For the so-called higher band parameters  $\gamma_1, \gamma_2, \gamma_3, \kappa$  and  $F$  we used the HgSe values. The values of those parameters are mainly de-

terminated by the energy distance from the  $\Gamma_6$ ,  $\Gamma_7$  and  $\Gamma_8$  bands to the higher bands. Although the  $\Gamma_6$ ,  $\Gamma_7$  and  $\Gamma_8$  band energies shift about 50 meV per percent of Mn, this shift is small compared to the energy distance to the higher bands. Therefore, the higher band parameters are not expected to change very drastically for low Mn concentrations, and we use the HgSe values for these parameters also in the calculations for  $\text{Hg}_{1-x}\text{Mn}_x\text{Se}$ . However, for HgSe several different sets of values for these parameters are reported. Because we are interested in the spin splitting of the conduction band it is obvious to take a set of higher band parameters determined in an experiment concentrating on the spin splitting of the conduction band [4]. These parameters are listed in table 7.1. F is taken equal to zero, because the spin splitting of the  $\Gamma_8$  conduction band is not sensitive to this parameter. F influences only the spin splitting of the  $\Gamma_6$  band. The difference  $\gamma_2 - \gamma_3$  actually describes the warping anisotropy of the Fermi surface. The numerical value of  $\gamma_2 - \gamma_3$  given in [4] is in agreement with the other reported sets of higher band parameters [6,7]. It is important to note that the higher band parameters of [4] were determined using the Pidgeon Brown model, i.e. neglecting inversion asymmetry effects. We calculated the influence of the inversion asymmetry on the spin splitting under the same experimental conditions for which

$E_g$	=	$-0.270 + 4.4 x$	eV
P	=	$7.2 \cdot 10^{-10}$	eVm
$\Delta_{so}$	=	0.390	eV
$\gamma_1$	=	5.77	
$\gamma_2$	=	-1.17	
$\gamma_3$	=	-0.57	
$\kappa$	=	0.98	
F	=	0	
$N_1$	=	0	
q	=	0	

Table 7.1 Bandparameters  
 for  $\text{Hg}_{1-x}\text{Mn}_x\text{Se}$

these higher band parameters were determined. Like already shown in chapter 4 the inversion asymmetry contribution becomes smaller with increasing magnetic field. For carrier densities of approximately  $1.0 \cdot 10^{24} \text{ m}^{-3}$  the inversion asymmetry contributes at 5 T less than 5 percent to the spin splitting. For lower carrier densities and higher fields [4] this contribution becomes even smaller. Therefore we feel justified to use this set of higher band parameters, although this set has been determined without taking the inversion asymmetry into account.

Both parameters  $N_1$  and  $q$  influence the spin splitting of the  $\Gamma_8$  conduction band. However  $N_1$  acts mainly on the spin splitting of the  $\Gamma_6$  band. Both  $N_1$  and  $q$  contribute in a similar way to the anisotropy of the spin splitting as the higher band parameters described above.  $N_1$  and  $q$  do not give a significant refinement of the description of the spin splitting of the conduction band. The warping of the Fermi surface remains unaffected by these parameters. Taking into account these considerations we put  $N_1$  and  $q$  equal to zero.

The values of the other band parameters like the exchange integrals  $\alpha$  and  $\beta$  and the inversion asymmetry parameters  $C$ ,  $G$  and  $N_2=N_3$  are discussed later on.

## 7.2 Magnetisation

A typical example of magnetisation results measured for different temperatures is shown in fig. 7.1 for  $\text{Hg}_{0.975}\text{Mn}_{0.025}\text{Se}$ . The data are fitted with the modified Brillouin function (eq. 3.7). The fit parameters  $S_o$  and  $T_o$  for this and other samples are listed in table 7.2. For temperatures below 4.2 K, which is the region in which our SdH data were taken, the temperature dependence of  $S_o$  and  $T_o$  can be linearised

$$S_o = S_{oo} + S_{o1} T \quad (7.2)$$

$$T_o = T_{oo} + T_{o1} T \quad (7.3)$$

Table 7.2 Magnetisation fit parameters  
 $S_o$  and  $T_o$  for  $Hg_{1-x}Mn_xSe$

x = 0.0048		
T	$S_o$	$T_o$
2.53	1.43	0.10
3.22	1.73	0.37
4.20	1.82	0.20
6.0	2.24	0.95
9.0	2.55	0.98

x = 0.0055 sample 2113-4		
T	$S_o$	$T_o$
1.5	1.64	0.16
2.24	1.62	0.12
3.20	1.58	-0.00
4.22	1.55	-0.19
7.5	1.34	-1.10
10.0	1.04	-3.44
15.0	0.83	-5.9

x = 0.014 sample 2114-3		
T	$S_o$	$T_o$
1.5	1.45	0.96
2.25	1.44	1.00
3.25	1.42	0.97
4.25	1.36	0.86
7.5	1.21	0.08
10	1.16	0.2
15	0.92	-3.2

x = 0.025		
T	$S_o$	$T_o$
1.6	1.58	2.32
2.18	1.54	2.14
3.19	1.66	2.54
4.2	1.55	2.24
7.5	1.47	1.9
12.0	1.33	0.5
18.0	1.44	0

x = 0.05 sample 2138-2-1		
T	$S_o$	$T_o$
1.4	1.13	3.73
2.25	1.14	3.77
3.18	1.19	3.90
4.2	1.18	3.82
7.5	1.14	3.1
12	1.01	0.75
17	1.38	0

x = 0.057		
T	$S_o$	$T_o$
1.6	1.09	3.69
2.41	1.04	3.19
3.20	1.04	3.23
4.20	1.11	3.72
11.5	1.34	2.03

x = 0.106 sample 153-4		
T	$S_o$	$T_o$
1.4	0.61	4.90
2.25	0.63	4.85
3.18	0.64	4.80
4.2	0.59	3.69
7.5	0.58	2.5
12	0.60	1.7
18	0.44	-5.1

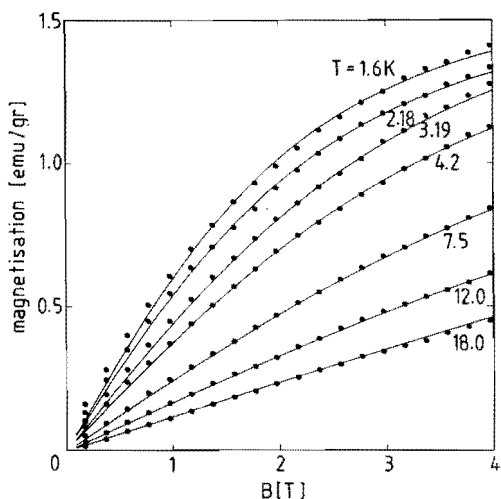


Fig. 7.1  
The magnetisation of  $\text{Hg}_{0.975}\text{Mn}_{0.025}\text{Se}$  for different temperatures. The curves are fits with the modified Brillouin function.

The values of  $S_{00}$ ,  $S_{01}$ ,  $T_{00}$  and  $T_{01}$  are listed in table 7.3.

The temperature dependence of  $S_0$  and  $T_0$ , we observed in our experiments is neglected in the determination of  $S_0$  and  $T_0$  in ref. [8,9]. Raw data on the magnetisation are given only by Staguhn [9] for  $x = 0.02$  and  $x = 0.042$ . These data were measured in fields up to 15 T. We analysed these data in the field range ( $B < 5$  T) and temperature range ( $T < 4.2$  K) which are of interest for our SdH data. The obtained fit parameters  $S_0$  and  $T_0$  are given in table 7.4. The bottom line gives the temperature independent parameters determined over the whole temperature and field range by Staguhn [9]. Comparing these parameters to those obtained from our own experiments we conclude that our

Table 7.3. Coefficients for the linear temperature dependence of  $S_0$  and  $T_0$ .

x	sample	$S_{00}$	$S_{01}$	$T_{00}$	$T_{01}$
0.0048		1.13	0.165	-0.49	0.24
0.0055	2113-4	1.0	0.036	0.39	-0.13
0.014	2114-4	1.50	-0.030	1.06	-0.039
0.025		1.58	0.0	2.31	0.0
0.050	2138-2-1	1.10	0.023	3.66	0.054
0.057		1.08	0.0	3.46	0.0
0.106	153.4	0.64	-0.01	5.73	-0.42

Table 7.4 Magnetisation fit parameters for  $Hg_{1-x}Mn_xSe$  from the data by Stuguhrn [9]

x = 0.02			x = 0.042		
T	$S_o$	$T_o$	T	$S_o$	$T_o$
2.0	1.30	1.8	1.8	1.45	2.7
4.2	1.35	2.1	4.2	1.50	3.4
[9]	1.35	1.7	[9]	1.5	5.2

results could not have been obtained by the interpolation of the results in table 7.4.

In [10] a similar temperature dependence of  $S_o$  and  $T_o$  was observed as in our experiments. However, in [10] only data for  $x > 0.05$  were fitted with the modified Brillouin function. For lower  $x$  no direct experimental results were given in [10].

From the comparison of our experimental results with those published in literature [8-10] we conclude that the fit of the magnetisation data is improved by using temperature dependent fit parameters  $S_o$  and  $T_o$ .

### 7.3 Shubnikov de Haas results and discussion

In this section we present the results of the SdH measurements on HgSe and  $\text{Hg}_{1-x}\text{Mn}_x\text{Se}$ . Fig. 7.2 presents a typical set of SdH measurements taken at 2.2 K on a  $\text{Hg}_{0.975}\text{Mn}_{0.025}\text{Se}$  sample with a carrier density of  $1.2 \cdot 10^{24} \text{ m}^{-3}$ . The angle between the magnetic field and the [001]-axis is indicated in the left part of the figure. A strong variation of the nodal field position with magnetic field orientation is clearly observed. The shift of the oscillation peak positions corresponding to the anisotropy in the oscillation period is less visible on this scale.

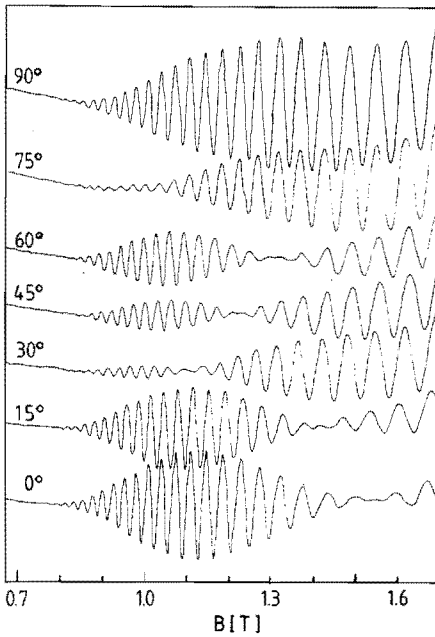


Fig. 7.2  
SdH recorder traces for  $\text{Hg}_{0.975}\text{Mn}_{0.025}\text{Se}$  at 2.22 K for  $n_e = 1.2 \cdot 10^{24} \text{ m}^{-3}$  at various magnetic field orientations. The field is in the  $(\bar{1}\bar{1}0)$ -plane. Angles between magnetic field and [001]-axis are given.

#### 7.3.1 Shubnikov de Haas oscillation period

Figs. 7.3 to 7.5 give the first experimental results of measurements of the anisotropy of the SdH oscillation period for  $\text{Hg}_{1-x}\text{Mn}_x\text{Se}$ . For comparison the anisotropy of the oscillation period of pure HgSe is given in fig. 7.6. For each sample data were taken for different carrier densities.



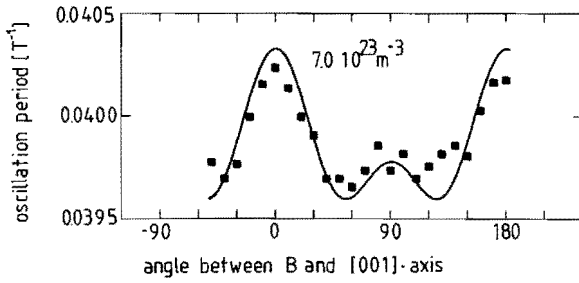


Fig. 7.3 The anisotropy of the oscillation period in  $\text{Hg}_{1-x}\text{Mn}_x\text{Se}$  with  $x = 0.014$ . The curve is calculated with the modified Pidgeon Brown model.

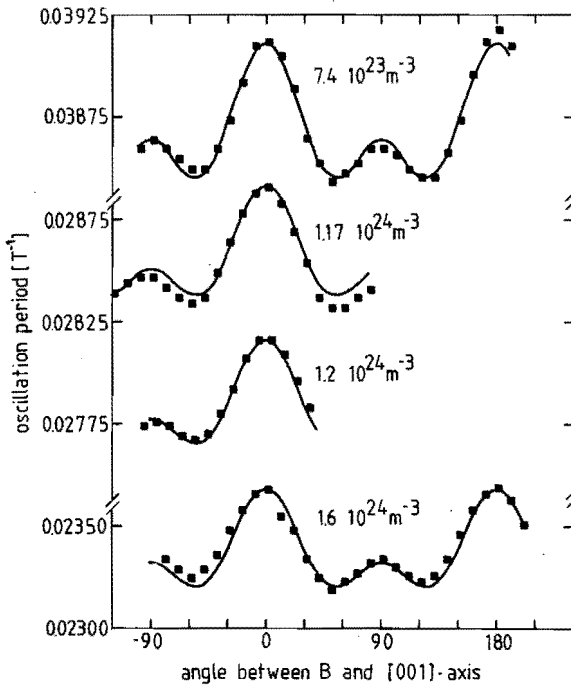


Fig. 7.4 As fig. 7.3 for  $x = 0.025$ .

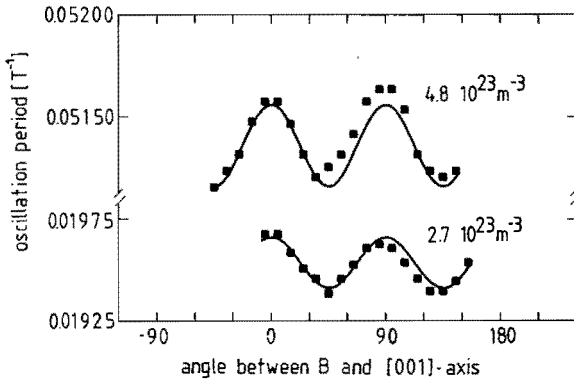


Fig. 7.5 As fig. 7.3 for  $x = 0.05$ .

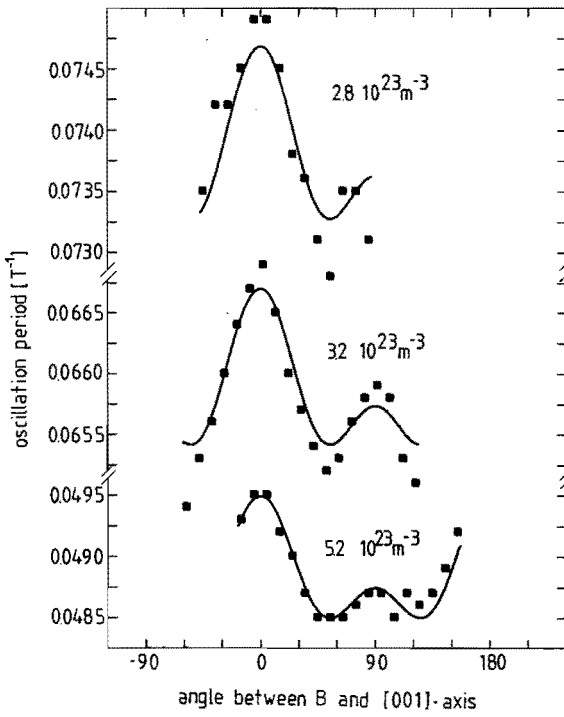


Fig. 7.6 As fig. 7.3 for HgSe.

In all cases except for  $x = 0.05$  the magnetic field was rotated around the  $[110]$ -axis, permitting the orientations  $B \parallel [110]$ ,  $[111]$  and  $[001]$  (configuration 1 in fig 7.7). For the  $x = 0.05$  sample  $B$  was rotated around the  $[001]$ -axis allowing the orientations  $B \parallel [110]$  and  $[100]$  (configuration 2 in fig 7.7). The curves are calculated with the modified Pidgeon Brown model (section 3.1.5) for the parameters given in table 7.1, using only the Fermi energy as a fit parameter.

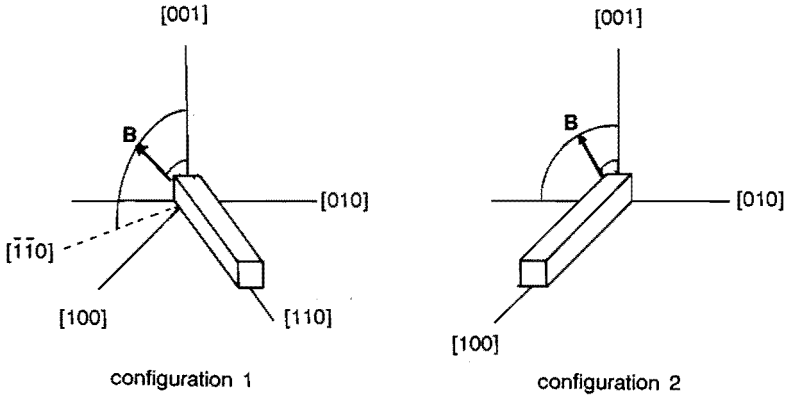


Fig. 7.7 Definition of the orientations.

In the field region where the data were taken, the spin splitting of the oscillation peaks remains unresolved. In that case the observed peak positions are determined by the superposition of a spin-up and a spin-down peak. The resulting peak position is related to the mean value of the spin-up energy and the spin-down energy for a certain Landau level. Because we are dealing with the mean energy values for both spin levels, the splitting of the levels does not affect the oscillation peak positions. Therefore the inversion asymmetry and the exchange interaction can be neglected in the determination of the anisotropy of the oscillations. The mean energy follows the warping of the bands which is well described by the Pidgeon Brown model, using only the higher band parameters  $\gamma_1$ ,  $\gamma_2$ ,  $\gamma_3$ ,  $\kappa$  and  $F$ . The good fit of the oscillation period for all  $\text{Hg}_{1-x}\text{Mn}_x\text{Se}$  samples using the  $\text{HgSe}$  values of the higher band parameters, proves that the  $\text{Mn}$  composition has a negligible influence on these parameters for low  $x$ .

### 7.3.2 Nodes in the Shubnikov de Haas oscillation amplitude

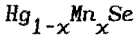


Fig. 7.2 shows some typical SdH recorder traces for a  $\text{Hg}_{1-x}\text{Mn}_x\text{Se}$  sample with  $x = 0.025$  for  $T = 2.22$  K. The nodal field positions observed in these curves are plotted in fig. 7.8b as a function of the field orientation. The angular dependence of the nodes observed for other temperatures is also shown in fig. 7.8b. Fig. 7.8a gives similar curves as fig. 7.8b for the same sample, for a different carrier density. All data were taken for the sample in configuration 1.

Figs. 7.9a,b and 7.10 show the nodes for the samples with  $x = 0.05$  and  $x = 0.0055$ . These data were taken for the sample configuration 2. The nodes observed for the  $x = 0.05$  sample clearly shift with temperature, whereas the nodal positions for the  $x = 0.0055$  sample depend only weakly on the temperature.

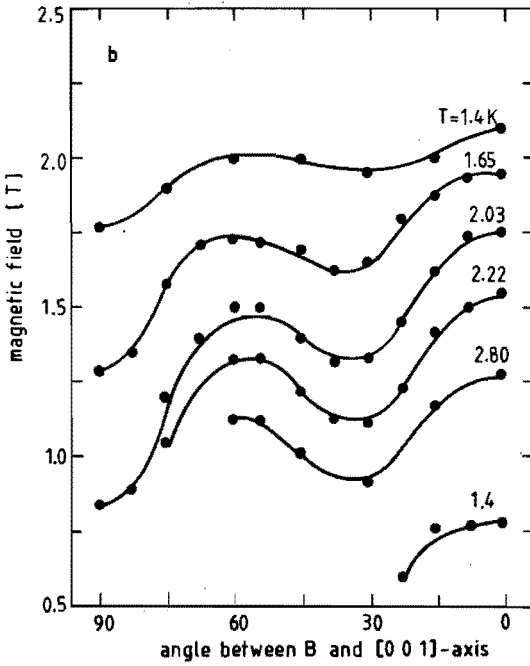
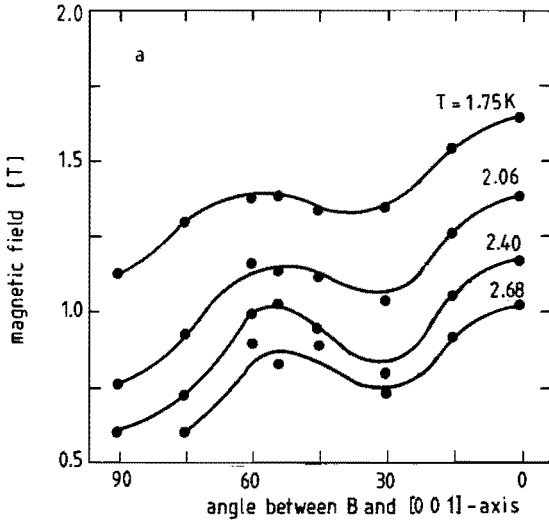


Fig. 7.8 Variation of the nodal field positions for  $\text{Hg}_{0.975}\text{Mn}_{0.025}\text{Se}$  with magnetic field orientation at different temperatures for (a)  $n_e = 7.4 \times 10^{23} \text{ m}^{-3}$  and (b)  $n_e = 1.2 \times 10^{24} \text{ m}^{-3}$ .

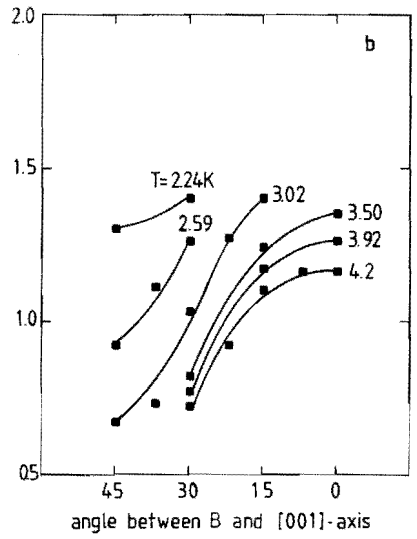
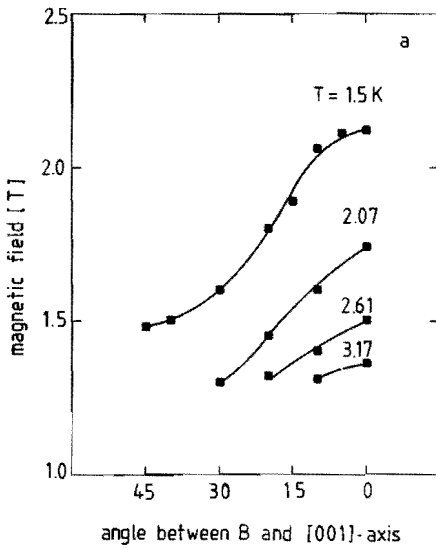


Fig. 7.9 Variation of the nodal field positions for  $\text{Hg}_{0.95}\text{Mn}_{0.05}\text{Se}$  with magnetic field orientation at different temperatures for (a)  $.8 \cdot 10^{23} \text{ m}^{-3}$  and (b)  $n_e = 2.7 \cdot 10^{24} \text{ m}^{-3}$ .

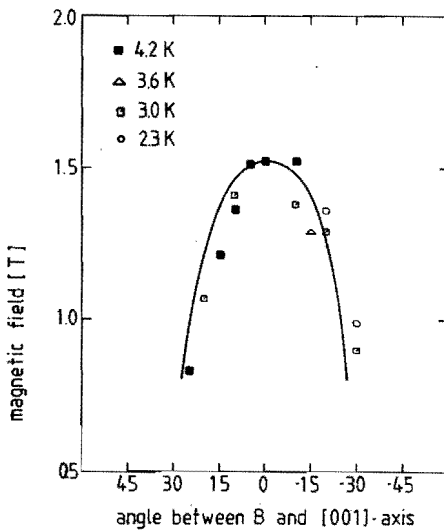


Fig. 7.10 Variation of the nodal field positions for  $\text{Hg}_{0.995}\text{Mn}_{0.005}\text{Se}$  with magnetic field orientation at different temperatures for  $n_e = 4.5 \cdot 10^{23} \text{ m}^{-3}$ .

## HgSe

For comparison we also measured the nodal field positions for pure HgSe as shown in fig. 7.11. These nodes are insensitive to temperature variations. Our observations of the shape of the anisotropy of the nodal field positions, the temperature behaviour and the dependence on the carrier density agree with the results reported by Whitsett [11] and Seiler et al. [12]. Fig. 7.12 by Seiler et al. [12] shows for  $B \parallel [001]$  a second maximum in the nodal fields. Our samples did not show SdH oscillations in the low field region where these maxima and the other low field nodes were observed.

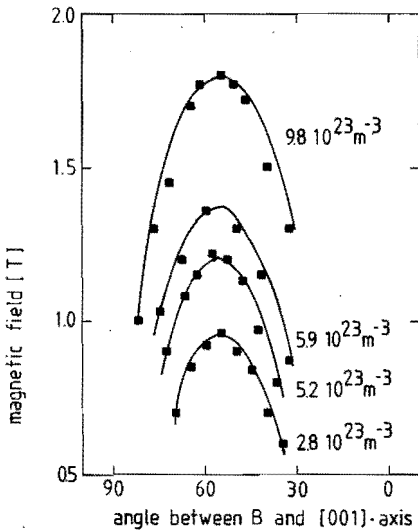


Fig. 7.11

Variation of the nodal field positions for HgSe with magnetic field orientation at different temperatures for different carrier densities.

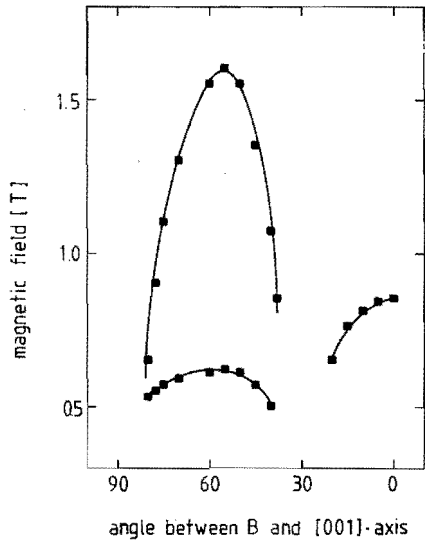


Fig. 7.12

Nodal field positions for HgSe as measured by Seiler et al. [12].

### Discussion of the results

From the results for the  $\text{Hg}_{1-x}\text{Mn}_x\text{Se}$  samples with  $x = 0.025$  and  $x = 0.05$  we can deduce the following essential features.

- i) The nodes shift smoothly with changing field orientation similarly as for pure HgSe. Maxima in the nodal fields are observed for the same orientations as for HgSe namely for  $B \parallel [111]$  and  $B \parallel [001]$ .
- ii) The nodes shift towards lower fields when the carrier density decreases.
- iii) The nodal fields are strongly temperature dependent.

From i) and ii) we conclude that the anisotropy of the nodes is related to the same mechanism causing the nodes in pure HgSe. The nodes in HgSe are caused by the splitting of the conduction band due to the lack of inversion symmetry in the zinc blende structure [13,14]. The shape of the anisotropy of the nodal positions remains the same, irrespectively of the Mn concentration. The nodes in HgSe are temperature independent in contrast to iii). Even for a small amount of Mn ( $x = 0.0055$ ), the nodal field positions shift with temperature. This temperature dependence of the nodes is, like for other SMSC [15], attributed to the exchange interaction.

From the discussion above it is clear that we need a model which includes both the effects of inversion asymmetry and exchange interaction to give an accurate description of the dependence of the nodes on field orientation and temperature.

We will emphasise the need for a new model, by showing that the modified Pidgeon Brown model fails to describe the angular dependence of the nodes (fig. 7.13). The nodal field positions as predicted by the modified Pidgeon Brown model are given by the solid curve. The parameters used in these calculations are the same as those used to describe the anisotropy of the oscillation period except for the exchange integrals  $\alpha = -0.8$  eV and  $\beta = 1.3$  eV as determined in the next section.



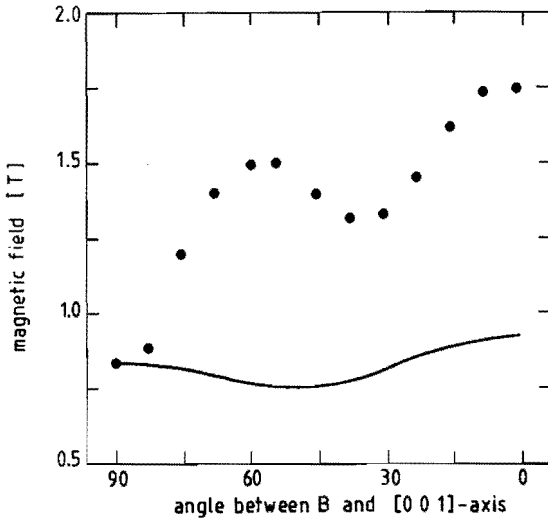


Fig. 7.13  
 Observed nodal field positions for  $\text{Hg}_{0.975}\text{Mn}_{0.025}\text{Se}$  at 2.03 K, compared to the positions predicted by the modified Pidgeon Brown model (solid curve).

### 7.3.3 Exchange interaction

For the determination of the exchange integrals we have to separate the exchange part of the spin splitting from the other contributions as given in eq. 2.9. As we have seen in fig. 4.2 the inversion asymmetry does not contribute to the spin splitting for B oriented parallel to the [110]-axis. Therefore we use only data obtained for this orientation. In that case only the spin-orbit interaction and the exchange interaction contribute to the spin splitting. The magnitude of the spin-orbit part  $\Delta E_{\text{sp o}}$  can be calculated from our bandmodel for a given  $E_F$  using the bandparameters in table 7.1. The exchange part of the spin splitting is proportional to  $\langle S_B \rangle$

$$\Delta E_{\text{sp ex}} = J \times \langle S_B \rangle \quad (7.4)$$

where  $J$  represents the strength of the exchange interaction,  $\langle S_B \rangle$  is known from the magnetisation and  $x$  is the Mn concentration. The spin splitting  $\Delta E_{\text{sp}}$  divided by the Landau splitting  $\Delta E_L = \hbar e B/m^*$  can now be written as

$$\nu = \frac{\Delta E_{\text{sp o}}}{\hbar e B/m^*} + \frac{J \times \langle S_B \rangle}{\hbar e B/m^*} \quad (7.5)$$

Because the effective electron mass  $m^*$  can also be calculated from the bandmodel, the interaction strength  $J$  remains the only indetermined parameter in the right hand side of this expression.

For the  $\nu$ -value we only know, that in a node  $\nu = k + 1/2$ , with  $k$  being an integer value. The ambiguity in the  $k$ -value can be eliminated by fitting the measurements of the temperature dependence of the amplitude of the SdH oscillations to eq. 2.8. This is illustrated for the  $\text{Hg}_{0.975}\text{Mn}_{0.025}\text{Se}$  sample. For this sample the oscillation amplitude at a constant field of 1 T is plotted as a function of temperature in fig. 7.14. A node occurs for  $T = 1.8$  K. For this node we start with an estimated value for the integer  $k$ . Substitution of the resulting  $\nu$ -value in eq. 7.5 yields the corresponding value for the interaction strength  $J$ . In the high temperature node,  $k$  is increased by 1. The only temperature dependent quantity in eq. 7.5 is  $\langle S_B \rangle$ . Now we have to increase the temperature until  $\langle S_B \rangle$  reaches the value where eq. 7.5 is satisfied for the new  $\nu$ -value. This yields the temperature where the next node is expected. For  $\nu$  in the 1.8 K node chosen equal to  $-7/2$ ,  $-5/2$ ,  $-3/2$ , the high temperature node is expected for 3.8 K, 5.4 K and 19 K respectively. From fig. 7.14 it is clear that the next node occurs very close to 5.4 K. Thus we find that  $-5/2$  is the correct  $\nu$ -value for the node at 1.8 K. The solid curve in fig. 7.14 gives the temperature dependence of the amplitude of the first harmonic of the oscillations as calculated from eq. 2.8 under the conditions  $\nu = -5/2$  at 1.8 K.

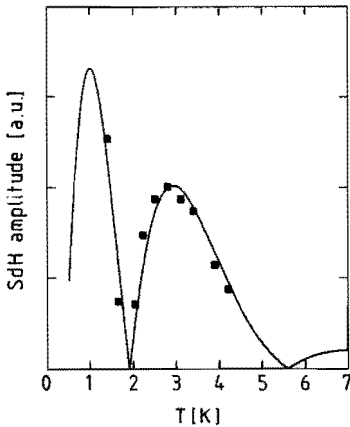


Fig. 7.14

Temperature dependence of the SdH oscillation amplitude for

$\text{Hg}_{0.975}\text{Mn}_{0.025}\text{Se}$  with  
 $n_e = 1.2 \cdot 10^{24} \text{ m}^{-3}$  at  $B = 1 \text{ T}$   
and  $B \parallel [110]$ .

The values of the exchange integrals  $\alpha$  and  $\beta$  can be obtained from the interaction strength  $J$ . Because the band electron wave functions are mixtures of  $s$  and  $p$ -symmetric wave functions, both  $\alpha$  and  $\beta$  contribute to  $J$

$$J = f_1 \alpha + f_2 \beta \quad (7.6)$$

$f_1$  and  $f_2$  depend only on the bandparameters and the Fermi energy, and can be calculated with the bandmodel. Using eq. 7.5, we can determine  $J$  from the experimental conditions where a node occurs. Thus eq. 7.6 becomes a relation in which  $\alpha$  and  $\beta$  are the only unknown parameters.

Repeating this procedure for a sample with different carrier density and corresponding different  $E_F$ , results in a second equation in  $\alpha$  and  $\beta$ . Solving these two independent equations yields the values for  $\alpha$  and  $\beta$ . In the case the samples have carrier densities in a narrow range, the coefficients of these equations do not differ very much, because  $f_1$  and  $f_2$  do not vary very rapidly with  $E_F$ . In that case a small inaccuracy in one of the coefficients can cause a large change in the values of  $\alpha$  and  $\beta$  determined from these equations.

Applying the procedure mentioned above on data collected for  $\text{Hg}_{0.975}\text{Mn}_{0.025}\text{Se}$ , we obtain the following values for the exchange integrals:  $\alpha = -0.8 \pm 0.3$  eV and  $\beta = 1.3 \pm 0.3$  eV. For  $\text{Hg}_{0.95}\text{Mn}_{0.05}\text{Se}$ , the data can be fit with the same values.

From our results we conclude that the exchange parameters are independent of the Mn composition. Before comparing these values to the values for other SMSC we first discuss the accuracy of the determination of  $\alpha$  and  $\beta$ , taking the case of  $\text{Hg}_{0.975}\text{Mn}_{0.025}\text{Se}$  as an example.

Inaccuracies in the determination of the field and temperature where the nodes occur enter the calculations via  $\langle S_B \rangle / B$  in eq. 7.5. The experimental error in the temperature measurement is less than 0.05 K for  $T > 2$  K; and less than 0.1 K for  $T < 2$  K. The field value can be given with an accuracy of  $\pm 0.05$  T. This leads to 1 percent uncertainty in  $\langle S_B \rangle / B$  for  $T > 2$  K and 2.5 percent for  $T < 2$  K. For the error ranges of the exchange integrals this results in 0.2 eV and 0.3 eV for  $T > 2$  K and  $T < 2$  K respectively.

The magnetisation enters the calculations via  $\langle S_B \rangle$ . The accuracy of values for  $\langle S_B \rangle$ , obtained by the interpolation of data from literature, would not have been better than 5 percent. A change of 5 percent in the value for  $\langle S_B \rangle$ , yields changes of 0.5 eV in the values of the exchange integrals. This demonstrates the need for a very precise determination of  $\langle S_B \rangle$ . Our magnetisation measurements give  $\langle S_B \rangle$  with 2 percent accuracy, yielding an error range of 0.2 eV for the exchange integrals.

The Mn composition enters the calculations both directly and via the composition dependence of the bandgap. Changing  $x$  from 0.025 to 0.0275 leads to changes in  $\alpha$  and  $\beta$  of 0.2 eV. The uncertainty in the concentration values for our samples is less than 2 percent, resulting in a negligible contribution to the error in  $\alpha$  and  $\beta$ .

The most serious errors in the values of  $\alpha$  and  $\beta$  are caused by neglecting the anisotropy of the bandstructure. To demonstrate this we also determined  $\alpha$  and  $\beta$  from data obtained for  $B \parallel [001]$ . In contrast to the case where  $B$  is oriented parallel to the  $[110]$ -axis, the inversion asymmetry contributes significantly to the spin splitting for  $B \parallel [001]$ . The values of  $\alpha$  and  $\beta$  obtained in this case are  $\alpha = -0.3 \pm 0.3$  eV and  $\beta = 1.1 \pm 0.3$  eV. All values of  $\alpha$  and  $\beta$  reported in literature are determined from experiments on unoriented samples [1-3]. Doing this one neglects the anisotropy of the bandstructure and the values of  $\alpha$  and  $\beta$  scatter over a large range  $-0.3 < \alpha < -0.9$  eV and  $0.7 < \beta < 1.5$  eV. This proves that the anisotropy of the bandstructure cannot be neglected in the determination of  $\alpha$  and  $\beta$ .

Notwithstanding the experimental inaccuracies, the values for the exchange integrals we determined for  $\text{Hg}_{1-x}\text{Mn}_x\text{Se}$ ,  $\alpha = -0.8$  eV and  $\beta = 1.3$  eV, follow the general trends for the exchange integrals in II-VI SMSC. The value of the exchange integral  $\alpha$  for electrons with an s-symmetric wave function yields a ferromagnetic interaction, whereas the value for the exchange integral  $\beta$ , for wave functions with p-symmetry, indicates an antiferromagnetic interaction. Furthermore our results show that  $|\beta| > |\alpha|$ . Also the tendency is followed that the ratio between  $|\beta|$  and  $|\alpha|$  is smaller for narrow-gap SMSC than for wide-gap SMSC (see table 7.5).

Table 7.5. Exchange integrals for some II-VI compounds

	$ \alpha $ [eV]	$ \beta $ [eV]	$\beta/\alpha$	ref.
ZnMnSe	0.29	1.4	4.8	[16]
ZnMnTe	0.20	1.1	5.5	[16]
CdMnSe	0.23	1.26	5.5	[16]
CdMnTe	0.22	0.88	4.0	[16]
HgMnSe	0.8	1.3	1.6	our work
HgMnSe	0.3-0.9	0.7-1.5	1.6-2.3	[16]
HgMnTe	0.4-0.7	0.6-1.4	1.5-2.0	[16]
MnSe	0.33	1.05	3.2	[17]
MnTe	0.33	1.35	4.1	[17]

The values of  $\alpha$  and  $\beta$  for MnSe and MnTe, obtained from spin polarised band calculations, are the only theoretical values available until now [17]. The calculations were performed assuming that MnSe and MnTe are wide-gap ferromagnetic semiconductors with zinc blende structure. Apparently these theoretical values agree only with the experimental results for wide-gap SMSC and not for narrow-gap SMSC. This is related to the origin of the exchange interaction as qualitatively discussed by Bhattacharjee et al. [18]. According to Bhattacharjee et al. two mechanisms contribute to the exchange interaction constants

- i) The normal exchange mechanism originating from the interaction potential between band electrons and d-electrons.
- ii) The additional mechanism due to hybridisation of the wave functions for the band electrons and the d-electrons, in the case the d-levels are located in one of the bands.

The first contribution is independent of the symmetry of the bands and will therefore be approximately the same for  $\alpha$  and  $\beta$ . The second contribution depends strongly on the symmetry of the bands. The d-levels are located in the valence bands. For wide-gap SMSC the valence band states are constructed of p-symmetric wave functions. Therefore the hybridisation contribution affects in wide-gap SMSC only the value for  $\beta$ , resulting in a large difference of the values for  $\alpha$  and  $\beta$ . In narrow-gap SMSC the band states of both the conduction band and the valence band, are constructed of mixtures of s and p-type wave functions. The d-levels for  $\text{Hg}_{1-x}\text{Mn}_x\text{Se}$  are again located in the valence

band [19]. This result also holds for  $\text{Hg}_{1-x}\text{Mn}_x\text{Te}$  [20]. Hybridisation of d-states with the valence band involves both s and p-symmetric wave functions, resulting in additional contributions to both  $\alpha$  and  $\beta$ . This explains qualitatively the difference in exchange integrals obtained for wide-gap and narrow-gap SMSC.

### 7.3.4 Inversion asymmetry

#### HgSe

We start with the determination of the inversion asymmetry parameters for pure HgSe, because only the spin-orbit interaction and the inversion asymmetry contribute to the spin splitting for this material. This reduces the number of parameters describing the spin splitting. The inversion asymmetry part of the spin splitting is described by three parameters:  $C$ ,  $G$  and  $N_2=N_3$ .

Like the exchange interaction parameters in the previous section, also the inversion asymmetry parameters are determined from the spin splitting nodes in the SdH amplitude. In addition to our data also data published by Seiler et al. [12] are used in our analysis. The procedure to determine the values of the inversion asymmetry parameters from the nodes is illustrated in fig. 7.15. This figure gives

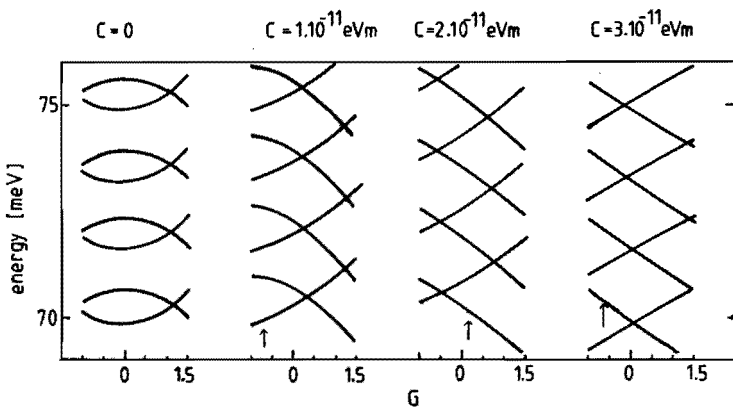


Fig. 7.15 Energy levels of the conduction band of HgSe, as a function of the inversion asymmetry parameters. Further explanation is given in the text.

the energy levels of the electrons near the Fermi energy calculated for the field strength and orientation where a given node occurs in the experiments. The bandparameters used in this calculation are listed in table 7.1. The inversion asymmetry parameters are adjusted in order to fulfil the conditions for a node to occur: the ratio  $\nu$  between spin splitting and Landau splitting equals  $1/2$ . In fig. 7.15  $N_2=N_3$  is kept equal to zero. In the left part of fig. 7.15  $C = 0$  and  $G$  is varied from  $-1$  to  $+1.5$ . In this range the condition  $\nu = 1/2$  cannot be satisfied. For the other  $C$ -values in the figure  $G$  is varied over the same range. The arrows mark the position where  $\nu = 1/2$ . The collection of  $C, G$ -combinations, where this relation is fulfilled, leads to a curve in the  $C, G$ -plane. If this procedure is repeated for different values of  $N_2=N_3$  one obtains a surface in the three dimensional  $C, G, N_2=N_3$ -space.

The analysis of nodes for other orientations of this sample and for samples with different carrier densities yields other surfaces in the  $C, G, N_2=N_3$ -space. In principle it should be possible to find from the intersection of these surfaces one unique set of values for  $C, G$  and  $N_2=N_3$ , fitting the data obtained for all orientations and for all carrier densities. However, as we have seen in chapter 4, the shape of the anisotropy for the inversion asymmetry part of the spin splitting is almost the same for each of the three parameters (fig. 4.2). Therefore the analysis of the orientation dependence of the nodes is not a very sensitive method to distinguish between the influence of each of the inversion asymmetry parameters (the surfaces in  $C, G, N_2=N_3$ -space corresponding to the different orientations coincide).

In principle only the different  $k$ -vector dependence of the matrix elements corresponding to the different inversion asymmetry parameters allows to determine the values of these parameters independently. Fig. 7.16 shows the  $k$ -dependence of the splitting of the conduction band of HgSe in the absence of a magnetic field for the different inversion asymmetry parameters. The splitting is calculated using the  $8 \times 8$  Hamiltonian matrix in table 3.1. The  $k$ -vector is chosen parallel to the  $[110]$ -axis.

One cannot distinguish between the influence on the splitting due to  $G$  and  $N_2=N_3$ , because the corresponding matrix elements vary both quadratically with  $k$ . This implies in reverse that there is no need

for a refinement in the description of the inversion asymmetry by the parameter  $N_2=N_3$ . Therefore we concentrate on C and G and keep  $N_2=N_3$  equal to zero. However, even though the splittings due to C and G have a different  $k$ -dependence (fig. 7.16), the  $k$ -dependence cannot be used to determine the parameter values independently: experimental data are

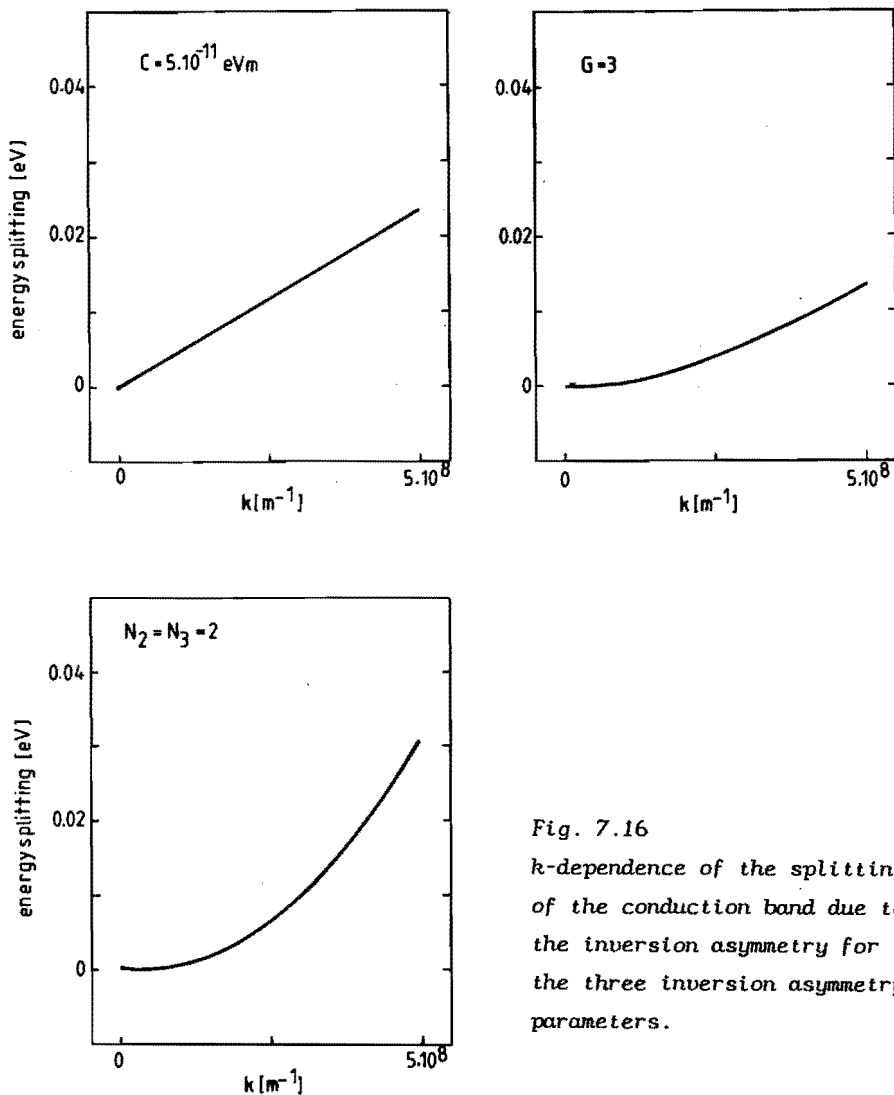


Fig. 7.16  
*k*-dependence of the splitting of the conduction band due to the inversion asymmetry for the three inversion asymmetry parameters.

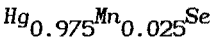


available only for carrier densities between  $0.5 \cdot 10^{24} \text{ m}^{-3}$  and  $4.0 \cdot 10^{24} \text{ m}^{-3}$ . This corresponds to the k-vector range from  $2.5 \cdot 10^8 \text{ m}^{-1}$  to  $5.0 \cdot 10^8 \text{ m}^{-1}$ . In this range the quadratic increase of the splitting with increasing k can hardly be distinguished from a linear increase of the splitting (fig. 7.16).

Because we cannot give one single set of values for C and G, we summarise our results in the relation

$$C = (2.5 \pm 0.3) \cdot 10^{-11} \text{ eVm} - G (1.6 \pm 0.3) \cdot 10^{-11} \text{ eVm} \quad (7.7)$$

We cannot determine the values of the inversion asymmetry parameters separately, because they cause a similar behaviour of the spin splitting. The other way around, only one of the parameters is sufficient to describe the inversion asymmetry. For this "effective" parameter we choose C, because the addition of terms linear in k is the simplest and therefore the most obvious way to include the inversion asymmetry in the Hamiltonian.



For the determination of the effective inversion asymmetry parameter C for  $\text{Hg}_{0.975}\text{Mn}_{0.025}\text{Se}$  we use the nodal field positions measured for the sample with  $n_e = 1.2 \cdot 10^{24} \text{ m}^{-3}$  at 2.03 K. From the determination of the exchange integrals  $\alpha$  and  $\beta$  we know that the  $\nu$ -value for these nodes equals -2.5. The procedure to determine C is shown in fig. 7.17. This figure shows the spin split energy levels of the conduction band near the Fermi energy for three magnetic field orientations. The spin levels belonging to the Landau level closest to the Fermi energy are given by the solid curves. For each field orientation we start on the left with the energy levels without exchange interaction and without inversion asymmetry. Then we increase  $\alpha$  to -0.8 eV and afterwards  $\beta$  to 1.3 eV, the values obtained in section 7.3.3. We now obtain the energy levels in the presence of exchange interaction but still without inversion asymmetry. Finally the inversion asymmetry parameter C is increased from 0 to  $5.0 \cdot 10^{-11} \text{ eVm}$ . The nodes occur when the spin splitting equals 2.5 times the Landau splitting. This way we can determine the value of C, resulting in  $C = 2.4 \cdot 10^{-11} \text{ eVm}$  in the  $B \parallel [001]$  orientation and  $C = 2.3 \cdot 10^{-11} \text{ eVm}$  for  $B \parallel [111]$ . As we

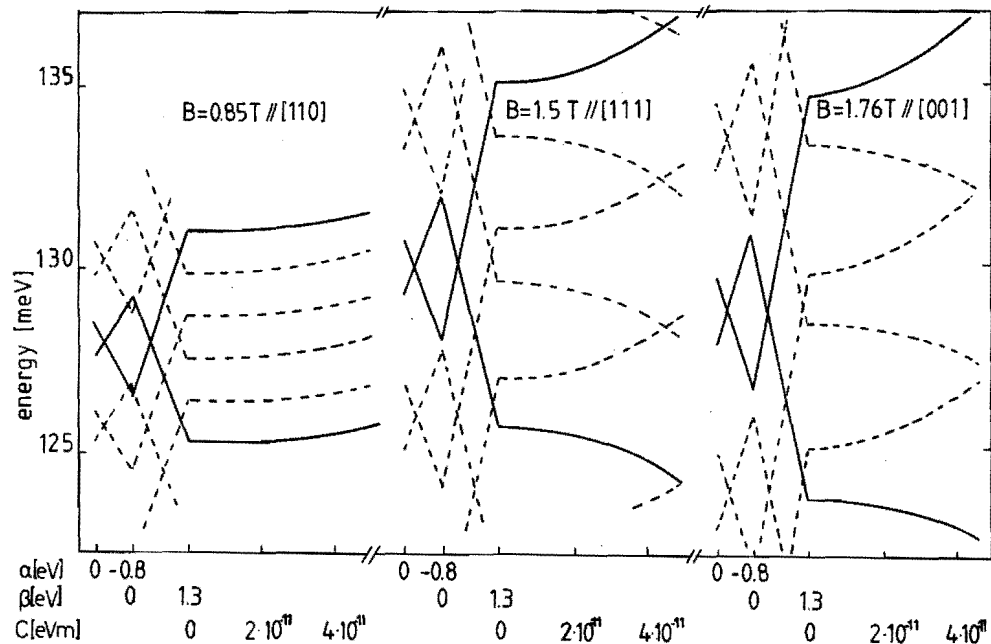


Fig. 7.17 Energy levels of the conduction band for three magnetic field orientations, calculated for  $\text{Hg}_{0.975}\text{Mn}_{0.025}\text{Se}$  for  $\alpha = -0.8$  eV and  $\beta = 1.3$  eV and  $C$  increasing from 0 to  $5.0 \cdot 10^{-11}$  eVm. Further explanation is given in the text.

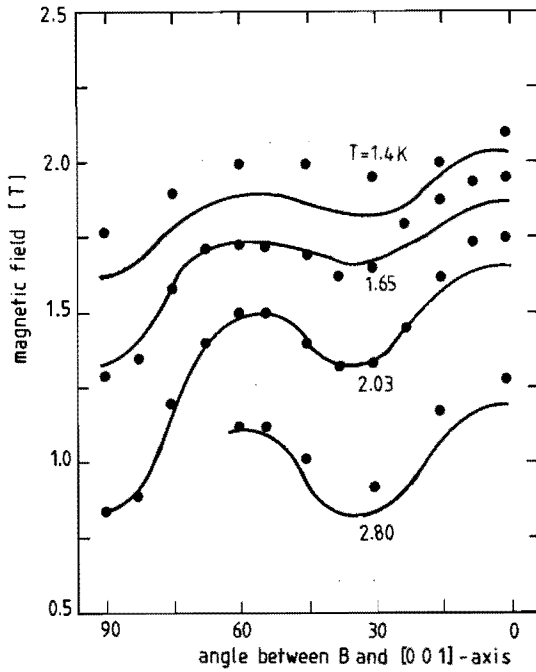
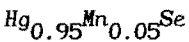


Fig. 7.18

Angular dependence of the nodes for  $\text{Hg}_{0.975}\text{Mn}_{0.025}\text{Se}$  with  $n_e = 1.2 \cdot 10^{24} \text{ m}^{-3}$ . The solid curves are calculated using  $\alpha = -0.8 \text{ eV}$ ,  $\beta = 1.3 \text{ eV}$  and  $C = 2.3 \cdot 10^{-11} \text{ eVm}$ . The dots represent the measurements.

expected for the  $B \parallel [110]$  orientation, the splitting remains constant when  $C$  increases. Only a slight shift of the levels is observed.

Choosing  $C$  equal to  $2.3 \cdot 10^{-11} \text{ eVm}$  we can now calculate for the first time the complete angular dependence of the nodal positions in the SdH amplitude. In fig. 7.18 we compare the calculated positions (solid curves) to the experimental data shown in fig. 7.8b. The agreement of the angular dependence is very good. The experimentally observed decrease of the anisotropy of the nodal positions with increasing magnetic field is very well reproduced by our calculations.



For  $\text{Hg}_{0.95}\text{Mn}_{0.05}\text{Se}$  we followed the same procedure for the determination of the parameter  $C$  as we used for  $\text{Hg}_{0.975}\text{Mn}_{0.025}\text{Se}$ . This is shown in fig. 7.19 for the sample with  $n_e = 2.07 \cdot 10^{24} \text{ m}^{-3}$ . We use the same exchange integral values as in the case of  $\text{Hg}_{0.975}\text{Mn}_{0.025}\text{Se}$ . The value obtained for  $C$  is  $1.0 \cdot 10^{-11} \text{ eVm}$ .

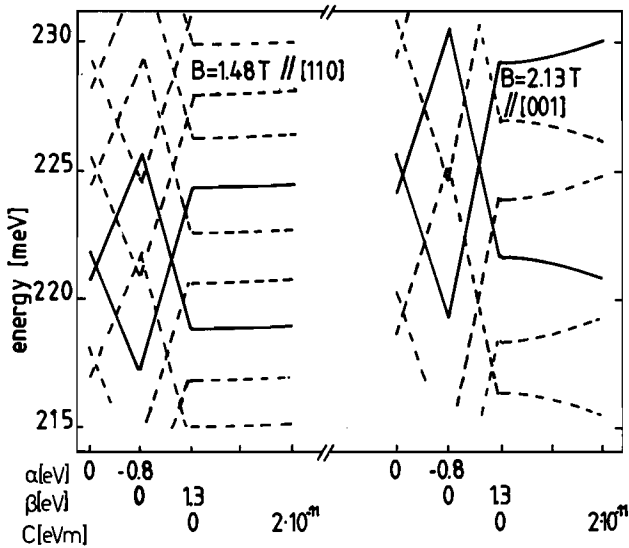


Fig. 7.19 Energy levels of the conduction band for two magnetic field orientations, calculated for  $\text{Hg}_{0.95}\text{Mn}_{0.05}\text{Se}$  for  $\alpha = -0.8$  eV and  $\beta = 1.3$  eV and  $C$  increasing from 0 to  $2.0 \cdot 10^{-11}$  eVm. Further explanation is given in the text.

With our bandmodel we can only calculate the energy levels for magnetic field orientations in the (110)-plane. Because the measurements for this sample were done in configuration 2, the experimental data can be fit only for the two field orientations given in fig. 7.19 and a complete calculation of the angular dependence of the nodes cannot be given for this sample.

#### Discussion

We have clearly demonstrated for the  $x = 0.025$  sample that our new bandmodel can fit the anisotropy and the temperature dependence of the nodes in the SdH amplitude using only one effective inversion asymmetry parameter. The value of this parameter is not consistent for different Mn concentrations: the  $C$  value of  $2.3 \pm 0.1 \cdot 10^{-11}$  eVm for  $x = 0.025$  agrees very well with the  $C, G$ -relation derived for HgSe. The value of  $C = 1.0 \cdot 10^{-11}$  eVm obtained for  $x = 0.05$  does not fulfil this relation.

The large decrease of the effective inversion asymmetry parameter  $C$ , when changing  $x$  from 0.025 to 0.05 is surprising because the values of the inversion asymmetry parameters  $C$ ,  $G$  and  $N_2=N_3$  are mainly determined by interaction with higher bands. As already mentioned in the discussion of the higher band parameters describing the warping, the energy distances to the higher bands change only weakly due to the admixture of Mn in the lattice. Consequently also the interactions with these higher bands should be insensitive to variation of the Mn concentration. Therefore the effective value of  $C$ , including the effects of all the three inversion asymmetry parameters, is expected to be constant for all Mn concentrations. Nevertheless, we found experimentally that the addition of Mn influences the inversion asymmetry effects (compare the results for  $x = 0.025$  and  $x = 0.05$ ).

Therefore we estimated the variation of the inversion asymmetry part of the spin splitting due to the change of the bandgap with Mn concentration. For fixed values of the inversion asymmetry parameters  $C$ ,  $G$  and  $N_2=N_3$  we calculated the splitting of the bands as a function of the bandgap. For a constant  $k$ -vector value the splitting due to  $G$  and to  $N_2=N_3$  turned out to be insensitive to variation of the bandgap. The splitting due to  $C$  decreases by 10 percent when the bandgap is changed from  $-0.27$  eV ( $x = 0$ ) to  $-0.16$  eV ( $x = 0.025$ ), and another 10 percent for a further change of  $E_g$  to  $-0.05$  eV ( $x = 0.05$ ).

One can possibly explain the observed splitting for  $x = 0.025$  and  $x = 0.05$  by assuming that apart from  $C$ , also  $G$  contributes to the spin splitting and that both contributions partly compensate each other. The compensation changes with Mn concentration because the contribution originating from  $C$  depends on the bandgap. The estimated values of  $C$  and  $G$ , fitting the results for both Mn concentrations, are:  $C = 9.0 \cdot 10^{-11}$  eV $\cdot$ m and  $G = -8$ . These values are very large compared to the other results and do not fit to the  $C, G$ -relation obtained for HgSe. Therefore this set of values is unacceptable.

We cannot compare our results to other values determined for  $\text{Hg}_{1-x}\text{Mn}_x\text{Se}$ , because no values are published in literature so far. Even for the host material HgSe, very little is known on the numerical values of the inversion asymmetry parameters. Witowski [21] determined values for  $C$  and  $G$  from magneto-optical experiments. The parameters are obtained from the analysis of the relative strengths of observed

resonances corresponding to different optical transitions as a function of the crystal orientation. Witowski obtains two sets of values: one for C and G with opposite signs ( $C = 1.1 \cdot 10^{-11}$  eVm and  $G = -0.3$ ) and another one for C and G with equal signs ( $C = 7.0 \cdot 10^{-11}$  eVm and  $G = 60$ ). The values with opposite signs are the closest to the C,G-combinations satisfying eq. 7.7.

A theoretical estimate of the parameters is only given for C. Cardona et al. [22] determined the value for C independently of the other inversion asymmetry parameters. The resulting value is  $0.8 \cdot 10^{-11}$  eVm.

Considering the scatter in the reported values of inversion asymmetry parameters for the  $\text{Hg}_{1-x}\text{Mn}_x\text{Se-HgSe}$  system, we have to keep in mind that even for InSb, the narrow-gap semiconductor which is most widely investigated, no consistent set of inversion asymmetry parameters is available. Weiler et al. [23] found that data on absorption coefficients observed in experiments can be fit with three different sets of parameters:  $C = -3.0 \cdot 10^{-11}$  eVm,  $G = -0.21$ ,  $N_2=N_3 = 0.61$ ;  $C = -3.0 \cdot 10^{-12}$  eVm,  $G = -3$ ,  $N_2=N_3 = -1$ , and  $C = 3.0 \cdot 10^{-11}$  eVm,  $G = -0.9$ ,  $N_2=N_3 = -0.4$ . The values vary over more than one order of magnitude and even change their signs. Also the values for C determined experimentally by Pidgeon and Groves [24] and Bell and Rodgers [5] show a similar scatter.

### Conclusion

Although we cannot give a consistent set of inversion asymmetry parameters for the  $\text{Hg}_{1-x}\text{Mn}_x\text{Se-HgSe}$  system, we have shown in this section that the inversion asymmetry is indeed responsible for the strong anisotropy of the nodal field positions.

### 7.3.5 Zero-field spin splitting

According to the theory of exchange interaction used in the preceding parts of this chapter the exchange contribution to the spin splitting is proportional to the macroscopic magnetisation [26]. Thus the exchange part of the spin splitting should vanish in the absence of a magnetic field. Contrary to this theoretical expectation, some

observations of a finite spin level splitting at zero magnetic field are reported. The size of this zero-field splitting amounts up to a few meV: 0.4 meV in  $\text{Pb}_{0.99}\text{Mn}_{0.01}\text{Te}$  [27], 1.25 meV per percent of Mn in  $\text{Pb}_{1-x}\text{Mn}_x\text{S}$  [28], 7.5 meV in  $\text{Hg}_{0.91}\text{Mn}_{0.09}\text{Te}$  [29], 0.72 meV in  $\text{Hg}_{0.98}\text{Mn}_{0.02}\text{Se}$  and 1.82 meV in  $\text{Hg}_{0.96}\text{Mn}_{0.04}\text{Se}$  [9].

In all these experiments, except in the case of  $\text{Pb}_{1-x}\text{Mn}_x\text{S}$ , the influence of the zero-field splitting was determined from extrapolations of the spin splitting to the zero-field case. Since these experiments prove that the effects of a finite zero-field splitting can still be present in an external magnetic field, we may expect that the zero-field splitting will also affect our SdH measurements.

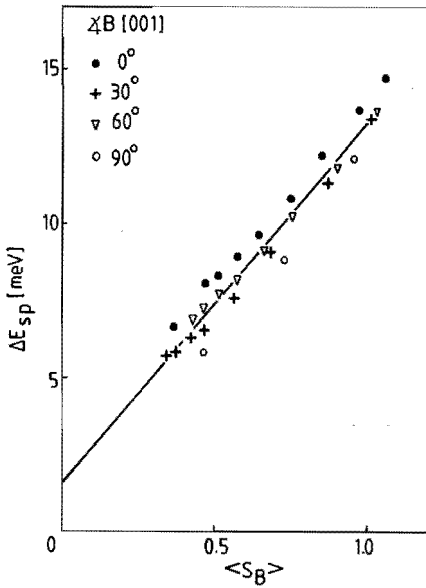


Fig. 7.20 Total spin splitting for  $\text{Hg}_{0.975}\text{Mn}_{0.025}\text{Se}$  with  $n_e = 1.2 \cdot 10^{24} \text{ m}^{-3}$ , determined from the nodes.  $\langle S_B \rangle$  is calculated for the  $B, T$ -combinations where the nodes occur. Different symbols represent the different field orientations for which the data were obtained.

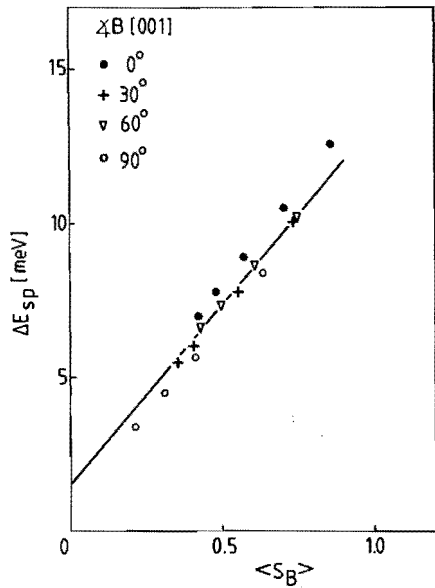


Fig. 7.21 Same as for fig. 7.20 except  $n_e = 7.4 \cdot 10^{24} \text{ m}^{-3}$ .

In our search for possible effects of zero-field splitting in  $\text{Hg}_{1-x}\text{Mn}_x\text{Se}$  we use the data for  $x = 0.025$ . Of all our samples, the most complete set of data on nodal field positions was obtained for this sample. For these nodes we determined the value of the spin splitting  $\Delta E_{\text{sp}}$ . In figs. 7.20 and 7.21,  $\Delta E_{\text{sp}}$  is plotted versus  $\langle S_B \rangle$ .  $\langle S_B \rangle$  is determined from the magnetisation data for the fields and temperatures where the nodes occur. Figs. 7.20 and 7.21 give the data for the samples with  $n_e = 1.2 \cdot 10^{24} \text{ m}^{-3}$  and  $7.4 \cdot 10^{23} \text{ m}^{-3}$  respectively. The different symbols represent the different orientations of the magnetic field. The splitting at zero field is found by linear extrapolation of these data to  $\langle S_B \rangle = 0$  (i.e.  $B = 0 \text{ T}$ ). For both carrier densities we find a zero-field splitting of 1.5 meV. This value is of the same

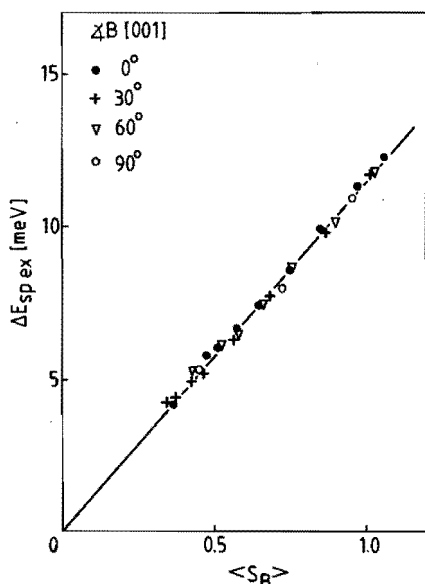


Fig. 7.22 Exchange part of the spin splitting for  $\text{Hg}_{0.975}\text{Mn}_{0.025}\text{Se}$  with  $n_e = 1.2 \cdot 10^{24} \text{ m}^{-3}$ , obtained by subtraction of the spin-orbit spin splitting and the inversion asymmetry splitting from the total spin splitting in fig. 7.20. The solid line represents the theoretical exchange splitting without zero-field splitting.

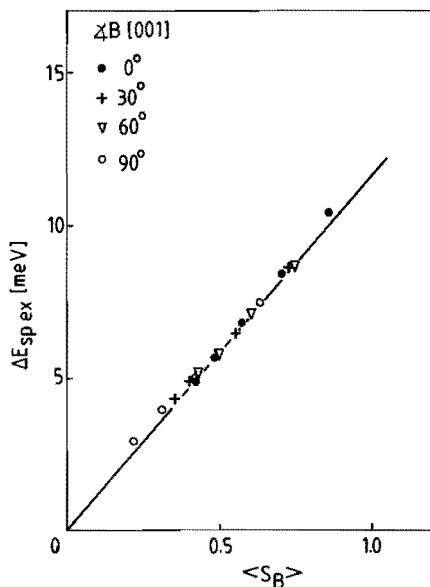


Fig. 7.23 Same as for fig. 7.21 except  $n_e = 7.4 \cdot 10^{23} \text{ m}^{-3}$ .



order of magnitude as the values reported in refs. [9,26-28]. These authors attribute the zero-field splitting completely to the exchange interaction. The inversion asymmetry, however, can cause a splitting of the bands at zero field as well. To obtain purely the exchange part of the spin splitting ( $\Delta E_{sp\ ex}$ ) we subtract the contributions of the spin-orbit interaction ( $\Delta E_{sp\ o}$ ) and the inversion asymmetry ( $\Delta E_{sp\ ia}$ ) according to eq. 2.9.  $\Delta E_{sp\ ia}$  was calculated using  $C = 2.3 \cdot 10^{-11}$  eV $\cdot$ m for the effective inversion asymmetry parameter as obtained for this sample. The resulting  $\Delta E_{sp\ ex}$  values are plotted versus  $\langle S_B \rangle$  in figs. 7.22 and 7.23. Note that after subtraction of  $\Delta E_{sp\ o}$  and  $\Delta E_{sp\ ia}$  the splitting does not depend on the field orientation anymore.

For  $\langle S_B \rangle$  values above 0.5 the experimental values of  $\Delta E_{sp\ ex}$  deviate only negligibly from the relation  $\Delta E_{sp\ ex} = J \times \langle S_B \rangle$ , given by the solid lines in fig. 7.22 and 7.23. This relation was used to determine the exchange integrals  $\alpha$  and  $\beta$  in section 7.3.2. Therefore we conclude that even if a finite splitting exists at zero field, it does not affect the obtained values for  $\alpha$  and  $\beta$ .

From a linear extrapolation of  $\Delta E_{sp\ ex}$  to  $\langle S_B \rangle = 0$  in figs. 7.22 and 7.23 we find much smaller zero-field splitting energies: 0.20 meV and 0.27 meV for  $n_e = 1.2 \cdot 10^{24} \text{ m}^{-3}$  and  $7.4 \cdot 10^{23} \text{ m}^{-3}$  respectively. This indicates that the effects of inversion asymmetry must be taken into account in the determination of zero-field splitting energies.

Staguhn [9] neglected the inversion asymmetry and found a zero-field splitting of 0.72 meV for a  $\text{Hg}_{1-x}\text{Mn}_x\text{Se}$  sample with nearly the same Mn concentration as our sample ( $x = 0.02$ ) and  $n_e = 6.0 \cdot 10^{22} \text{ m}^{-3}$ . However, the contribution of the inversion asymmetry to the spin splitting is only very small for the low carrier density of the sample of Staguhn. Furthermore the increase of the zero-field splitting with increasing Mn concentration (1.82 meV for  $x = 0.04$  and  $n_e = 6.0 \cdot 10^{22} \text{ m}^{-3}$  [9]) proves that the splitting observed by Staguhn cannot be attributed to the inversion asymmetry alone.

The values for the zero-field splitting obtained from figs. 7.22 and 7.23 come very close to the accuracy of the values for  $\Delta E_{sp\ ex}$ . Therefore these results do not give clear evidence for the existence of zero-field splitting in our samples.

From this section we conclude that if zero-field splitting exists for our samples, it is very small. The most important conclusion is, that a possible zero-field splitting does not influence the spin splitting energies from which we determined the exchange integrals  $\alpha$  and  $\beta$ , and therefore it is justified to neglect the zero-field splitting in the determination of  $\alpha$  and  $\beta$ .

#### REFERENCES

- [1] S. Takeyama, R.R. Gałazka, Phys. Stat. Sol. (b) 96, 413 (1979).
- [2] P. Byszewski, M.Z. Cieplak, A. Mongird-Corska, J.Phys.C., Sol. St. Phys 13, 5383 (1980).
- [3] M. Dobrowolska, W. Dobrowolski, R.R. Gałazka, A Mycielski, Phys. Stat. Sol. (b) 105, 477 (1981).
- [4] R.R. Gałazka, W. Dobrowolski, J.C. Thuillier, Phys. Stat. Sol. (b) 98, 97 (1980).
- [5] A. Witowski, K. Pastor, J.K. Furdyna, Phys. Rev. B 26, 931 (1982)
- [6] Y. Guldner, C. Rigaux, M. Dobrowolska, A. Mycielski, W. Dobrowolski, Proc. Int. Conf. Phys. Narrow-Gap Semicond. Warsaw 1977 (Polish Scient. Publ., Warsaw 1978) p. 87.
- [7] W. Szuskiewicz, Phys. Stat. Sol. (b) 91, 361 (1979).
- [8] P. Byszewski, A. Mongird-Corska, A.M. Sandauer, Proc. Conf. Physics of Semicond., Jaszowiec 1980, p. 245.

- [9] W. Staguhn, Ph.D. Thesis, Julius Maximilians Universität, Würzburg (1984).
- [10] W. Dobrowolski, M. v. Ortenberg, A.M. Sandauer, R.R. Gałazka, A. Mycielski, R. Pauthenet, in Lecture notes on Physics no 152 (Springer Verlag, Berlin, 1982) p. 302.
- [11] C.R. Whitsett, Phys. Rev. 138, A829 (1965).
- [12] D.G. Seiler, R.R. Gałazka, W.M. Becker, Phys.Rev. B 3, 4274 (1971).
- [13] L.M. Roth, S.H. Groves, P.W. Wyatt, Phys. Rev. Lett. 19, 576 (1967).
- [14] L.M. Roth, Phys. Rev. 173, 755 (1968)
- [15] M. Jaczynski, J. Kossut, R.R. Gałazka, Phys. Stat. Sol. (b) 88, 73 (1978)
- [16] A. Twardowski, T. Dietl, M. Demianiuk, Sol. St. Comm. 48, 845 (1983).
- [17] K.C. Hass, B.E. Larson, H. Ehrenreich, A.E. Carlson, Journ. Magn. Magn. Mat. 54-57, 1283 (1986).
- [18] A.K. Bhattacharjee, G. Fishman, B. Coqblin, Physica 117B&118B, 449 (1983).
- [19] A. Franciosi, C. Caprile, R. Reifenberger, Phys. Rev. B 31, 8061 (1985).
- [20] K.C. Hass, H. Ehrenreich, J. Vac. Sci. Technol. A1, 1678 (1983).
- [21] A. Witowski, private communication (april 1986).
- [22] M. Cardona, N.E. Christensen, G. Fasol, Phys. Rev. Lett. 56, 2831 (1986).
- [23] M.H. Weiler, R.L. Aggarwal, B. Lax, Phys. Rev. B 17, 3269 (1978).
- [24] C.R. Pidgeon, S.H. Groves, Phys. Rev. 186, 824 (1969).
- [25] R.L. Bell, K.T. Rodgers, Phys. Rev. 152, 746 (1966).
- [26] J. Kossut, Phys. Stat. Sol. (b) 72, 359 (1975).
- [27] H. Pascher, E.J. Fantner, G. Bauer, W. Zawadzki, M. von Ortenberg, Sol. St. Comm. 48, 461 (1983).
- [28] G. Karczewski, L. Kowalczyk, Sol. St. Comm. 48, 653 (1983).
- [29] R. Stepniewski, Sol. St. Comm. 58, 19 (1986).

## CHAPTER VIII EXPERIMENTAL RESULTS ON $(\text{Cd}_{1-x}\text{Mn}_x)_3\text{As}_2$ AND THEIR INTERPRETATION.

This chapter gives the experimental results on  $(\text{Cd}_{1-x}\text{Mn}_x)_3\text{As}_2$  and their interpretation. The first section discusses the bandparameters used for the interpretation of the data. The second section deals with the results of the magnetisation measurements. The SdH data are presented and discussed in the last section. Special attention is paid to the small anisotropy of the bandstructure and to the determination of exchange integrals  $\alpha$  and  $\beta$ .

### 8.1 Bandparameters

For the  $(\text{Cd}_{1-x}\text{Mn}_x)_3\text{As}_2$ - $\text{Cd}_3\text{As}_2$  system we follow the same approach as for the  $\text{Hg}_{1-x}\text{Mn}_x\text{Se}$ - $\text{HgSe}$  system. For the interpretation of the data of the semimagnetic compound, we use a set of bandparameters based on the parameters of the host material.

Also in  $(\text{Cd}_{1-x}\text{Mn}_x)_3\text{As}_2$  the energy bandgap depends on the composition. Until now, no relation between the bandgap and the Mn concentration has been published. Therefore we have to use an estimate for this relation. As pointed out by Verié [1], the bandgap of narrow-gap semiconductors follows an empirical rule. The bandgap energy decreases with increasing mean atomic number  $Z$ . The bandgap values of some tetragonal II-V compounds with similar crystal structures are plotted in fig. 8.1. In the first approach the relation between the bandgap and the mean atomic number is taken linear. Now from this linear relation we can obtain an estimate of the bandgap energy of the hypothetical  $\text{Mn}_3\text{As}_2$  compound with a tetragonal crystal structure. For the mean atomic mass 28.3 of  $\text{Mn}_3\text{As}_2$  a bandgap of 1.36 eV is obtained. We assume a linear increase of the bandgap with increasing  $x$ , as in other mixed crystals [2]. Thus we obtain the following  $E_g(x)$  relation for  $(\text{Cd}_{1-x}\text{Mn}_x)_3\text{As}_2$

$$E_g(x) = -0.095 \text{ eV} + x \cdot 1.45 \text{ eV} \quad (8.1)$$

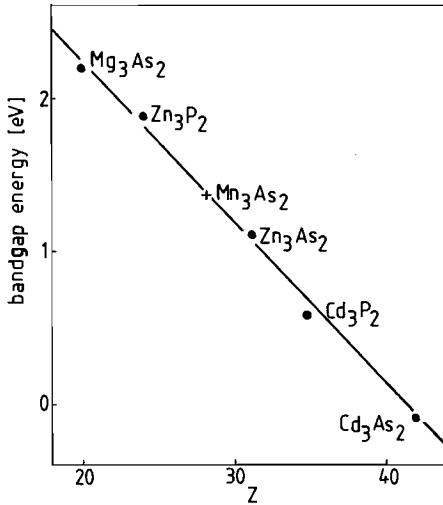


Fig. 8.1  
Bandgap energy versus mean atomic number  $Z$  for tetragonal II-V compounds.

The scarce data on the bandgap of  $(\text{Cd}_{1-x}\text{Mn}_x)_3\text{As}_2$  agree quite well with this relation. Neve [3] obtains  $E_g = -0.077$  eV and  $-0.060$  eV for  $x = 0.01$  and  $0.02$  respectively. The best fit of the bandgap energy obtained by Lubczynski et al. [4] for a sample with  $x = 0.083$ , is  $0.045$  eV.

The other bandparameters used in the interpretation of our data on  $(\text{Cd}_{1-x}\text{Mn}_x)_3\text{As}_2$  are based on the values for  $\text{Cd}_3\text{As}_2$  [5]. The values of the momentum matrix elements are  $P_{//} = 7.21 \cdot 10^{-10}$  eVm and  $P_{\perp} = 7.43 \cdot 10^{-10}$  eVm. The spin-orbit split off energy  $\Delta_{\text{so}}$  equals  $0.27$  eV. The crystal field splitting parameter  $\delta$ , which is characteristic for the tetragonal distortion of the lattice, equals  $0.085$  eV for  $\text{Cd}_3\text{As}_2$ .

Our experimental data show that the tetragonal distortion decreases with increasing Mn concentration. This means that the difference  $P_{//} - P_{\perp}$  and the parameter  $\delta$  depend on the Mn composition.

## 8.2 Magnetisation

The importance of having very accurate data on the magnetisation of the samples has already been discussed in the previous chapter. Magnetisation measurements were done for 7  $(\text{Cd}_{1-x}\text{Mn}_x)_3\text{As}_2$  samples in the temperature range from 1.5 to 4.2 K in fields up to 5 T. Fig. 8.2 shows the magnetisation of sample 1/4 CMA 3B for several temperatures. The solid curves are fits with the modified Brillouin function (eq. 3.7). The fit parameters  $S_o$  and  $T_o$  determined for this and all other samples are given in table 8.1. The  $S_o$  and  $T_o$  values of each sample show a monotonic temperature dependence. In the small temperature range in which the measurements were performed, the dependence of  $S_o$  and  $T_o$  can be linearised:  $S_o = S_{oo} + S_{o1} T$  and  $T_o = T_{oo} + T_{o1} T$ . The coefficients  $S_{oo}$ ,  $S_{o1}$ ,  $T_{oo}$  and  $T_{o1}$  are given in table 8.2.

The data in tables 8.1 and 8.2 follow the trend of a decreasing value of  $S_o$  and an increasing value of  $T_o$  with increasing Mn concentration. These changes reflect the increasing effects of the interaction between the Mn spins with increasing Mn content.

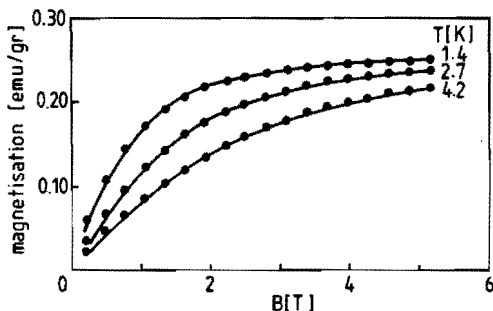


Fig. 8.2

The magnetisation of  $(\text{Cd}_{1-x}\text{Mn}_x)_3\text{As}_2$ ,  $x = 0.0075$  for different temperatures. The curves are fits with the modified Brillouin function.

Table 8.2 Coefficients for the linear temperature dependence of  $S_o$  and  $T_o$

X	sample	$S_{oo}$	$S_{o1}$	$T_{oo}$	$T_{o1}$
0.0023	0,25CMA3B	1.65	-0.17	0.26	0.003
0.0059	0.50CMA4B	1.61	0.18	1.17	0.14
0.0069	0,75CMA2	1.59	0.02	1.43	0.19
0.0105	1CMA7B	1.44	0.05	1.95	0.35
0.017	1.5CMA	1.25	0.05	3.22	0.40
0.0165	2CMA11	1.29	0.04	3.04	0.31
0.032	4CMA5	0.95	0.06	4.96	0.60

Table 8.1 Best fit parameters  $S_o$  and  $T_o$  for  $(Cd_{1-x}Mn_x)_3As_2$  magnetisation data:

1/4 CMA 3B, $x = 0.0023$		
T	$S_o$	$T_o$
1.5	1.61	0.27
2.02	1.61	0.33
2.70	1.61	0.39
3.47	1.59	0.40
4.2	1.57	0.36

3/2 CMA, $x = 0.017$		
T	$S_o$	$T_o$
1.5	1.32	3.81
2.01	1.35	3.98
2.72	1.40	4.39
3.49	1.43	4.55
4.22	1.46	4.9

1/2 CMA 4B, $x = 0.0059$		
T	$S_o$	$T_o$
1.5	1.62	1.32
2.02	1.65	1.45
2.67	1.68	1.72
3.47	1.67	1.60
4.20	1.68	1.75

2 CMA 11 $x = 0.0165$		
T	$S_o$	$T_o$
1.5	1.35	3.52
2.05	1.39	3.73
2.70	1.41	3.87
3.49	1.43	3.99
4.2	1.48	4.46

3/4 CMA 2, $x = 0.0069$		
T	$S_o$	$T_o$
1.5	1.62	1.67
2.00	1.64	1.82
2.69	1.66	1.95
3.50	1.60	2.14
4.20	1.67	2.17

4 CMA 5, $x = 0.032$		
T	$S_o$	$T_o$
1.5	0.80	3.87
2.03	1.07	6.22
2.74	1.10	6.49
3.46	1.17	7.15
4.2	1.19	7.45

1 CMA 7B, $x = 0.0105$		
T	$S_o$	$T_o$
1.5	1.53	2.50
2.00	1.51	2.50
2.71	1.62	3.09
3.37	1.66	3.24
4.20	1.67	3.35

### 8.3 Shubnikov de Haas results and interpretation

In this section we present the results of the SdH measurements on  $(\text{Cd}_{1-x}\text{Mn}_x)_3\text{As}_2$ . A typical set of curves is given in fig. 8.3. These data were taken for sample 1 CMA 7B with  $x = 0.01$  and  $n_e = 6.4 \cdot 10^{24} \text{ m}^{-3}$ . For this sample we measured the SdH signals for a fixed orientation as a function of the temperature. The nodes in the oscillation amplitude are clearly visible in this figure.

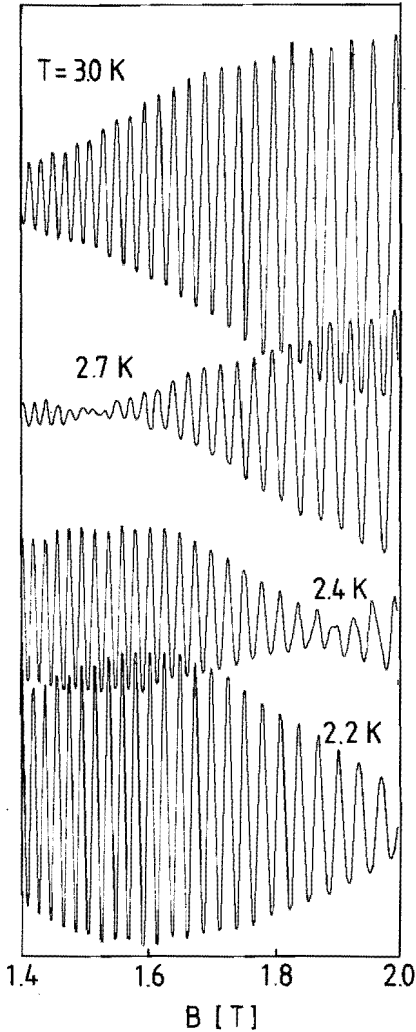


Fig. 8.3

SdH recorder traces for  $(\text{Cd}_{1-x}\text{Mn}_x)_3\text{As}_2$ ,  $x = 0.01$  with  $n_e = 6.2 \cdot 10^{24} \text{ m}^{-3}$  at different temperatures. The field is oriented parallel to the  $[001]$ -axis.



### 8.3.1 Anisotropy of the oscillation period

Figs. 8.4 and 8.5 give some experimental results of the measurements of the anisotropy of the SdH oscillation period. For the  $(\text{Cd}_{1-x}\text{Mn}_x)_3\text{As}_2$ - $\text{Cd}_3\text{As}_2$  system two mechanisms contribute to the anisotropy of the oscillation period: the warping of the Fermi surface and the tetragonal distortion of the lattice.

Our results on the anisotropy of the oscillation period follow the trend observed by Blom et al. [6]. These authors report that the anisotropy of the bandstructure due to the tetragonal distortion of the lattice decreases with increasing Mn concentration. The rate of anisotropy can be expressed in the ratio  $P_{\parallel}/P_{\perp}$ , where  $P_{\parallel}$  and  $P_{\perp}$  represent the oscillation periods for the magnetic field parallel and perpendicular to the [001]-axis respectively. The data by Blom et al. [6] show that  $P_{\parallel}/P_{\perp}$  decreases from 1.16 to 1.05 going from  $x = 0$  to  $x = 0.01$  for  $n_e = 4.0 \cdot 10^{24} \text{ m}^{-3}$ . Because  $P_{\parallel}/P_{\perp}$  depends on the carrier density, this ratio must be compared for equal carrier densities.

The decrease of the anisotropy is in agreement with the observation that the difference between the lattice constants in the [100] and [001]-direction decreases [7,8]. This means that the crystal structure gradually changes from tetragonal to cubic with increasing  $x$ . A decreasing tetragonal distortion of the lattice reduces the crystal field splitting parameter  $\delta$  and reduces also the difference between the values of  $P_{\parallel}$  and  $P_{\perp}$ . In the  $(\text{Cd}_{1-x}\text{Mn}_x)_3\text{As}_2$ - $\text{Cd}_3\text{As}_2$  system, the anisotropy effects due to the tetragonal distortion of the lattice become most pronounced for low carrier densities. Therefore an accurate relation between the Mn concentration and  $\delta$ ,  $P_{\parallel}$  and  $P_{\perp}$  can only be obtained from a set of samples with low carrier density ( $n_e < 1.0 \cdot 10^{24} \text{ m}^{-3}$ ). Despite numerous attempts to reduce the carrier density by annealing, we did not succeed to prepare samples with sufficiently low carrier densities. On the other hand the anisotropy effects become relatively less important for samples with high carrier densities. This fact, combined with the reduction of the tetragonal distortion itself, leads to a reduced tetragonal anisotropy of the oscillation period for our samples.

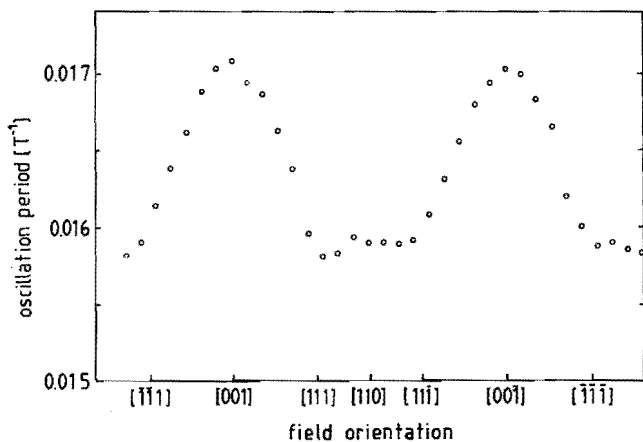


Fig. 8.4 The anisotropy of the oscillation period in  $(\text{Cd}_{1-x}\text{Mn}_x)_3\text{As}_2$  with  $x = 0.01$ .

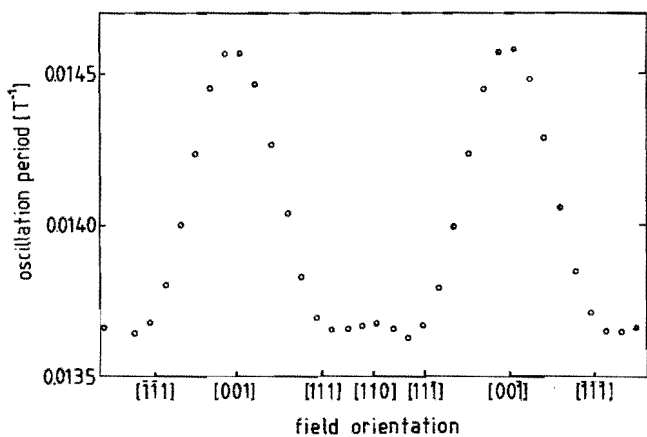


Fig. 8.5 As fig. 8.4 for  $x = 0.015$ .

### 8.3.2 Nodes in the oscillation amplitude.

In fig. 8.6 we plotted the amplitude of the oscillations for a constant magnetic field as a function of temperature, for sample 1 CMA 7 with  $n_e = 3.8 \cdot 10^{24} \text{ m}^{-3}$ . The different symbols mark the data for  $B \parallel [001]$  and  $B \parallel [100]$ . The temperatures where the minima in the amplitude occur, differ less than 0.05 K for the two orientations. This small difference in temperatures is equal to the experimental accuracy in the determination of the temperature, as discussed in chapter 7. Therefore we cannot discern any anisotropy in the appearance of the nodes.

For all samples we observed similar results for the anisotropy of the nodes. From these experimental results we conclude that the anisotropy of the nodes is negligibly small.

Although the theoretical work by Neve et al. [9] predicts a strong angular dependence of the nodes due to the tetragonal lattice distortion, we decided, considering our experimental results, to neglect the tetragonal distortion in the bandmodel used for the interpretation of our data on  $(\text{Cd}_{1-x}\text{Mn}_x)_3\text{As}_2$ . In that case the crystal structure is

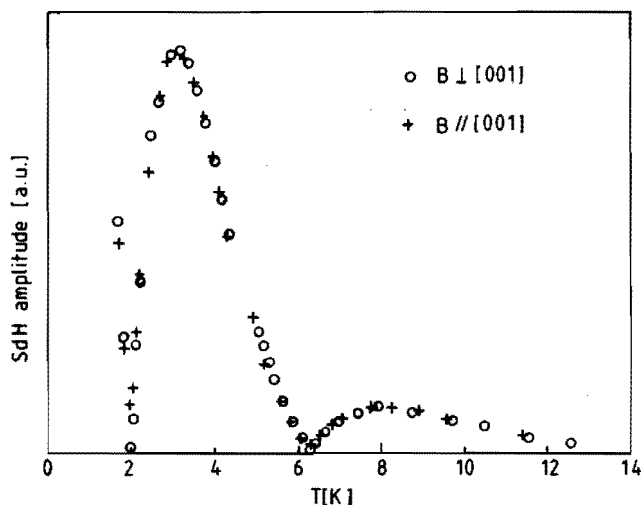


Fig. 8.6 Temperature dependence of the SdH oscillation amplitude for  $(\text{Cd}_{1-x}\text{Mn}_x)_3\text{As}_2$ ,  $x = 0.01$  with  $n_e = 3.8 \cdot 10^{24} \text{ m}^{-3}$  at  $B = 1.33 \text{ T}$ . The different symbols represent the data for the orientations as indicated in the figure.

assumed to be cubic. The warping and the inversion asymmetry are again the two remaining mechanisms which can cause anisotropy of the bandstructure. As we have seen for  $\text{Hg}_{1-x}\text{Mn}_x\text{Se}$ , the warping causes only a very weak anisotropy of the spin splitting. The inversion asymmetry, which is responsible for the strong anisotropy of the nodes in  $\text{Hg}_{1-x}\text{Mn}_x\text{Se}$ , also exists in  $(\text{Cd}_{1-x}\text{Mn}_x)_3\text{As}_2$  crystals. However, beating effects in the SdH oscillations as observed for  $\text{HgSe}$  were never found for  $\text{Cd}_3\text{As}_2$ . Apparently the effects of the inversion asymmetry are small and can be neglected.

Neglect of the tetragonal distortion, the warping and the inversion asymmetry results in an isotropic bandmodel

In the case the tetragonal distortion is neglected, the crystal field splitting parameter  $\delta$  is set equal to zero and the momentum matrix elements  $P_{\parallel}$  and  $P_{\perp}$  are taken equal to each other. For the actual value for  $P$  we choose the mean value for  $P_{\parallel}$  and  $P_{\perp}$  from  $\text{Cd}_3\text{As}_2$ . The resulting set of bandparameters for  $(\text{Cd}_{1-x}\text{Mn}_x)_3\text{As}_2$  for the isotropic model is listed in table 8.3, together with the parameters for  $\text{Cd}_3\text{As}_2$ . Without tetragonal distortion also the exchange integrals  $\beta_{\parallel}$  and  $\beta_{\perp}$  become equal.

Table 8.3. Bandparameters for  $(\text{Cd}_{1-x}\text{Mn}_x)_3\text{As}_2$  and  $\text{Cd}_3\text{As}_2$  [4]

$(\text{Cd}_{1-x}\text{Mn}_x)_3\text{As}_2$	$\text{Cd}_3\text{As}_2$
$E_g = -0.095 + 1.45 x \text{ eV}$	$E_g = -0.095 \text{ eV}$
$P_{\perp} = 7.32 \cdot 10^{-10} \text{ eVm}$	$P_{\perp} = 7.43 \cdot 10^{-10} \text{ eVm}$
$P_{\parallel} = 7.32 \cdot 10^{-10} \text{ eVm}$	$P_{\parallel} = 7.21 \cdot 10^{-10} \text{ eVm}$
$\Delta_{\text{so}} = 0.27 \text{ eV}$	$\Delta_{\text{so}} = 0.27 \text{ eV}$
$\delta = 0$	$\delta = 0.085 \text{ eV}$

The isotropic bandmodel can be obtained from the  $8 \times 8$  matrix in table 3.5, by substituting  $\delta = 0$ ,  $P = P_{\parallel} = P_{\perp}$  and  $\beta = \beta_{\parallel} = \beta_{\perp}$ . In the case  $k_B = 0$  and  $\langle S^+ \rangle = \langle S^- \rangle = 0$  one can follow the approach for  $\text{Cd}_3\text{As}_2$  by Wallace [10] to derive an analytical expression for the effective g-factor, and subsequently for  $\nu$ . The resulting expression for  $\nu$  for electrons at the Fermi level  $E_F$  is given by

$$\nu = - \frac{\hbar}{eB} \left[ \frac{(E_F - E_g)(E_F + 2\Delta_{so}/3)b + E_F(E_F + \Delta_{so})a - P^2 \Delta_{so} / 3\lambda^2}{(E_F + 2\Delta_{so}/3)P^2} \right] \quad (8.2)$$

where  $\lambda^2 = \hbar/eB$ ,  $a = 1/2 \alpha x \langle S_B \rangle$ ,  $b = 1/2 \beta x \langle S_B \rangle$ .

The value of  $\nu$  can be determined in a node using the procedure for this purpose given in the previous chapter. Substitution of  $\nu$ ,  $x$ ,  $\langle S_B \rangle$ , the Fermi energy and the parameters from table 8.3 in eq. 8.2 yields a relation in  $\alpha$  and  $\beta$ . We followed this procedure for several samples with different Mn concentrations and different carrier densities. For each Mn concentration we obtained a number of  $\alpha, \beta$ -relations, corresponding to the different carrier densities. In principle one set of values for  $\alpha$  and  $\beta$  should satisfy all equations for one Mn concentration. In practice however, each pair of relations leads to a different set of values for  $\alpha$  and  $\beta$ . The values of  $\alpha$  and  $\beta$  of these sets scatter over a range of a few eV. This large scatter in the values of  $\alpha$  and  $\beta$  is found for all Mn concentrations. The scatter is much larger than in the case of  $\text{Hg}_{1-x}\text{Mn}_x\text{Se}$ . This is probably due to a gradient in the Mn concentration over the  $(\text{Cd}_{1-x}\text{Mn}_x)_3\text{As}_2$  samples. As we have seen in chapter 5, strong gradients of the Mn concentration parallel to the growth direction occur in the as-grown ingots. Homogeneous samples can only be obtained when they are taken from slices cut perpendicular to the growth direction. In contrast to the  $\text{Hg}_{1-x}\text{Mn}_x\text{Se}$  samples, the desired orientation can only seldom be obtained for samples cut with their long edge perpendicular to the growth direction. It is therefore very likely that a gradient in the Mn concentration arises over the  $(\text{Cd}_{1-x}\text{Mn}_x)_3\text{As}_2$  samples.

The average values of  $\alpha$  and  $\beta$  obtained from our data for all Mn concentrations are given by:  $\alpha = -3.8 \pm 3.0$  eV and  $\beta = 2.3 \pm 3.5$  eV. The error margins are given by the standard deviation of all values for  $\alpha$  and  $\beta$ .

Despite the large scatter we can conclude that the signs of  $\alpha$  and  $\beta$  follow the same trend as found for the II-VI compounds.  $\alpha$  yields a ferromagnetic interaction for s-symmetric wave functions and  $\beta$  indicates an antiferromagnetic interaction for p-symmetric wave functions. The values of  $|\alpha|$  and  $|\beta|$  are larger than the values for the narrow-gap II-VI SMSC, listed in table 7.5. Similar large values of  $\alpha$  and  $\beta$

for  $(\text{Cd}_{1-x}\text{Mn}_x)_3\text{As}_2$  were also found by Lubczynski et al. [4]:  $\alpha = -2$  eV and  $\beta = 2.5$  eV. The ratio between  $|\beta|$  and  $|\alpha|$  for  $(\text{Cd}_{1-x}\text{Mn}_x)_3\text{As}_2$  seems to be smaller than for the narrow-gap compounds of the II-VI family. However, as already mentioned in the discussion of the exchange parameters of  $\text{Hg}_{1-x}\text{Mn}_x\text{Se}$ , the trend that the ratio between  $|\beta|$  and  $|\alpha|$  is smaller for narrow-gap semiconductors than for wide-gap semiconductors can only be explained qualitatively. A theoretical model to give a quantitative analysis of the values of  $\alpha$  and  $\beta$  does not exist, and therefore a quantitative discussion of the difference of the values for  $\alpha$  and  $\beta$  obtained for  $(\text{Cd}_{1-x}\text{Mn}_x)_3\text{As}_2$  and for  $\text{Hg}_{1-x}\text{Mn}_x\text{Se}$  cannot be given.

In the previous chapter we discussed the influence of zero-field splitting on the determination of the exchange integrals  $\alpha$  and  $\beta$  from nodes in the SdH oscillations. Although the actual strength of the exchange interaction given by  $\alpha$  and  $\beta$  cannot be determined with great precision for  $(\text{Cd}_{1-x}\text{Mn}_x)_3\text{As}_2$ , the exchange part of the spin splitting still has to be proportional to  $\langle S_B \rangle$ , for a correct determination of  $\alpha$  and  $\beta$ . We tested this, using the same approach as for  $\text{Hg}_{1-x}\text{Mn}_x\text{Se}$ . The exchange part of the spin splitting  $\Delta E_{\text{sp ex}}$  is plotted versus  $\langle S_B \rangle$ . A typical example is given in fig. 8.7. Fig. 8.7 shows that the exchange part of the spin splitting deviates only negligibly from the relation  $\Delta E_{\text{sp ex}} = J \times \langle S_B \rangle$ , given by the solid line. This indicates that the splitting is indeed proportional to  $\langle S_B \rangle$ . The extrapolation of the

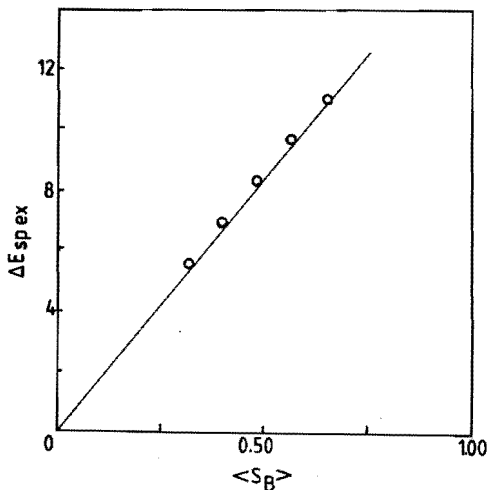


Fig. 8.7

Spin splitting for

$(\text{Cd}_{1-x}\text{Mn}_x)_3\text{As}_2$ ,  $x = 0.015$   
with  $n_e = 3.2 \cdot 10^{24} \text{ m}^{-3}$  as  
determined from the nodes.  
 $\langle S_B \rangle$  is calculated for the  
B,T-combinations where the  
nodes occur.

splitting to  $\langle S_B \rangle = 0$  yields the zero-field splitting energy. The average value of the zero-field splittings observed in the  $(\text{Cd}_{1-x}\text{Mn}_x)_3\text{As}_2$  samples is 0.15 meV, which is almost equal to the value of the splitting determined for  $\text{Hg}_{1-x}\text{Mn}_x\text{Se}$ . As in the case of  $\text{Hg}_{1-x}\text{Mn}_x\text{Se}$  the zero-field splitting energy comes very close to the accuracy of the values of  $\Delta E_{\text{sp ex}}$ .

Considering the possible existence of zero-field splitting in  $(\text{Cd}_{1-x}\text{Mn}_x)_3\text{As}_2$  we can draw the same conclusions as for  $\text{Hg}_{1-x}\text{Mn}_x\text{Se}$ . If zero-field splitting exists in  $(\text{Cd}_{1-x}\text{Mn}_x)_3\text{As}_2$  it is only very small and it does not influence the values of  $\alpha$  and  $\beta$  determined from the nodes in the SdH oscillations.

#### REFERENCES

- [1] C. Verié in *New developments in semiconductors* ed. by P.R. Wallace (Noordhoff Int. publ., Leiden, 1973) p. 511.
- [2] M.H. Weiler in *Semiconductors and Semimetals* Vol. 16, ed. R.K. Willardson and A.C. Beer (Academic Press, New York, 1981) p. 119.
- [3] J.J. Neve, Ph.D. Thesis, Eindhoven, University of Technology Eindhoven (1984).
- [4] W. Lubczynski, W. Zdanowicz, J. Cisowski, J.C. Portal, XV<sup>th</sup> school on the Physics of Semiconducting Compounds, Jaszowiec-Ustron, 1986, to be published in *Acta Physica Polonica*.
- [5] J. Bodnar, Proc. Int. Conf. Phys Narrow Gap Semicond...Warsaw, 1977 (Polish Scient. Publ., Warsaw, 1978) p. 311.
- [6] F.A.P. Blom, J.J. Neve, P.A.M. Nouwens, *Physica* 117B&118B, 470 (1983).
- [7] Z. Celinski, A. Burian, B Rzepa, W. Zdanowicz, *Mat. Res. Bull.* 22, 419 (1987).
- [8] C.J.M. Denissen, Ph.D. thesis, Eindhoven University of Technology, Eindhoven, 1986.
- [9] J.J. Neve, J. Kossut, C.M. van Es, F.A.P. Blom, *J. Phys. C: Solid State Phys.* 15, 4795 (1982).
- [10] P.R. Wallace, *Phys. Stat. Sol. (b)* 92, 49 (1979).

## CHAPTER IX DISTORTED SHUBNIKOV DE HAAS SIGNALS.

In the previous chapters we only used data obtained from undistorted SdH signals. However, in some experiments the SdH oscillations were distorted. In this chapter we discuss two kinds of anomalies observed. Firstly: other frequencies than the first and second harmonic can occur in the oscillation period of the SdH signal. Secondly: due to the influence of a superconducting phase transition of the solder material used to attach the electrical leads to the sample, a distortion can occur in a limited range of the magnetic field.

### 9.1 Nodes in the SdH oscillation amplitude due to beating effects

Interference effects between two oscillations with slightly different frequency can cause additional nodes in the amplitude of the superposition of these oscillations. Especially because we are studying the appearance of nodes in the SdH signals due to spin splitting effects, the occurrence of additional nodes due to frequency beating is bothersome. Examples of this beating are shown in figs. 9.1 and 9.2 for pure HgSe and  $\text{Hg}_{0.95}\text{Mn}_{0.05}\text{Se}$  respectively.

Due to the large number of nodes and their periodicity in  $1/B$  it can be easily recognised here, that these nodes are no spin splitting nodes. In both cases the beating effects manifest themselves most

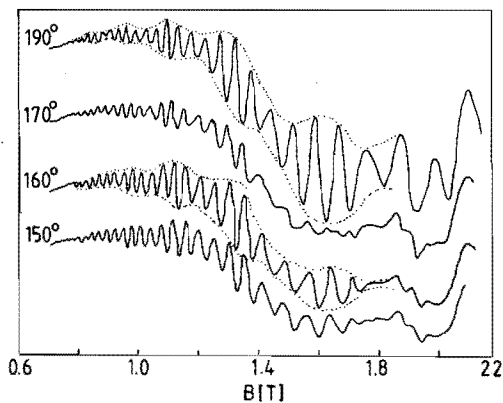


Fig. 9.1  
SdH signal showing additional nodes in the amplitude due to frequency beating. The signal was recorded for a HgSe sample. The angle between the magnetic field and the [001]-axis is indicated in the left part of the figure.



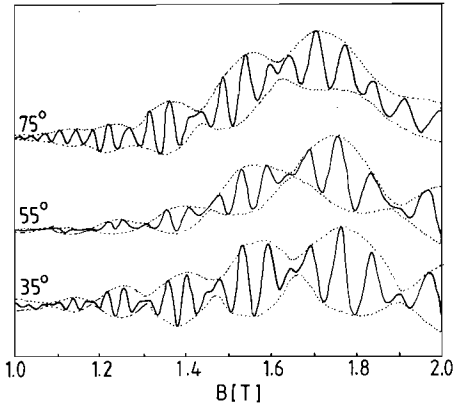


Fig. 9.2

As fig.9.1 for a  $\text{Hg}_{1-x}\text{Mn}_x\text{Se}$  sample with  $x = 0.005$ .

strongly if the magnetic field is oriented parallel to the [111] crystal axis. For  $\text{Hg}_{1-x}\text{Mn}_x\text{Se}$  we also observed a temperature dependence of the nodes. In this case the beating was most pronounced in the measurements at 2.62 K and less at 1.6 K and 3.5 K.

Booth [1] has shown that a gradient in the carrier density can cause beating effects in the SdH signal. We do not follow the approach of Booth, but simply assume that the sample can be divided in two parts with different carrier density. Each part contributes equally to the SdH signal with its own oscillation period. Although the assumption of a step-like change of the carrier density is somewhat unrealistic in practice, we can obtain an estimate of the range over which the carrier density varies, by calculating the carrier densities corresponding to the two oscillation periods contributing to the SdH signal. For the HgSe sample we find a mean oscillation period of  $0.0315 \text{ T}^{-1}$  and a beating period of  $0.1414 \text{ T}^{-1}$ . This can be the result of the superposition of signals with oscillation periods of  $0.0258 \text{ T}^{-1}$  and  $0.0408 \text{ T}^{-1}$  corresponding to carrier densities of  $1.4 \cdot 10^{24} \text{ m}^{-3}$  and  $6.9 \cdot 10^{23} \text{ m}^{-3}$  respectively. For  $\text{Hg}_{0.95}\text{Mn}_{0.05}\text{Se}$  a mean oscillation period of  $0.02 \text{ T}^{-1}$  and a beating period of  $0.08 \text{ T}^{-1}$  lead to oscillation periods of  $0.016 \text{ T}^{-1}$  and  $0.026 \text{ T}^{-1}$  corresponding to  $n_e = 2.8 \cdot 10^{24} \text{ m}^{-3}$  and  $1.3 \cdot 10^{24} \text{ m}^{-3}$  respectively. In both cases we obtain a difference in carrier density of a factor of 2.

It is likely that there is indeed a strong carrier density gradient in the HgSe sample. The curves in fig. 9.1 were measured immediately after annealing. In this case a very extreme annealing procedure was performed. The sample was kept at  $500 \text{ }^\circ\text{C}$  during 24 min. Probably

the annealing time was too short to establish a homogeneous carrier distribution, and a strong carrier density gradient is created.

Also for the  $\text{Hg}_{1-x}\text{Mn}_x\text{Se}$  sample it seems likely that a carrier density gradient was created during annealing. This sample was kept at  $240^\circ\text{C}$  during 3 days, which is much less extreme than the procedure for the HgSe sample given above. However, at low annealing temperatures a long time is often needed to establish a homogeneous carrier distribution [2].

The origin of the orientation and temperature dependence of the beating effects is still unclear.

## 9.2 Second oscillation period

For both HgSe and  $\text{Hg}_{1-x}\text{Mn}_x\text{Se}$  we observed sometimes a very weak oscillation superimposed on the main SdH signal. This second oscillation is also periodic in  $1/B$ . Sometimes this goes together with an orientation dependent decrease of the amplitude of the first harmonic of the oscillation as shown in fig. 9.3. The minimum amplitude is observed in the case the magnetic field is oriented almost parallel to the  $[111]$ -axis.

The appearance of the second oscillation period is illustrated in fig. 9.4 for a HgSe sample with  $n_e = 1.7 \cdot 10^{23} \text{ m}^{-3}$ . Only for very low magnetic fields the first harmonic can be observed. For higher fields the spin splitting of the oscillation peaks becomes visible and the oscillation frequency is doubled. For still higher fields the oscillation frequency doubles again. This frequency doubling is also observed most pronounced for field orientations close to the  $[111]$  crystal axis. With decreasing temperature the amplitude of the high frequency oscillations increases much faster than the amplitude of the main oscillation.

The frequency doubling was observed for several HgSe samples with carrier densities in the range of  $1.0 \cdot 10^{23} < n_e < 2.0 \cdot 10^{23} \text{ m}^{-3}$ . Also the  $\text{Hg}_{1-x}\text{Mn}_x\text{Se}$  samples which showed this behaviour had a carrier density in this range. These carrier densities were obtained after a long annealing period (more than 50 hours) at relatively low temperatures ( $180\text{--}200^\circ\text{C}$ ).

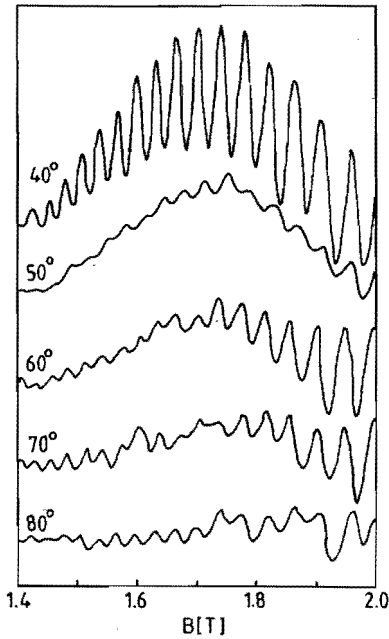


Fig. 9.3

SdH recorder traces as a function of the orientation for  $\text{Hg}_{1-x}\text{Mn}_x\text{Se}$ ,  $x = 0.005$  at 1.4 K. The field was rotated in the  $(\bar{1}10)$ -plane. Note the decrease of the oscillation amplitude for field orientations close to the  $[111]$ -axis.

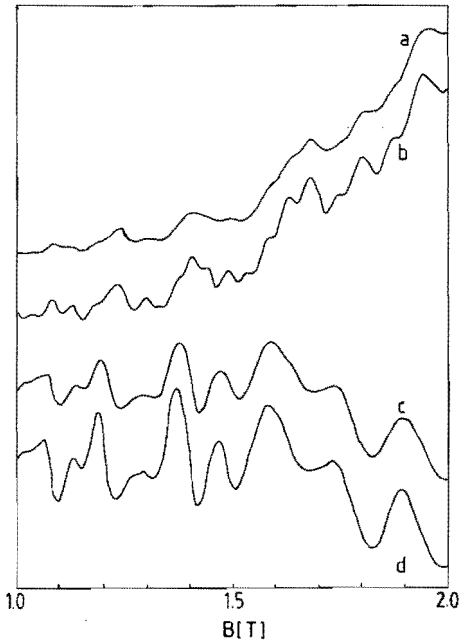


Fig. 9.4

SdH recorder traces for HgSe with  $n_e = 1.7 \cdot 10^{23} \text{ m}^{-3}$ . Curves (a) and (b) are taken for  $B \parallel [111]$  at 4.2 K and 1.4 K respectively. Note the rapid decrease of the high frequency oscillation. Curves (c) and (d) are taken for  $B \parallel [001]$  at 4.2 K and 1.4 K respectively. The high frequency oscillation is invisible for this orientation.

The appearance of additional peaks in the SdH oscillations of HgSe was already reported in literature [3-5]. Gałazka et al. [3] reported on high field measurements on HgSe. Additional peaks were observed for all magnetic field orientations but most often for  $B \parallel [111]$ . The carrier density range of the samples in which the extra peaks were observed was quite broad:  $1.7 \cdot 10^{23} \text{ m}^{-3} < n_e < 2.2 \cdot 10^{24} \text{ m}^{-3}$ . The authors speculate that the additional resistivity maxima might result from the coincidence of the Fermi level and impurity levels which are degenerated with the conduction band. In that case, the impurity levels must be quantised by the magnetic field. The angular dependence of the resulting impurity level splitting can in principle be different from the angular dependence of the splitting of the Landau levels. This might be the reason of the angular dependence of the appearance of the additional peaks.

Byszewski et al. [5] report on SdH measurements on HgSe at 77 K in high fields. They observed additional peaks for their purest samples ( $n_e = 2.2 \cdot 10^{23} \text{ m}^{-3}$  and  $3.3 \cdot 10^{23} \text{ m}^{-3}$ ). Their explanation of the effects is related to warping of the lowest magnetic subbands. The warped bands have kinks at k-vector values of about  $0.6 \cdot 10^8 \text{ m}^{-1}$  some meV above the bottom of the band. This kink gives rise to a rapid increase of the density of states. In the case this rapid increase of the density of states coincides with the Fermi level, the corresponding increase of the scattering probability gives rise to a resistivity maximum. The angular dependence of the warping might be the reason for the orientation dependence of the additional peaks.

If we assume that the kink in the k-dependence of the bands also appears for higher Landau numbers, this gives rise to two maxima in the density of states in one subband. In our experimental conditions this doubles the number of resistivity peaks per subband. This accounts for our observation of the fourth harmonic in the SdH oscillations. The preference of the additional peaks to appear for the magnetic field oriented parallel to the  $[111]$ -axis can be related to the anisotropy in the bandstructure. The observed increase of the oscillation amplitude with decreasing temperature agrees with the theoretically predicted faster increase of the amplitude of the higher harmonics compared to the amplitude of the first harmonic. It has to be mentioned that even a very weak fourth harmonic component of the

SdH signal, originating from weak maxima in the density of states, can be observed in our SdH curves because the modulation technique enhances the amplitude of higher harmonics.

Also in measurements on some of the  $(\text{Cd}_{0.96}\text{Mn}_{0.04})_3\text{As}_2$  samples a second oscillation period was observed. The additional oscillation appeared close to the spin splitting nodes, where the amplitude of the first harmonic of the main frequency is very small. The oscillations were periodic in  $1/B$ .

A more detailed study of this effect was performed on pure  $\text{Cd}_3\text{As}_2$  samples where this kind of oscillations appeared as well. An example of these measurements is shown in fig. 9.5. This figure shows SdH oscillations for two different temperatures. There was no preferential orientation for the appearance of the additional frequency. From the temperature dependence of the amplitude of the oscillations, the effective electron masses were determined. The high frequency oscillations originate from electrons with a high effective mass. A high effective mass is theoretically expected for electrons in regions with high carrier densities. A similar analysis of this effect in HgSe could not be done because the amplitude of the high frequency oscillations was too small to obtain reliable values for the effective masses.

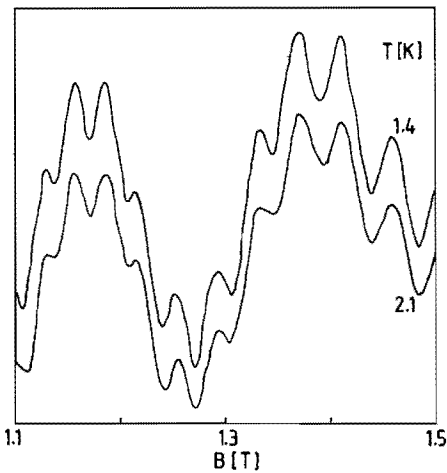


Fig. 9.5  
SdH recorder traces for  $\text{Cd}_3\text{As}_2$ , showing a second oscillation superimposed on the main signal for two different temperatures.

Table 9.1. Oscillation periods ( $P$ ) and effective masses ( $m$ ) for the main frequency (1) and the superimposed frequency (2) for  $\text{Cd}_3\text{As}_2$  measured for  $B \parallel [001]$  ( $\alpha$ ) and  $B \parallel [100]$  ( $90^\circ$ ).

	exp. 1	theor.	exp. 2	theor.	exp. 3	theor.	exp. 4	theor.
$P_1(0)$					0.204			
$m_1(0)$								
$P_2(0)$					0.018			
$m_2(0)$								
$P_1(90)$	0.124		0.140		0.138		0.126	
$m_1(90)$			0.0186	0.0202	0.0176	0.0203		
$P_2(90)$	0.022		0.027		0.0142		0.016	
$m_2(90)$	0.038	0.041	0.035	0.037	0.0545	0.0504	0.057	0.476
$P_1(0)/P_1(90)$					1.48	1.57		
$P_2(0)/P_2(90)$					1.27	1.16		

Also the anisotropy of both oscillation periods was determined. The results for the anisotropy of masses and periods were compared to the values predicted by the bandstructure model for the tetragonally distorted lattice (chapter 3), using the  $\text{Cd}_3\text{As}_2$  parameters listed in table 8.3. This comparison is listed in table 9.1. From table 9.1 we can conclude that the anisotropy ratios and the effective masses of the second oscillations agree quite well with the predicted values. Therefore we conclude that the second oscillation period in  $\text{Cd}_3\text{As}_2$  is caused by the contribution to the SdH signal from a part of the sample with a higher carrier density. The second oscillation period was only observed in  $(\text{Cd}_{1-x}\text{Mn}_x)_3\text{As}_2$  and  $\text{Cd}_3\text{As}_2$  samples, which had been subjected to an annealing procedure, indicating that the inhomogeneous carrier density is created by the annealing of the samples.

### 9.3 Appearance of the superconducting phase transition of solders in magnetoresistance measurements

In this section we discuss the effect of phase transitions of the solder materials used to attach the current and voltage leads to the samples. These effects can cause a distortion of the SdH signal. We only observed this kind of distortion in measurements on  $\text{Cd}_3\text{As}_2$  and  $(\text{Cd}_{1-x}\text{Mn}_x)_3\text{As}_2$ , because only for these materials we used a solder material, which becomes superconducting.

The effect was first observed in a  $(\text{Cd}_{1-x}\text{Mn}_x)_3\text{As}_2$  sample with  $x = 0.0025$ . For this sample no SdH oscillations were observed. However, in measurements of the second derivative of the magnetoresistance one single oscillation appeared (curve c in fig. 9.6). The field position of the oscillation shifts towards higher fields when the temperature is lowered. Fig. 9.6 also shows the amplification of this effect by the modulation technique. Curve b gives the first derivative of the magnetoresistance. The direct measurement (curve a) shows only a very weak kink at the field position where the oscillation is observed in the second derivative.

In the case the single oscillation is superimposed on the usual SdH signal, it appears as if the one of the peaks of the SdH oscillations has an anomalously large amplitude (fig. 9.7). This figure also shows that the field position of the anomaly shifts with changing

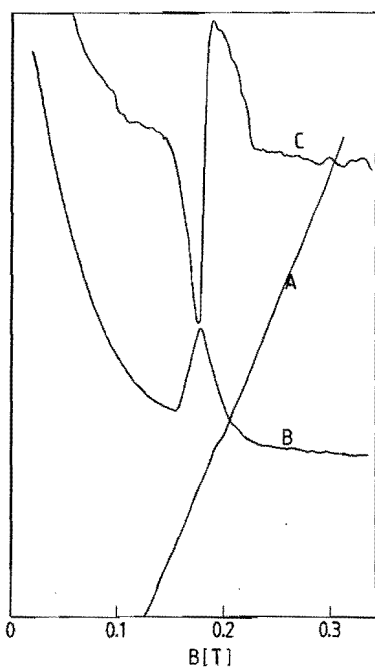


Fig. 9.6  
 Appearance of the superconducting phase transition in magneto-resistance measurements on sample  $(\text{Cd}_{1-x}\text{Mn}_x)_3\text{As}_2$ ,  $x = 0.0025$  with Rose metal contacts. Curve (a) direct, (b) first derivative and (c) second derivative .

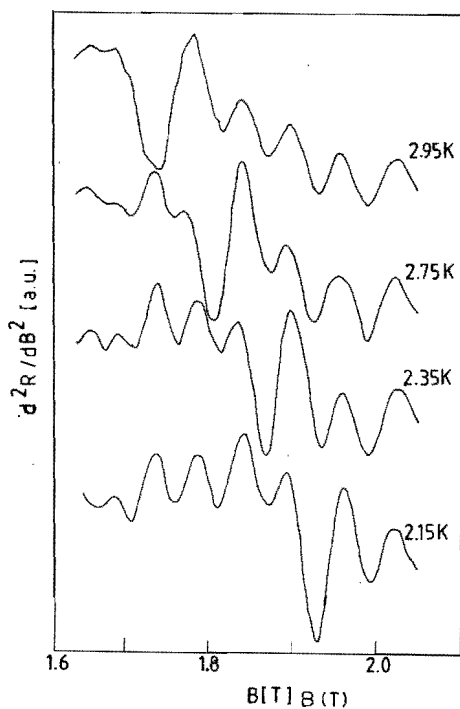


Fig. 9.7  
 Appearance of the superconducting phase transition in a SdH measurement (second derivative).



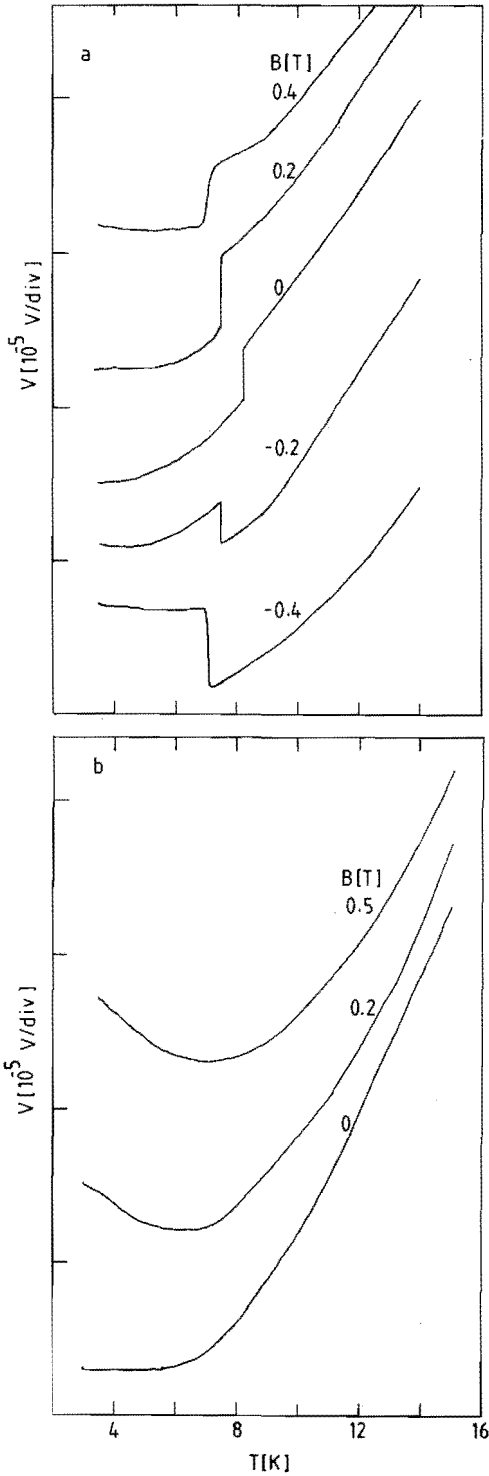


Fig. 9.8  
 Voltage measurements as a function of temperature, at different magnetic field values. The curves have been shifted relative to each other for clarity. (a) sample  $(\text{Cd}_{1-x}\text{Mn}_x)_3\text{As}_2$  with Rose metal contacts (b) same sample with indium contacts.

temperature. A possible relation between these effects and the presence of the Mn spins in  $(\text{Cd}_{1-x}\text{Mn}_x)_3\text{As}_2$  was ruled out by the appearance of similar effects in  $\text{Cd}_3\text{As}_2$ . When measuring the resistance at a constant magnetic field as a function of temperature we also observed a step-like change in the resistance. The combinations of field and temperature where the steps occur, correspond to those observed in the magnetoresistance. Figs. 9.8a and 9.8b show the voltage measured on a  $(\text{Cd}_{1-x}\text{Mn}_x)_3\text{As}_2$  sample as a function of temperature at different magnetic fields. A current of 100 mA was passed through the sample. Fig. 9.8a shows the results for a sample, where Rose metal (52.5-Bi, 32-Pb, 15.5-Sn) was used as a solder material. Fig. 9.8b shows the results for the same sample with In solder. The steps in the resistivity disappear with the change of solder material.

In Fig. 9.8a the step occurs at 8.2 K for  $B = 0$  T. This appears to be the temperature where the superconducting phase transition occurs in Rose metal. The superconducting properties of Rose metal are similar to those of Woods metal. The critical temperature for Woods metal (56-Bi, 14-Pb, 14-Sn, 16-Cd) is 8.5 K [6].

For three solder materials: pure In, CdIn alloy (50-Cd, 50-In) and Rose metal we did a large number of resistance measurements as a function of either temperature or magnetic field. We not only checked the effects on the magnetoresistivity of a semiconductor in the case In is used as a solder material, but we also measured the magnetoresistivity of In itself. The results are shown in fig. 9.9. From this figure we can see that a superconducting phase transition can give rise to more complex structures in the magnetoresistivity than the single oscillation in the case of Rose metal. Fig. 9.10 gives the temperature and field ranges in which the superconducting phase transition was observed experimentally for the three materials we examined.

Although fig. 9.9 shows large effects in the resistance of the solder material itself, a superconducting phase transition can also generate effects on the voltage measured on a semiconductor sample in an indirect way. A contact in the normal state will partially shunt the effective separation of the potential electrodes resulting in a decrease of the measured voltage. When the contacts are in the superconducting state, they will shunt this separation more effectively.

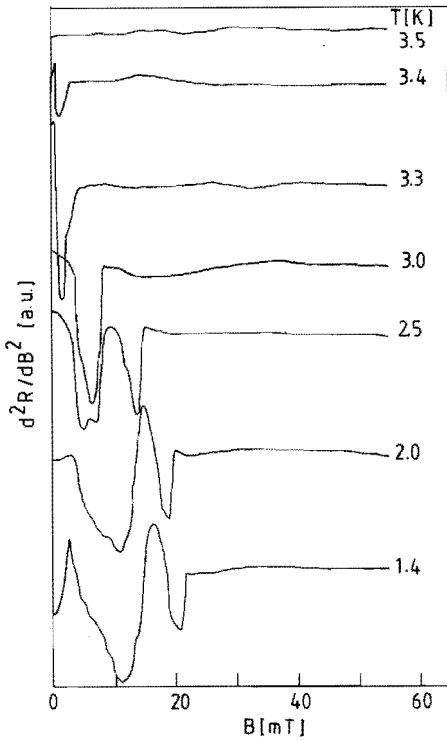


Fig. 9.9  
 Second derivative of the  
 magnetoresistance of a  
 pure indium sample.

The difference in measured voltage between the situation with superconducting contacts and the situation with normal contacts depends upon the ratio of the resistivities of solder material and sample material. The voltage measured on a sample, can be seriously affected by the current input configuration. In the absence of a magnetic field, a superconducting contact, covering the entire cross sectional area of the end of the sample, injects current uniformly. It is quite obvious that the same contact in the normal state injects the current non-uniformly. The maximum current density is expected in the vicinity of the place where the current lead enters the solder material. Whether this effect produces a higher voltage with normal or with superconducting contacts depends upon geometry.

Due to this mixture of influences it is obvious that very complicated structures can occur in magnetoresistance curves close to the superconducting phase transition. Many observations of anomalous steps, peaks and oscillations in measurements of magnetoresistance and its quantum oscillations [7,8] probably have been the result of using superconducting solder materials.

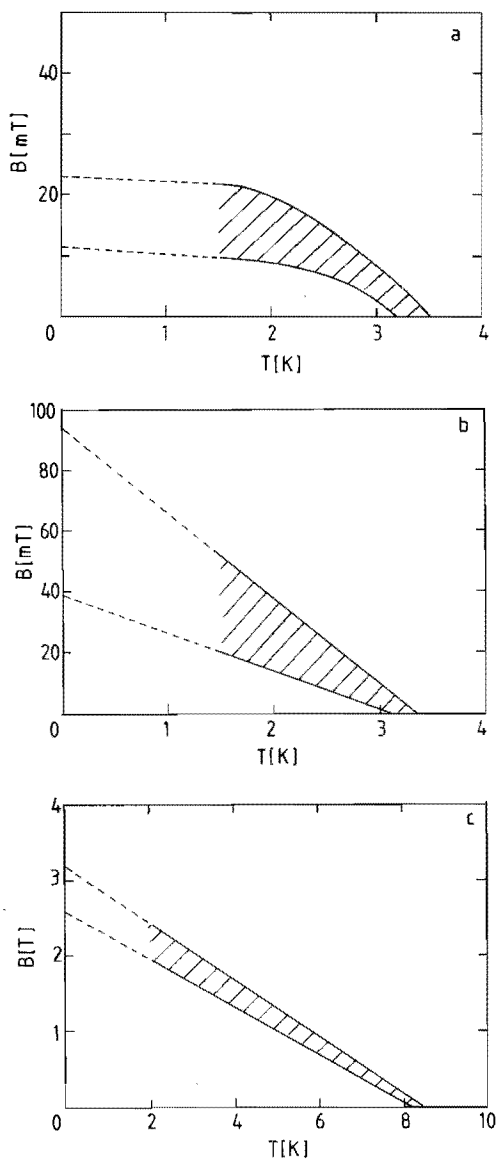


Fig. 9.10  
Diagrams indicating magnetic field and temperature ranges where the superconducting phase transition was found experimentally. (a) Indium, (b) CdIn alloy and (c) Rose metal.

## REFERENCES

- [1] B.L. Booth, Ph.D. thesis, Northwestern University, Evanston, Ill. (1967).
- [2] R.J. Iwanowski, *Acta Physica Polonica*, A47, 583 (1975).
- [3] R.R. Gałazka, W. Dobrowolski, J.L. Thuillier, *Phys. Stat. Sol. (b)* 98, 97 (1980).
- [4] W. Dobrowolski, T. Dietl, Proc. 13th. Int. Conf. Phys. Semicond., ed. F.C. Fami, Rome 1976, p. 447.
- [5] P. Byszewski, J. Kowalski, R.R. Gałazka, *Phys. Stat. Sol.(b)* 78, 477 (1976).
- [6] Handbook of Chemistry and Physics, 44th ed. The Chemical Rubber Publishing Co, Cleveland, 1961.
- [7] E.M. Skok, S.A. Studenikin, H. Hefel, and H. Pascher, *Pis'ma Zh. Eksp. Teor. Fiz.* 37, 468 [*JETP Lett.* 37, 554 (1983)].
- [8] O.V. Zharikov, *Pis'ma Zh. Eksp. Teor. Fiz.* 38, 108 (1983) [*JETP Lett.* 38, 126 (1983)].

## SUMMARY

This thesis reports on the study of the Shubnikov de Haas (SdH) effect in the narrow-gap semiconductors  $(\text{Cd}_{1-x}\text{Mn}_x)_3\text{As}_2$  and  $\text{Hg}_{1-x}\text{Mn}_x\text{Se}$ . These materials belong to the class of semimagnetic semiconductors (SMSC). In SMSC the spin splitting of the electron levels is strongly enhanced by the exchange interaction between the spins of the localised magnetic atoms and the spins of the band electrons.

Because the bandstructure (and consequently the spin splitting) in  $\text{HgSe}$  and  $\text{Cd}_3\text{As}_2$  are known to be anisotropic, we paid special attention to anisotropy effects in the study of the semimagnetic compounds based on these materials.

The anisotropy in  $\text{HgSe}$  is due to the lack of inversion symmetry in the zinc blende lattice. In the bandstructure of  $\text{Hg}_{1-x}\text{Mn}_x\text{Se}$  both the inversion asymmetry and the exchange interaction have to be taken into account. Since an adequate model did not exist, we developed a new model. With this new model we could calculate numerically the effects of inversion asymmetry on the bandstructure of  $\text{Hg}_{1-x}\text{Mn}_x\text{Se}$ .

For the interpretation of our experimental results on  $\text{Hg}_{1-x}\text{Mn}_x\text{Se}$  we used the values of the bandparameters as taken from literature, except for the exchange parameters and the inversion asymmetry parameters. To obtain a consistent set of data for our samples, the magnetisation is measured on the same samples as used in the SdH measurements.

The anisotropy of the SdH oscillation period can be explained without taking into account the inversion asymmetry and the exchange interaction. This anisotropy is completely determined by the interaction of the conduction band with higher bands.

The values of the exchange parameters  $\alpha$  and  $\beta$  are determined from the spin splitting. For the correct determination of these parameters, one has to be aware that both the exchange interaction and the inversion asymmetry contribute to the spin splitting. We have shown that the inversion asymmetry does not contribute to the spin splitting only for one particular orientation of the magnetic field. The exchange integrals are determined from data taken for this orientation:  $\alpha = -0.8 \pm 0.3$  eV and  $\beta = 1.3 \pm 0.3$  eV. These parameters fit the data for the samples of  $x = 0.025$  and  $x = 0.05$ . The values of  $\alpha$  and  $\beta$  obtained

from our experiments follow the trend for other narrow-gap SMSC of the II-VI family. We have demonstrated that neglect of the effects of inversion asymmetry can lead to serious errors in the values for  $\alpha$  and  $\beta$ .

Although we cannot determine one unique set of values for the three parameters describing the inversion asymmetry, we have shown that the influence of the inversion asymmetry on the bandstructure can be described with one "effective" parameter. Using this effective parameter, we can describe the anisotropy of the spin splitting in  $\text{Hg}_{1-x}\text{Mn}_x\text{Se}$  with our new bandmodel, thus proving that the strong anisotropy indeed originates from the inversion asymmetry.

$\text{Cd}_3\text{As}_2$  is anisotropic because the crystal structure of this material is tetragonal. The experimental results on  $(\text{Cd}_{1-x}\text{Mn}_x)_3\text{As}_2$  however, show that the bandstructure of this material is much less anisotropic than theoretically expected. We have shown that the results can be interpreted in an isotropic band model. The values of the bandparameters are based on those of  $\text{Cd}_3\text{As}_2$ , neglecting the tetragonal distortion of the lattice. We deduced the following relation for the bandgap as a function of the Mn concentration:  $E_g(x) = -0.095 + 1.45 x$  eV.

For the exchange integrals we obtained the values  $\alpha = -3.8 \pm 3$  eV and  $\beta = 2.3 \pm 3.5$  eV. The large scatter is probably due to inhomogeneities of the carrier density and the Mn distribution in the samples. However, the signs of  $\alpha$  and  $\beta$  still follow the trend for other narrow-gap SMSC. The magnitudes of  $\alpha$  and  $\beta$  are larger than for narrow-gap SMSC of the II-VI family.

## SAMENVATTING

Dit proefschrift beschrijft een onderzoek van het Shubnikov de Haas (SdH) effect in de kleine bandafstand halfgeleiders  $(\text{Cd}_{1-x}\text{Mn}_x)_3\text{As}_2$  en  $\text{Hg}_{1-x}\text{Mn}_x\text{Se}$ . Deze materialen behoren tot de groep van semimagnetische halfgeleiders. In semimagnetische halfgeleiders wordt de spinsplitsing van de electron-energieniveaus sterk vergroot door de exchange wisselwerking tussen de spins van de gelocaliseerde magnetische atomen en de spins van de bandelectronen.

Omdat van  $\text{HgSe}$  en  $\text{Cd}_3\text{As}_2$  bekend is dat de bandenstructuur (en bijgevolg ook de spinsplitsing) anisotroop is, is er bij het onderzoek aan de semimagnetische halfgeleiders gebaseerd op deze materialen speciale aandacht besteed aan anisotropie effecten.

De anisotropie in  $\text{HgSe}$  wordt veroorzaakt door het ontbreken van inversie symmetrie in het zinkblende kristalrooster. In het bandenstructuurmodel van  $\text{Hg}_{1-x}\text{Mn}_x\text{Se}$  moet zowel met de inversie-asymmetrie als de exchange-wisselwerking rekening gehouden worden. Omdat er geen adequaat model beschikbaar was, is er een nieuw model ontwikkeld. Met behulp van dit model kan de invloed van de inversie-asymmetrie op de bandenstructuur van  $\text{Hg}_{1-x}\text{Mn}_x\text{Se}$  numeriek berekend worden.

Bij de interpretatie van de experimentele resultaten van  $\text{Hg}_{1-x}\text{Mn}_x\text{Se}$  zijn alle waarden voor de bandparameters uit de literatuur genomen, behalve de parameters voor de exchange wisselwerking en de inversie asymmetrie. Om een consistente verzameling van data te verkrijgen is de magnetisatie aan dezelfde preparaten gemeten als welke gebruikt zijn voor de SdH metingen.

De anisotropie in de SdH oscillatie-periode kan verklaard worden zonder rekening te houden met de inversie-asymmetrie en de exchange-wisselwerking. Deze anisotropie is volledig bepaald door de wisselwerking van de geleidingsband met hogere banden.

De exchange-parameters  $\alpha$  en  $\beta$  zijn bepaald uit de spinsplitsing. Men moet er rekening mee houden dat zowel de exchange-wisselwerking als de inversie-asymmetrie bijdragen aan de spinsplitsing. We hebben aangetoond dat de inversie-asymmetrie niet bijdraagt aan de spinsplitsing voor één bepaalde oriëntatie van het magnetische veld.

De exchange-integralen zijn bepaald uit data gemeten voor deze oriëntatie:  $\alpha = -0.8 \pm 0.3$  eV en  $\beta = 1.3 \pm 0.3$  eV. Deze waarden vol-



doen zowel voor de preparaten met  $x = 0.025$  als voor  $x = 0.05$ . De waarden van  $\alpha$  en  $\beta$ , bepaald uit onze experimenten volgen de trend voor andere kleine bandafstand semimagnetische halfgeleiders uit de II-VI familie. We hebben gedemonstreerd dat verwaarlozing van inversie-asymmetrie kan leiden tot grote fouten in de waarden van  $\alpha$  en  $\beta$ .

Ofschoon we niet een eenduidige set van waarden voor de inversie-asymmetrie parameters hebben kunnen bepalen, hebben we aangetoond dat de invloed van de inversie-asymmetrie beschreven kan worden met één "effectieve" parameter. Met behulp van deze parameter kunnen we de anisotropie van de spinsplitsing in  $\text{Hg}_{1-x}\text{Mn}_x\text{Se}$  met ons nieuwe bandenstructuurmodel beschrijven. Hiermee is aangetoond dat de sterke anisotropie inderdaad door de inversie-asymmetrie veroorzaakt wordt.

In  $\text{Cd}_3\text{As}_2$  treedt anisotropie op omdat de kristalstructuur van dit materiaal tetragonaal is. De experimentele resultaten van  $(\text{Cd}_{1-x}\text{Mn}_x)_3\text{As}_2$  tonen echter aan dat de bandenstructuur van dit materiaal veel minder anisotroop is dan theoretisch verwacht wordt. Er is aangetoond dat deze resultaten geïnterpreteerd kunnen worden met een isotroop bandenstructuur model. Alle bandparameters zijn gebaseerd op die van  $\text{Cd}_3\text{As}_2$  waarbij de tetragonale verstoring van het rooster verwaarloosd wordt. Voor de bandafstandenergie als functie van de Mn concentratie hebben we de volgende relatie bepaald:  $E_g(x) = -0.095 + 1.45 x$  eV.

Voor de exchange integralen zijn de volgende waarden verkregen:  $\alpha = -3.8 \pm 3.0$  eV en  $\beta = 2.3 \pm 3.5$  eV. De grote spreiding is waarschijnlijk veroorzaakt door inhomogeniteiten in de electronen dichtheid en de verdeling van Mn atomen in de preparaten. Desondank volgen de waarden voor  $\alpha$  en  $\beta$  de trend van andere semimagnetische kleine bandafstand halfgeleiders. De waarden voor  $\alpha$  en  $\beta$  zijn voor  $(\text{Cd}_{1-x}\text{Mn}_x)_3\text{As}_2$  echter groter dan voor kleine bandafstand halfgeleiders uit de II-VI familie.

## DANKWOORD

Aan het tot stand komen van dit proefschrift en het hierin beschreven onderzoek hebben velen meegewerkt. Allen die op enigerlei wijze een bijdrage geleverd hebben wil ik op deze plaats bedanken. Mijn dank gaat speciaal uit naar Frank Arnouts, Frans Blom, Arno Buij, Johan Cuypers, Kees Denissen, Kitty van Dongen, René Ebersson, Kees van Es, prof. R.R. Gałazka, Ruth Gruyters, Klaas Kopinga, Eric Koppen, René Leenen, Jan Millenaar, Jan Mink, Peter Nouwens, Helga Pouwels, Bart Somers, Cees van der Steen, prof. dr. M.J. Steenland, Leon Trines, Rianne van Vinken, Paul van Waes, Joachim Wolter en de overige leden van de groep halfgeleiderfysica.

## CURRICULUM VITAE

- 19 sept 1958 Geboren te Heerlen
- 1970 -1976 Gymnasium  $\beta$   
St. Maartenscollege, Maastricht.
- 1976 -1983 Studie aan de Technische Universiteit Eindhoven,  
afdeling Technische Natuurkunde,  
Afstudeerwerk verricht in het Max Planck Institut für  
Festkörperforschung HML in Grenoble,  
Onderwerp ver-infrarood relectiemetingen aan  $\text{Cd}_3\text{As}_2$ .
- 1983-1987 Wetenschappelijk assistent aan de Technische Universi-  
teit Eindhoven in de groep halfgeleiderfysica onder  
leiding van prof. dr. J.H. Wolter.

**STELLINGEN**

Behorende bij het proefschrift van

H.M.A. Schleijsen

Eindhoven, 27 oktober 1987.

## Stellingen

1. Het verwaarlozen van de anisotropie in de spinsplitsing van de electron-energie niveaus kan aanleiding geven tot een foutieve bepaling van de exchange interactie parameters  $\alpha$  en  $\beta$  in semi-magnetische halfgeleiders met zink blende structuur.

*Dit proefschrift.*

2. De verklaring van het tekenverschil van de exchange interactie parameters  $\alpha$  en  $\beta$  op grond van de invloed van de hybridisatie van de Mn 3d-niveaus met de  $\Gamma_8$  valentie band, doet verwachten dat  $\alpha$  en  $\beta$  elk van teken zullen omkeren in zero-gap halfgeleiders, waar de bandenstructuur geïnverteerd is. De experimenteel bepaalde waarden spreken dit tegen.

K.C. Hass, B.E. Larssen, H. Ehrenreich, A.E. Carlson, *J. Magn. Mat.* 54-57, 1283 (1986).

3. De spin exchange wisselwerking zal in heterojuncties van semi-magnetische halfgeleiders de mogelijkheid openen de spinsplitsing onafhankelijk van de Landau-splitsing te variëren en daarmee een extra hulpmiddel opleveren om het spingedrag in een twee-dimensionaal electronengas te bestuderen.
4. Het bestuderen van de toestandsdichtheid van de geleidingsband in magneetvelden m.b.v. tunnelspectroscopie biedt het voordeel dat de electronendichtheid van de preparaten niet gewijzigd hoeft te worden, om de electron-eigenschappen bij verschillende electron-energieën te meten. Voor  $\text{Cd}_3\text{As}_2$  en mogelijk ook voor  $(\text{Cd}_{1-x}\text{Mn}_x)_3\text{As}_2$  is deze methode echter onbruikbaar vanwege het optreden van een oppervlakte-laag met afwijkende eigenschappen t.o.v. het bulkmateriaal.

H.M.A. Schletjpen, M. v. Ortenberg, M.J. Gelten, F.A.P. Blom, *Int. Journ. of Infrared and Millimeter Waves* 5, 171 (1984).

- 5 De controverse tussen de experimentele resultaten van magneto-optische en magneto-transport metingen aan HgSe betreffende de anisotropie van de effectieve electron-massa kan veroorzaakt zijn door het verwaarlozen van de inversie-asymmetrie bijdrage aan de spinsplitsing bij de interpretatie van gecombineerde spin-flip overgangen in de magneto-optische metingen.

*K. Schwarzbeck, M. v. Ortenberg, Proc. Int. Conf. on the Phys. of Semicond. Edinburgh 1978, p. 1125.*

- 6 De door Landee et al. voorgestelde spinstructuur van  $\text{CuCl}_2 \cdot \text{TMSO}$  in de magnetisch geordende fase is niet consistent met de door Bosch et al. gerapporteerde ferromagnetische interactie tussen de ketens in de kristallografische c-richting.

*C.P. Landee, R.B. Willet, F. Waldner, J. Appl. Phys. 53, 1888 (1982), L.A. Bosch, C.H.W. Swüste, A.C. Phaff, W.J.M. de Jonge, J. Phys. C, 20, 2307 (1987).*

- 7 De uitspraak dat botbreuken meestal op de laatste dag van een wintersportvakantie optreden moet worden verscherpt tot: Botbreuk betekent per definitie het einde van een actieve wintersportvakantie.

- 8 Persoonlijke relaties kan men fysisch beschouwen als attractieve potentialen die de mobiliteit van een fysicus beïnvloeden.

*Symposium: Mobiliteit van de fysicus (studievereniging J.D. van der Waals).*